# Towards a Global SQUID Network Through Optimal Monitoring Station Design

by

**Emile Tobias Lochner**

*Thesis presented in fulfilment of the requirements for the degree of Master of Engineering at Stellenbosch University*

Faculty of Engineering, Department of Electrical and Electronic Engineering

Promoter: Prof. Coenrad J. Fourie
Co-Promoter: Mr. Daniel J. Gouws
Co-Promoter: Mrs. Elda Sanderson

Date: March 2015

# Declaration

By submitting this thesis electronically, I declare that the entirety of the work contained therein is my own, original work, that I am the sole author thereof (save to the extent explicitly otherwise stated), that reproduction and publication thereof by Stellenbosch University will not infringe any third party rights and that I have not previously in its entirety or in part submitted it for obtaining any qualification.

# Abstract

**Towards a Global SQUID Network Through Optimal Monitoring Station Design**

E.T. Lochner

Department of Electrical and Electronic Engineering,

University of Stellenbosch,

Private Bag X1, Matieland, 7602, South Africa.

Thesis: M. Eng (Research) (Electronic Engineering)

March 2015

The Superconducting QUantum Interference Device (SQUID) is one of the most sensitive magnetic field sensors in the world. These instruments can only be used optimally for geomagnetic research if placed far from man-made magnetic signals. Moving the SQUID to a remote site leads to several infrastructure-related problems including construction, power, data connectivity, and cryogenic cooling. This thesis investigates possible solutions to these problems and develops guidelines for designing future remote SQUID stations.

A remote SQUID observatory typically consists of three structures placed approximately 40 m apart. These include: the control room, which houses all computers and supporting electronics, the power hut, which contains a regulated battery bank charged from a solar array that delivers DC power to the rest of the system, and the SQUID hut itself, which is thermally insulated by cavity walls. The SQUID is placed on an isolation pillar that decouples it from structural vibrations due to wind and outside temperature fluctuations. The temperature inside the SQUID hut is also monitored as changes in temperature can result in small deformations of the SQUID mounting system which lead to changes in the SQUID's orientation. The changes in the orientation will appear as slow varying magnetic signals on the SQUID output. In principle, it is possible to compensate for these variations through post-processing.

The SQUID needs to be cryogenically cooled to function. The SANSA SQUID is a High Temperature Superconductor (HTS) and operates using liquid nitrogen. Immersion cooling is used, as it is the simplest method, and produces the least amount of mechanical and electrical noise. Over time the liquid nitrogen will evaporate and needs to be replaced without significantly disrupting SQUID operations. A simple yet effective pumping scheme was developed that can transfer approximately 1.8 litres of liquid nitrogen every minute from a refill dewar. Monitoring of the liquid nitrogen level is an important management tool for a remote station, as refilling will be the primary reason for technicians to visit the site. The monitoring is achieved by placing the SQUID dewar on a specially designed non-magnetic load cell scale. The scale has been designed to limit the amount of tilting as the weight changes since this would also change the SQUID orientation.

When a HTS SQUID is cooled in a large magnetic field, such as the Earth's field, Abrikosov vortices are likely to form in the superconducting material. As these vortices jump between pinning sites in the material, they increase the 1/f noise of the device and have been found to reduce the stability of the SQUID. Metal shields can be used to reduce the magnetic field, but are awkward to use and also reduce the magnitude of the signals of interest. In this thesis, a shielding method using Helmholtz coils is investigated. These coils are relatively simple and inexpensive to construct and do not attenuate the signals of interest. It was found that by cooling

the SQUID in the reduced magnetic field, generated by the Helmholtz coils, the stability of the SQUID can be improved significantly.

# Opsomming

**Nader aan 'n Globale SQUID Netwerk Deur Optimale Monitor Stasie Ontwerp**

(Towards a Global SQUID Network Through Optimal Monitering Station Design)

E.T. Lochner

Department of Electrical and Electronic Engineering,

University of Stellenbosch,

Private Bag X1, Matieland, 7602, South Africa.

Thesis: M. Eng (Research) (Electronic Engineering)

Maart 2015

Die SQUID is die mees sensitiewe magneetveld sensors in die wreld. Hierdie instrument kan slegs optimaal vir geometriese navorsing gebruik word indien dit vr van mensgemaakte magneetvelde opgestel word. Om die SQUID in 'n afgesonderde area op te stel veroorsaak verskeie probleme met betrekking tot infrastruktuur sover dit konstruksie, kragvoorsiening, en kriogeniese afkoeling aangaan. Hierdie tesis ondersoek moontlike oplossings vir die probleme en riglyne te ontwikkel vir die oprigting van toekomstige SQUID stasies.

'n Tipiese afgele SQUID observatorium bestaan gewoonlik uit 3 strukture wat 40m van mekaar opgestel is. Die beheerkamer bevat al die elektroniese apperaat, die kragkamer bevat 'n stel gereguleerde batterye wat deur sonpanele helaai word en DS krag verskaf aan die stasie en die SQUID-kamer wat deur middel van spoumure teen hitte gensoleer is. Die SQUID word op 'n gesoleerde pilaar geplaas om die invloed van vibrasies a.g.v. wind en wisselende buite temperature te verminder. Die temperatuur binne die SQUID kamer word ook noukeurig gemonitor aangesien wisseling in temperatuur geringe vervorming van die SQUID se montering kan veroorsaak wat 'n verandering van die SQUID se orintasie veroorsaak. Hierdie veranderings sal waargeneem word as stadige varirende sein in die SQUID se lesings. In beginsel is dit moontlik om vir dit te kompenseer deur middel van naprosessering.

Die SQUID moet kriogenies afgekoel word om te funksioneer. Die SANSA SQUID is 'n Ho Temperatuur Supergeleier (HTS) en vloeibare stikstof word gebruik vir verkoeling. Afkoeling deur middel van indompeling word gebruik omdat dit die kleinste hoeveelheid meganiese en elektroniese versteuring veroorsaak. Die vloeibare stikstof verdamp mettertyd em moet vervang word sonder om die werking van die SQUID merkbaar te onderbreek. 'n Eenvoudige tog effektiewe oorpompstelsel is ontwikkel wat ongeveer 1.8 liter/minuut vloeibare stikstof vanuit 'n hervullings vakuum fles kan oorpomp. Die meting van die vloeibare stikstof vlak is 'n belangrike aspek van die instandhouding van 'n afgele stasie aangesien dit die hoof rede sal wees vir tegnici om die perseel te besoek. Die meting word bewerkstellig deur die plasing van die SQUID se vakuum fles op 'n spesiale ontwerpte, nie-magnetiese vrag sel skaal. Hierdie skaal is ontwerp om die mate van kanteling te beperk aangesien dit die orentasie van die SQUID kan benvloed.

Wanneer 'n HTS SQUID binne in 'n groot magnetiese veld afgekoel word, is dit waarskynlik dat Abrikosov vortekse in die supergeleidende materiaal sal ontstaan. Soos hierdie vortekse rondspring in die materiaal vermeerder dit die 1/f ruis en daar is gevind dat die stabiliteit van die SQUID nadelig benvloed word. Metaal skilde kan gebruik word om die invloed van die magneetveld te verminder, maar is ongerieflik om te gebruik

en verminder ook die sterkte van die seine wat waarneem wil word. In hierdie tesis word Helmholtz spoele ondersoek as 'n afskermings metode. Hierdie spoele is eenvoudig om te vervaardig en verminder nie die sterkte van waarneembare seine nie. Daar is gevind dat die stabiliteit van die SQUID merkbaar verbeter word deur afkoeling in 'n lae magnetiese veld soos bewerkstellig deur die Helmholtz spoele.

# Acknowledgements

To my wife

Michelle

Who spent hours helping me edit my thesis and who put up with Helmholtz coils and liquid nitrogen systems taking up a considerable amount of space in our small flat. The thesis is now complete and we can have guests over for tea again.

To my supervisors

Prof. Fourie, Danie and Elda

who always provided me with insights into research and willingness to help. Your efforts have allowed me grow over the past two years, and I hope I can carry this momentum forward into my future endeavours.

To my parents

Johan and Marita

who supported me with kind words of encouragement when circuits did not do what they were supposed to, or when quantum mechanics proved a little tricky to understand. Thank you for believing in me.

To my sponsors

South African National Space Agency

for providing me with funding and facilities that hosted the SQUID. Without your support this thesis would not exist.

# Contents

# List of Figures

# List of Tables

# 1 Introduction

## 1.1 Motivation

Scientific knowledge relies on our ability to formulate an hypothesis and gather data to support or refute it. Without sufficient data to verify the claim, the hypothesis will always remain speculation and not develop into an accepted theory. It is thus reasonable to believe that if the technology we use to perform experiments and gather data do not advance, then our scientific knowledge will eventually also stagnate.

This thesis focusses on the development of a remote Superconducting QUantum Interference Device (SQUID) station for use in geomagnetic measurements. Currently the fluxgate magnetometer and the proton precession magnetometer are the workhorses for geomagnetic measurements. Although they have proven to be a simple and reliable instrument for the field, the SQUID has the potential to surpass it. While the SQUID is significantly harder to use than the fluxgate, it has the advantage of being more sensitive by orders of magnitude. This implies that with the SQUID it would be possible to measure faint signals that are currently undetectable. This is the primary motivation for this research.

Given the sensitivity of the SQUID, is is important that special consideration be given to site selection and the supporting systems. The ideal location for the SQUID would be in a magnetically clean environment far from man made interference. Unfortunately, placing the SQUID in a remote location also implies that the station will not have access to infrastructure like power and data connectivity. Without these and other supporting infrastructures, the station would not be able to function. This thesis primarily discusses the supporting infrastructure of such a remote station and presents potential solutions, that are either industry standard or developed as part of this research.

## 1.2 Current Systems

In order for the discussions that follow to be clear, a brief overview of what a basic SQUID system looks like will be described in this section. This will explain any terminology and give an overview of how these systems are typically installed.

### 1.2.1 South African National Space Agency

The South African National Space Agency (SANSA), Space Science Division, is located in Hermanus, South Africa (see Figure 1). It forms part of a global magnetic monitoring network, INTERMAGNET, and is the hub of space science in South Africa. It is ideally placed to study the South Atlantic Magnetic Anomaly, where the Earth's magnetic field strength is at its weakest. The facility also provides scientific and engineering support to South Africa's base in Antartica (SANAE) and supports various human capital development programs through training and funding schemes.


Figure 1: Location of SQUID on SANSA premises, showing nearby industrial area

The site hosts a High Temperature Superconductor (HTS) SQUID in a small building on the premises. The SQUID operates without magnetic shielding and hence is exposed to the Earth's unattenuated magnetic field. This is similar to how the remote stations are expected to operate as any attenuation will also affect the signals of interest. The majority of the electronics used for the SQUID is located approximately 20 meters away in a separate building. All structures on the SANSA premises are built using non-magnetic materials as far as possible to limit their effects on the local magnetic field.

This site is not ideal in terms of its noise properties as it is located in the centre of Hermanus close to a small industrial area. The surrounding human activity produces magnetic signals which can be detected on the SQUID and contributes to the noise of the system. Figure 2 shows an example spectrogram of 4 hours of SQUID data that shows magnetic contamination of the SANSA site. The 50 Hz signal from the national

power grid is clearly visible as well as several harmonics. The spectrum shows various spectral features whose amplitude and frequency change with time. Some of these features are fairly sharp, and hence believed to be man-made, but others are more dispersed and may be natural in origin. Because the spectrum at SANSA is contaminated to such a degree that it introduces additional uncertainty into the scientific measurements, it justifies the need to relocate to a remote site. The SANSA SQUID does however provide easy access and readily available infrastructure. It is thus suitable for testing various subsystems that could be used in future remote stations. Because of this, all tests in this research were performed on this system.

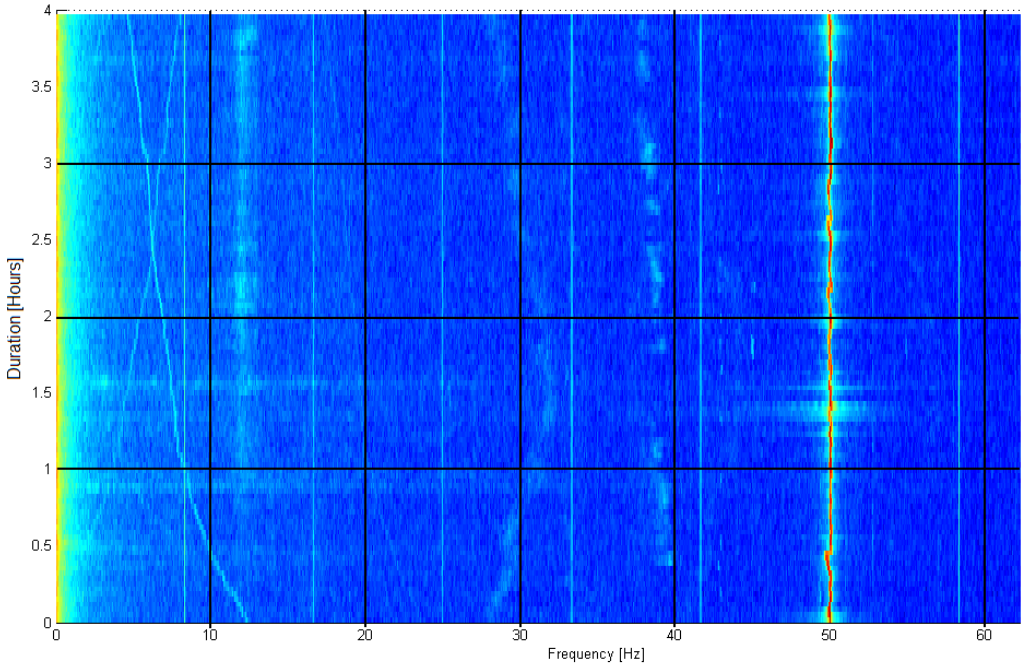


Figure 2: Spectrogram of SANSA SQUID over a four hour period showing contamination. The 50 Hz signal is due to the national power grid and the lines that appear every 8 Hz are harmonics that appear on the power grid.

During the course of this research the SQUID sensors were upgraded from a two-axis HTS SQUID to a more sensitive three-axis HTS SQUID, both from StarCryogenics. Their rated performance characteristics are summarised in Table 1.

Table 1: Rated characteristics of the HTS SQUID systems available at SANSA

| | 2012 SQUID | 2014 SQUID |
|---|---|---|
| No. of axes | 2 | 3 |
| Noise 10 Hz $\left[\frac{\text{fT}}{\sqrt{\text{Hz}}}\right]$ | 177 | 110 |
| Noise 1 kHz $\left[\frac{\text{fT}}{\sqrt{\text{Hz}}}\right]$ | 210 | 73 |
| Sensitivity $\left[\frac{\text{mV}}{\text{nT}}\right]$ | 35 | 526 |

### 1.2.2 Laboratoire Souterrain à Bas Bruit

Laboratoire Souterrain à Bas Bruit (LSSB)[1] is located near Rustrel, France (see Figure 3). The site is a decommissioned military bunker that has been converted for use in cross-disciplinary physics. The facility is comprised of a series of tunnels that lead into the mountain and is up to 500 m deep in places.

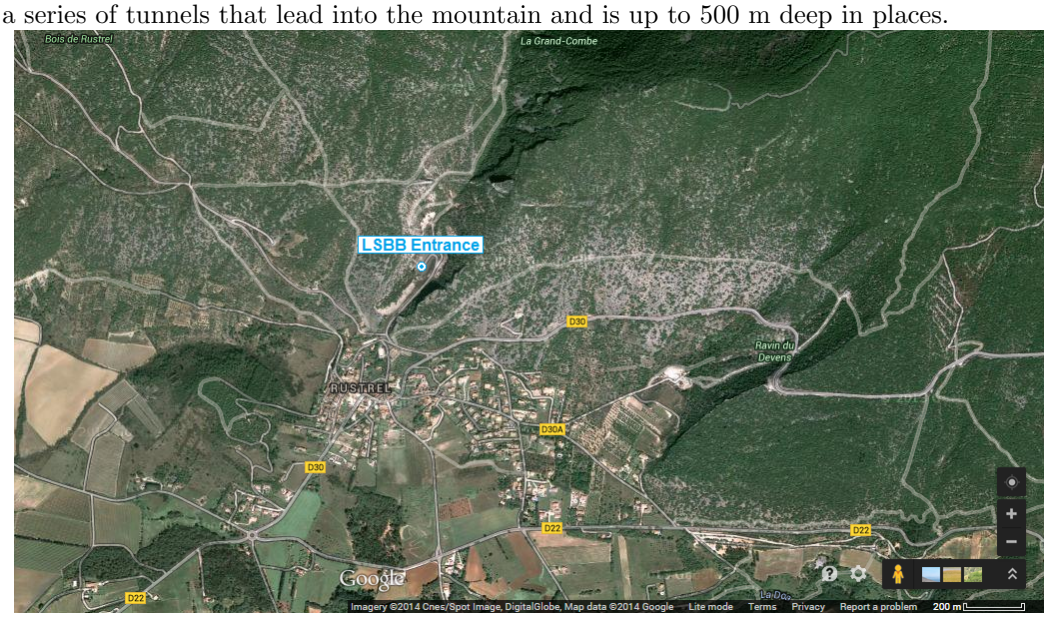


Figure 3: Location of LSBB entrance in Rustrel, France

This unique environment hosts several instruments including seismometers and a Low Temperature Superconductor (LTS) SQUID. The SQUID is placed deep in the mountain inside a non-$\mu$ metal capsule supported by large shock absorbing springs, which itself is placed inside a shielded concrete shell, known as the [SQUID$^2$] system, as shown in Figure 4.

The SQUID itself is immersed in liquid helium with the supporting electronics placed several meters outside the capsule. Originally this capsule was designed to protect the occupants against a nuclear attack, but now it is used to provide a significant amount of shielding for the SQUID sensor. This shielding produces a low noise environment of 2 fT/$\sqrt{\text{Hz}}$ above 10 Hz and allows the LTS SQUID to detect low frequency fluctuations in the Earth's magnetic field. The facility's seismometers allows scientists to study simultaneous measurements of earthquakes and their effects on the the Earth's magnetic field.

Figure 5 shows measurements taken by the author in the LSBB capsule in June 2013. A 3 axis fluxgate magnetometer was used, Lemi-11, to record the magnetic flux and the sensor was supported on a wooden structure that has several levels which the sensor could be mounted to. Due to limited equipment at the time, the uncertainty in the vector measurement is in the order of 3 degrees. Regardless, the map still shows significant distortion of the magnetic field, likely due to the large springs that support the capsule. The effect of these distortions on the data produced by LSBB is unclear, however it may effect the long term stability of the site's measurements. While the data produced at this facility is world class, unfortunately it is also unique and it would be very difficult to replicate these conditions elsewhere in the world. This indicates the need to find a simpler way of deploying SQUID magnetometers around the world for geomagnetic measurements.

[1]English translation: Low Noise Underground Laboratory

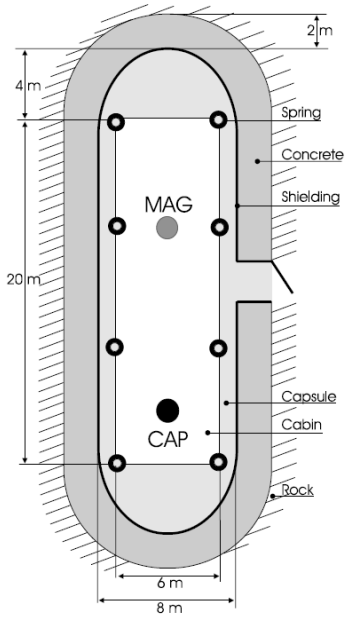


Figure 4: Diagram of shielded LSBB SQUID capsule. 'MAG' shows the position of the SQUID magnetometer [1].

### 1.2.3 Kanazawa Institute of Technology

All the information in this section has been obtained from a publication by the Kanazawa Institute of Technology [2]. The institute built a prototype SQUID system with the intention to detect magnetic signals caused by earthquakes and earthquake precursors. This was in part motivated by successful measurements of geomagnetic signals at LSBB. Their system is comprised of a three axis LTS SQUID placed in a 35 litre cryostat (see Figure 6). This allowed the system to run continuously for a month without needing to be refilled. The cryostat was placed in a hole on the ground floor of the laboratory inside a wooden structure. A direct readout Phase Locked-Loop (PLL) system was used and the SQUID readout was connected to an amplifier circuit, an analogue filter and finally a commercial 16-bit data logging system. The SQUID was placed inside an electromagnetic low-pass shield which attenuated signals above 500 Hz.

The noise levels were measured at 15 fT/$\sqrt{Hz}$ and 2000 fT/$\sqrt{Hz}$ at 100 Hz and 0.01 Hz respectively. The dynamic range was found to be $\pm$ 150 nT with a resolution of approximately 15 pT, mostly limited by the data logging system. A GPS unit was used to time stamp the data. The system was able to successfully detect Pi2 pulsation of the Earth's magnetic field, see Section 2.4 for more details on this phenomenon. It should be noted that both this system and the LSBB system makes use of a LTS SQUID which requires liquid helium for cooling. Liquid helium is significantly more expensive that the liquid nitrogen required for a HTS SQUID system. The major advantage for using a LTS SQUID is the increase in sensitivity and reduction of the noise floor. However, given the properties of liquid helium, it may be impractical to use for a remote station. The research presented in this thesis thus investigates the feasibility of using a liquid nitrogen based HTS SQUID and will compare the findings to the LTS SQUID. Regardless of the result, it should be noted that the HTS SQUID is still significantly more sensitive than traditional fluxgate magnetometers, and may still be a practical alternative to the LTS SQUID.

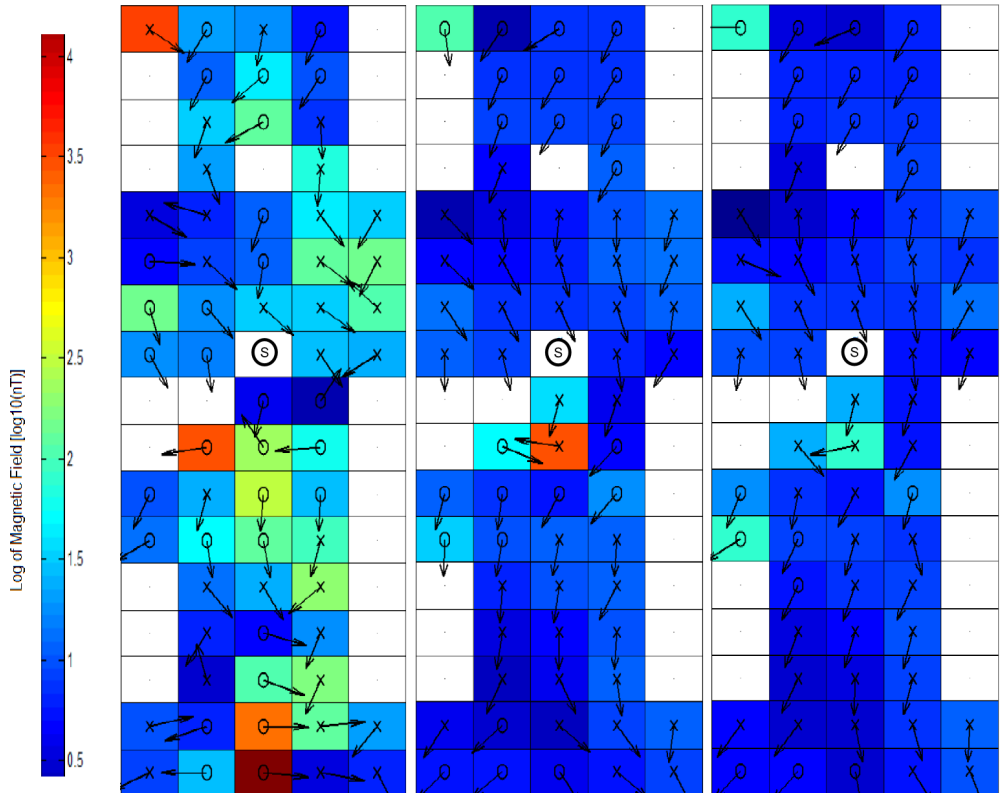


Figure 5: Magnetic vector map of LSBB capsule taken with a LEMI-11 magnetometer, showing distortion of the magnetic field in the SQUID environment. The grid has a spacing of approximately 1m. The colour shows the magnitude of the magnetic flux while the arrow shows the horizontal direction of the field while the 'o' and 'x' shows the vector out and into the page respectively. The 'S' shows the position of the SQUID. The figures show the measurements at a height above the capsule floor of 0.2 m, 1.0 m, and 1.4 m starting from the left.

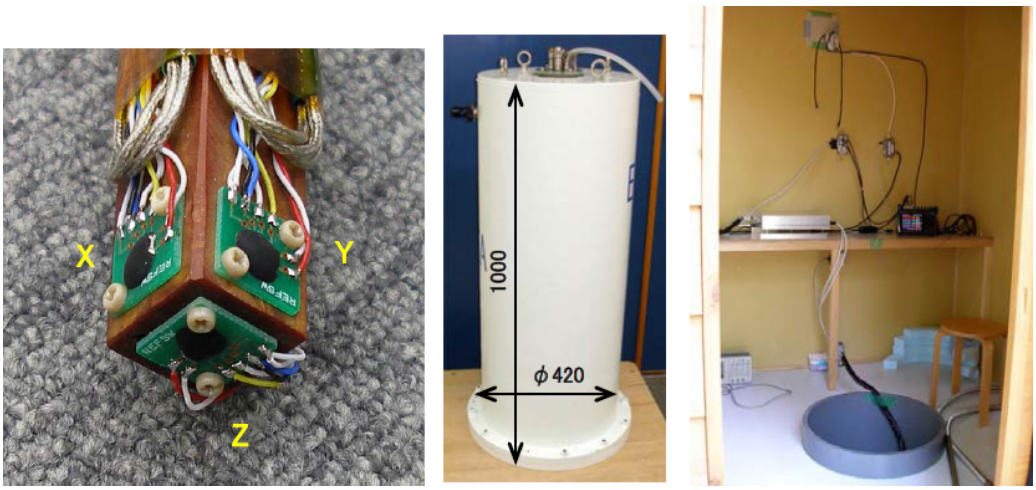


Figure 6: Kanazawa Institute of Technology SQUID system showing (left) 3-axis SQUID magnetometer, (middle) cryostat, (right) inside experimental facility [2].

# 2 Geomagnetism

This section provides and overview of geomagnetism. It lists and briefly describes the typical signals that would be of interest to a SQUID station as well as giving a general overview of geomagnetic signals.

## 2.1 Structure of the Atmosphere and Ionosphere

The atmosphere can be divided up into several layers according to its physical properties. The temperature gradient is typically used to define the layers of the atmosphere [3]. According to this scheme, the atmosphere has four layers: the troposphere, stratosphere, mesosphere and the thermosphere as seen in Figure 7.

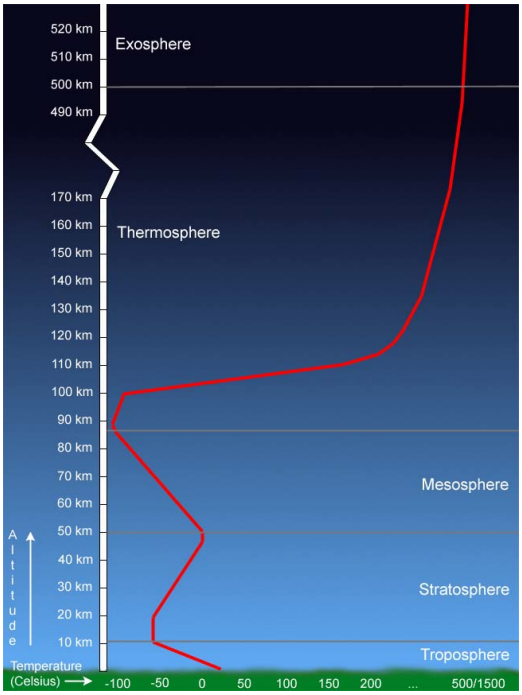


Figure 7: The different layers of the atmosphere. Different regions are defined according to how the temperature changes [3].

Each layer is separated by a boundary that is designated by the suffix *-pause*, thus the mesopause is the boundary between the mesosphere and the thermosphere. In the troposphere the temperature decreases linearly with altitude, however starting at the tropopause the temperature starts to increase once again. This region is called the stratosphere. It contains the ozone layer and extends all the way to the mesosphere. The heating occurs due to the ozone layer absorbing ultraviolet radiation from the sun and converting the incident photon's energy into thermal energy [3]. The mesosphere contains similar ratios of nitrogen and oxygen as the troposphere and hence cannot absorb ultraviolet radiation very well. As a result the temperature decreases with altitude again due to adiabatic cooling. Finally, the uppermost layer of the atmosphere is called the thermosphere, due to it being the hottest of all the layers. The increasing temperature is again caused by radiation absorption from the sun. The radiation causes the gas molecules to become ionized and the density is low enough to ensure that interactions between the ions are rare, leading to a permanent ionized layer. This layer of ionized gas is called the ionosphere and is significant in this thesis as the majority of the magnetic signals of interest are in

some way related to the ionosphere.

The ionosphere was first postulated by A. E. Kennelly and O. Heaviside in 1902 to explain why G. Marconi was able to broadcast a radio signal across the Atlantic Ocean [4]. Radio signals require line-of-sight, and cannot be transmitted through the Earth. Europe and North America are far enough apart that the curvature of the Earth would block and direct radio transmission. Thus, it was concluded that there must be a reflecting layer in the upper atmosphere which the radio signal could bounce off of and reach North America. It was proposed that a layer of conducting ionized gas in the upper atmosphere could be responsible for this reflecting layer.

It was only in 1925 that the existence of the ionosphere could be verified by E. V. Appleton and M. A. F. Barnett in the United Kingdom and G. Breit and M. A. Tuve in America [4]. Breit and Tuve would broadcast short radio pulses and measured the time it took for the pulses to return, since the speed of light is fixed, they could use this to measure the distance to the ionosphere. This method is still in use today, and by varying the frequency of the transmissions, different layers of the ionosphere can be probed. Appleton used the letter E for the electric vector of the reflected radio wave, when he found a refection coming from a higher layer he used the letter F, and occasionally he received a reflection from a lower level and naturally labelled this region as D. These layers are illustrated in Figure 8. The different layers of the ionosphere are due to the layers of the atmosphere responding differently to incoming radiation from the sun [4]. Thus, as the intensity of various radiation types change, the electron density in these layers will change accordingly.

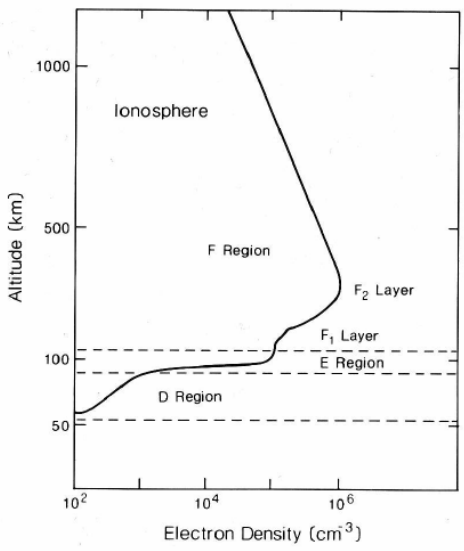


Figure 8: The different layers of the ionosphere at their typical altitudes. The different layers are characterised based on the electron density of the region [4].

The ionosphere is formed when the high-energy photons (mostly UV and X-rays) from the sun ionize the upper atmosphere's gases (such as $N_2$, $O_2$ and O) in a process known a photoionization. When the energy of an incoming photon is greater than the ionisation energy of a neutral molecule, and that photon gets absorbed, then the transferred energy is enough to cause an electron to be expelled from its orbit around the nucleus, hence ionising the molecule. This process begins when the sun rises, then the photoionisation rate gradually increases as the Sun makes its way to the highest point in the sky, when photoionisation is maximum. When the

sun sets, the intensity of the incoming solar radiation and photoionisation rate decreases. As the ions interact, they will recombine to form neutral molecules again and the electron density will decrease over time. This gives rise to the daily variations in ion density [4].

A second cause of ionisation is cosmic rays. These rays are actually high energy particles that originate from the sun, the magnetosphere, the galaxy, or the ionosphere itself. If the kinetic energy of the particle is greater than the ionisation energy of a neutral molecule, and a collision takes place, then there is a chance that the transferred energy will be great enough to ionize the molecule [4].

The actual interaction between the incoming radiation and the upper atmosphere is significantly more complex than described here, however for this thesis it is sufficient to understand that there is a correlation between solar activity and the ion density in the ionosphere. Thus, by monitoring the magnetic fields generated by the dynamic ionosphere, it is possible to monitor interactions between the solar wind and the ionosphere.

## 2.2 Solar-Quiet Variation

The diurnal variation of the magnetic field is the most studied and well understood of all known magnetic field perturbations. This variation is caused by the interaction between solar radiation and the upper atmosphere. As the ion density changes throughout the day due to solar radiation, currents are also formed. These currents cause magnetic fields, seen in Figure 9, which can be detected from ground based magnetic observatories.

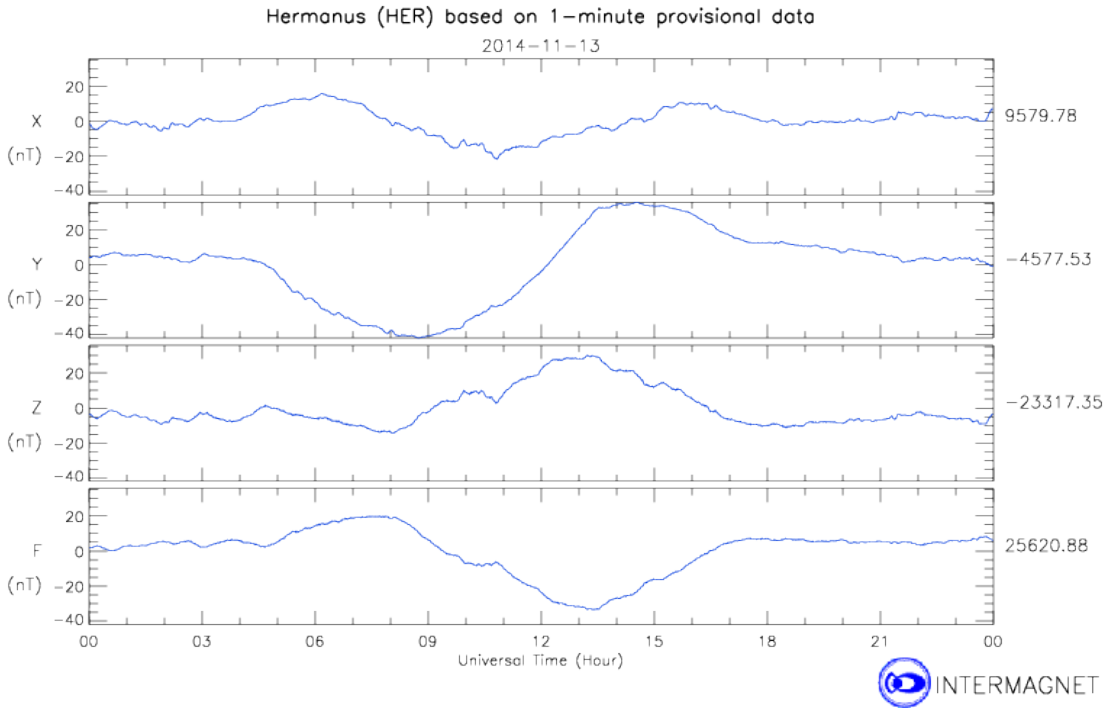


Figure 9: The magnetic field components at SANSA showing the daily variation for 13 November 2014. The X component points due north, Y is directed east, and Z points downward, while F is the total magnetic field [5].

Stations at the same magnetic latitude record similar patterns but delayed by the time of day. The pattern has considerable symmetry with respect to the magnetic equator and local noon. This suggests that the diurnal variations are due to ionospheric currents driven by the sun. These currents are shown in Figure 10 during

equinox [4]. The figure shows two cells of circular current located at about 30 degrees North and South of the magnetic equator.

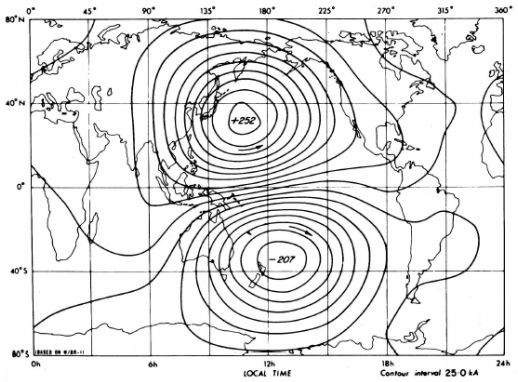


Figure 10: Ionospheric current system responsible for the diurnal magnetic variations. The figure shows the typical currents during equinox with the contour interval of 25 kA [4].

Kivelson and Russell [4], showed through Fourier analysis that the variation is primarily solar diurnal. Interestingly enough, there is also a weak lunar semidiurnal pattern with a period of 12h 25 min. The primary cause of the diurnal variation is a dynamo created by motion of electric charges in the ionosphere across the Earth's magnetic field lines. This motion is driven by winds in the ionosphere, which in turn are caused by solar heating and lunar and solar tides. The dominance of the diurnal component suggests that it is primarily due to solar heating [4].

## 2.3 Solar Wind and the Magnetosphere

The sun is at the center of our solar system and is driven by a fusion reaction at its core. This reaction creates vast quantities of plasma that makes makes up the bulk of the sun. A plasma is simply an ionised gas, that is to say some of the electrons have been stripped away from the positive nuclei. Massive convection currents cause the plasma to move through the sun and in turn generate complex magnetic fields. The sun also continuously emits plasma at speeds of around 450 km/s, known as the solar wind. As the solar wind moves through interplanetary space it generates its own magnetic field known as the Interplanetary Magnetic Field (IMF) and typically it either points "North" or "South".

The Earth's magnetic field can be approximated by a dipole that is tilted at an angle of approximately 20 degrees to the rotational axis. The magnetic field vector leaves the Earth at the South pole and enters at the North pole. The magnetic field extend far out into space and forms what is called the magnetosphere. Far from being a dipole, the magnetosphere is compressed on the day side and elongated on the night side by the influence of the solar wind. If the IMF generated by the solar wind is North facing then the plasma will be deflected around the Earth's magnetosphere with little impact on the Earth. If, however, the IMF points southward then a process known as magnetic reconnection occurs and the plasma can penetrate the Earth's inner magnetosphere leading to the day-side aurora. As the reconnected field lines fold back onto themselves in the magnetotail, reconnection occurs on the night side and more energy and plasma is injected into the inner magnetosphere. This gives rise to the night-side aurora. These short-lived disturbances, which usually only last

for a few hours [6], are called magnetic substorms and their magnetic signatures are usually only detectable at high latitudes. This is because the solar wind is deflected by the Earth's magnetic field and enters the upper atmosphere at the poles where it produces a magnetic disturbance. Hence, the further the station is from the poles, the harder it is to detect these disturbances. Before substorms are discussed in more detail, a brief explanation of magnetic reconnection is presented.

Magnetic reconnection is a complex process and is thought to be the primary mechanism by which energy is exchanged between the solar wind and the magnetosphere. As highly conductive plasma flows, it generates its own magnetic field and forms "flux tubes". A flux tube is a cylindrical shape whose sides are defined by magnetic field lines. Thus, the magnetic flux and the plasma move together as a single entity in large "threads". If two of these threads, with magnetic fields in anti-parallel, meet then reconnection can occur. During reconnection the plasma streams rearrange themselves and form new flux tubes. During this process, large amount of magnetic energy is converted to kinetic and thermal energy, and it is believed that this process is responsible to the sudden heating of solar flares [4].

On the surface of the sun, the flux tubes often forms a massive loop called a solar prominence. If this loop is forced together and magnetic reconnection occurs, then a new isolated loop forms and gets repelled from the sun at high velocity due to the energy exchange that occurs during reconnection. This ejected mass is appropriately named a Coronal Mass Ejection (CME).

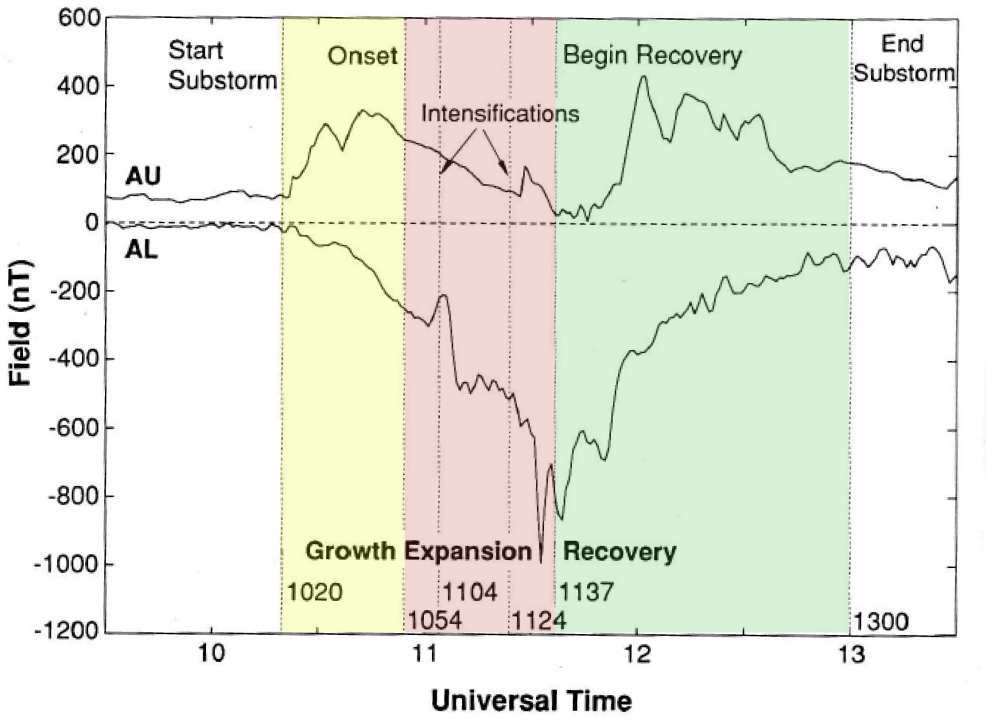


Figure 11: A magnetic substorm is caused by a brief South facing IMF which injects energy into the inner magnetosphere through magentic reconnection. This gives rise to the shown sequence of events. Adapted from [4].

We now turn our discussion back to substorms. Figure 11 shows the typical sequence of events during a

magnetic substorm. It describes how two substorm indices, AL and AU, change with time. These and other indices are used to measure the strength of the auroral electrojets (high altitude plasma streams). The AU index is defined at any instant as the maximum positive disturbance recorded by any station in a chain of observatories, while AL is defined as the minimum disturbance.

During the growth phase, the size of the polar cap (the ionosphere above the magnetic poles) increases, as well as the probability of weak intensifications of the aurora and electrojet. Bursts of Ultra-Low Frequency (ULF) waves called Pi-2 pulsations can also occur, see Table 2. During this phase, the energy from the solar wind is being stored in the magnetosphere, rather like thunderclouds building in the atmosphere. It is then followed by the expansion phase when the stored energy is released. Once this energy is expended, this is followed by the recovery phase when magnetospheric conditions return to normal. Typically these disturbances have amplitudes ranging from 200 to 2000 nT and last between 1 and 3 hours [4].

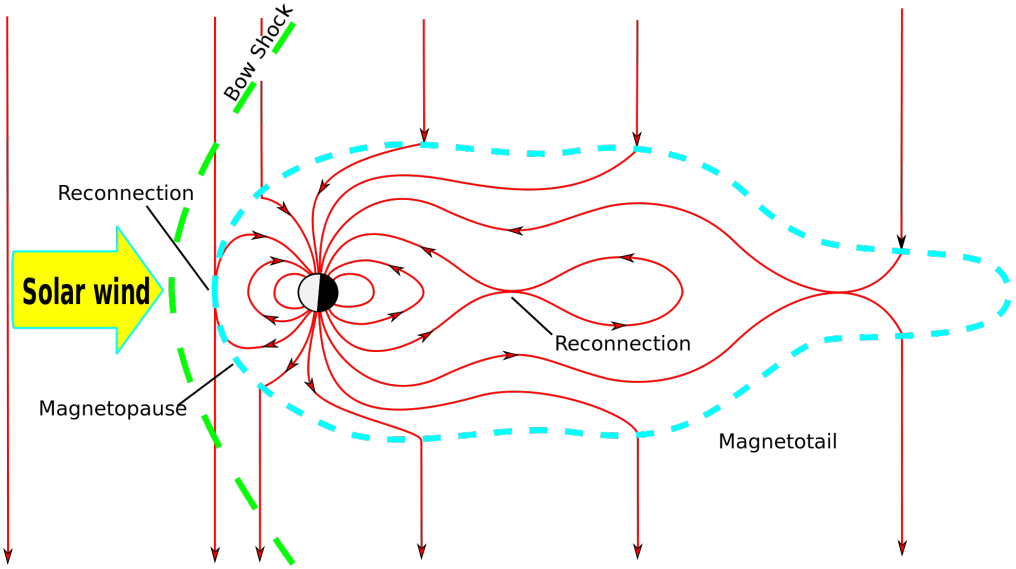


Figure 12: The Earth's magnetosphere is compressed by the solar wind on the day side. The boundary between the interplanetary medium and the magnetosphere is called the bow shock, while the elongated tail is naturally named the magnetotail. When oppositely directed field lines meet, the plasma which they contain merge in a process called magnetic reconnection which injects large amounts of energy and plasma into the inner magnetosphere [7].

If the IMF points southward for long periods of time, it gives rise to more powerful geomagnetic storms. While the field is pointing southward, plasma keeps being injected at the poles and forms a ring around the equator. The injected protons move in a westerly directions, while the electrons move in an easterly direction. The movement of these charges around the equator forms a ring current around the Earth. The ring current causes large decreases in the horizontal component, H, of the Earth's field over most of its surface area. As long as the IMF remains southward more particles are injected into the ring current, which will cause it to grow asymptotically in strength. Figure 13 shows the typical $D_{st}$ index for a magnetic storm. The index is an acronym for Disturbed Storm Time, and is an indication of the deviation in strength of the ring current around the equator. Zero signifies an unperturbed ring current, while negative numbers indicate a weakening of the

Earth's horizontal magnetic field at the equator due to the ring current (this is where it is typically measured) [8].

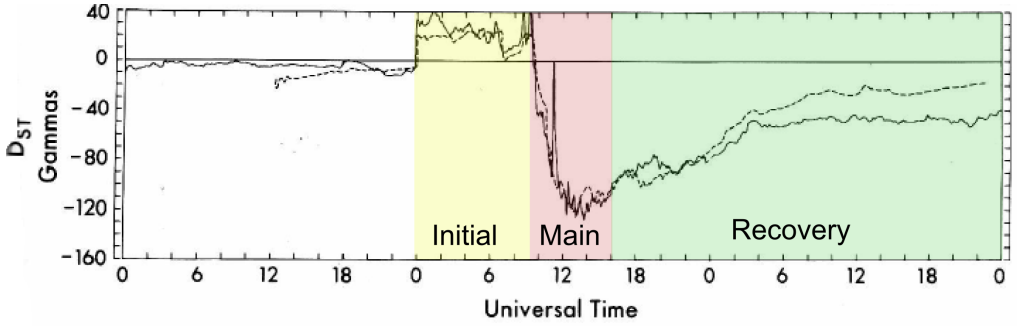


Figure 13: Measurements of magnetic field caused by equatorial ring currents during the 15-17 February 1967 magnetic strom. Adapted from [4].

Not all storms are preceded by an initial phase where the H component is increased. This increase is not related to the ring currents that form and occurs when the solar wind compresses the Earth's day side magnetic field, enhancing the the magnetopause currents and thus resulting in a positive increase in the global H component at the Earth's surface. The compression of the field is called a *sudden impulse* and lasts as long as the IMF is pointing northward. Eventually, when the IMF turns southward, the Earth's magnetic field gets peeled back through a series of reconnections and particles and energy can penetrate the inner magnetosphere and feed the ring currents. This is the start of the *main phase* of the storm.

During this phase, the ring current grows as the southward facing IMF keeps feeding plasma into the inner magnetosphere. When the IMF eventually weakens or turns northward, the Earth's field can close up again and prevent the solar wind from penetrating the magnetosphere. At this point the ring currents stop growing and the storm enters the *recovery phase*. Without a new supply of ions, the ring current slowly dissipates as the ions recombine to form neutral atoms.

Typically storms last between 1-5 days with the initial phase lasting up to 25 hours, the main phase approximately 1 day, and the recovery phase several days. The Dst index is a measure of the effect that the ring current around the equator has on the H component at the surface of the Earth. Storms with Dst of 50 to 150 nT occur almost every month, while a Dst of 150 to 300 nT occur several times per year, and a storm with a Dst of 500 nT or greater only occur a few times per solar cycle [4].

## 2.4 ULF Waves

Ultra-Low Frequency (ULF) waves typically have periods ranging from 1 to 1000 seconds and originate in the plasma of the upper atmosphere. These waves are called geomagnetic pulsations and have been grouped into categories based on their period and how stable they are, as seen in Table 2. Furthermore by studying these pulsations a large variety of observations about interactions between the solar wind and the ionosphere can be made [9].

In 1963 an International Association of Geomagnetism and Aeronomy (IAGA) committee classified these waves into various categories [4]. The continuous pulsations are quasi-sinusoidal and each has a well defined

spectral peak. These are called Pc pulsations due to their *continuous* nature. Each Pc type is characterised by a specific frequency band as shown in Table 2. Other pulsations are not regular and span multiple frequency bands. These are classified as Pi pulsations due to their *irregular* nature. The waves caused by these pulsations known as Alfvén waves, after Hannes Alfvén, who received the Nobel Prize for his discovery and description of these waves [4].

The plasma of the upper atmosphere tends to get frozen in along the magnetic field lines of the Earth. This creates long plasma strings that follow the magnetic field lines from North to South. Similar to a musical string instrument, if these "strings" are perturbed due to an external force like the solar wind, they will tend to oscillate at their resonant frequencies. The resulting motion of the charged particles locking into this "string" will generate ULF waves that are detectable from ground based observatories [10]. At SANSA the main pulsations that are detectable are the Pc-3 and Pi-2 pulsations.

## 2.5 Schumann Resonances

The surface of the Earth and the ionosphere can be approximated by a conductive sphere and shell respectively. The cavity between these two layers creates a wave guide that can support a variety of resonant frequencies called Schumann resonances. An example spectrum is shown in Figure 14.

The Schumann resonances are classified as Extremely Low Frequency (ELF) signals and have their peaks at approximately 8, 14, 20, 26 and 32 Hz [11]. To detect them using conventional antennae would be impractical due to their large wavelengths, thus observers usually attempt to detect either the magnetic- or electric field variations using dedicated sensors. These devices need to be sensitive enough to detect signals which are in the mV/m range for electric, and pT range for magnetic fields [11]. The SQUID magnetometer is thus ideally suited for observing this phenomenon due to its low noise and high sensitivity.

The energy to stimulate these resonant frequencies is believed to enter the global wave guide through lightning storms [11]. Thus, studying the Schumann resonances gives valuable insight into global lightning patterns or large scale changes in the ionosphere. This in turn can be used to indirectly monitor other global climatic conditions. As the global climate changes and temperatures rise, it is expected that lightning activity will increase. This in turn will inject more energy into the earth-ionosphere wave guide and increase the magnitude of the Schumann resonances [11].

## 2.6 Earthquake Precursors

Electromagnetic signals associated with earthquake precursors are very difficult to detect and tend to be inconsistent. Typically earthquake precursor signals are in the ULF band and are defined as anomalous signals that occur before a seismic event. Precursors are different from coseismic signals that occur at the same time

| | **Pc-1** | **Pc-2** | **Pc-3** | **Pc-4** | **Pc-5** | **Pi-1** | **Pi-2** |
|---|---|---|---|---|---|---|---|
| **Period [s]** | 0.2-5 | 5-10 | 10-45 | 45-150 | 150-600 | 1-40 | 40-150 |
| **Frequency [mHz]** | 200-5000 | 100-200 | 22-100 | 7-22 | 2-7 | 25-1000 | 2-25 |

Table 2: Ranges of periods and frequencies for different pulsation classes [4].

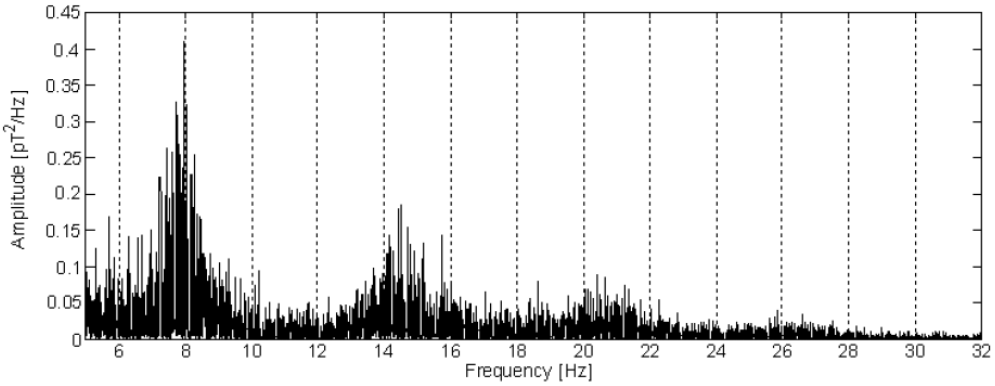


Figure 14: Schumann resonances in a sample spectrum of ELF natural electromagnetic signal recorded at Mitzpe Ramon (32N, 34E) station in Israel [11].

as the earthquake due to a release of stress or strain on the rocks. The ultimate goal however is to be able to detect precursors reliably to act as an early warning system. To date, this has proven to be very difficult due the complex nature of the phenomenon.

In laboratory experiments, it has been shown that electric fields develop as fluid flow through rocks change, and both resistivity and magnetisation change with the stress on the rocks [12]. Unfortunately field experiments have been less successful. In field measurements, the fields generated before an earthquake are sometimes larger than expected based on models developed from laboratory experiments. Other times ULF waves are not present at all, or they are detected with no seismic event associated with it. Before a practical seismic precursor system can be deployed, a better understanding of the underlying phenomenon as well as the structure of the Earth's crust needs to be attained [12]. The SQUID magnetometer is significantly more sensitive than any of the instruments used to date to study this, and it may reveal something that the other detectors missed.

Generally there are two types of observations that are made when studying precursors. The first observation is a change in the material properties of the rock, such as resistivity, while the second is a change in the amplitudes of natural signals that may be present, such as magnetisation. Magnetic field variations have been associated with earthquake precursors. Prior to the mid-1960s there were many false reports due to disturbances in the ionosphere or the magnetosphere, but as measurement techniques and technologies improved, so has the quality of reporting [12].

Proton Precession Magnetometers are commonly used to detect the magnetic signals which are typically in the quasi-DC to 10 Hz frequency range with signal amplitudes less than 25 nT. Shapiro and Abdulabekov issued a warning for a M7.0 earthquake in 1982 on the basis of a 23 nT anomaly 3 days before the earthquake which was based on the difference in fields between two observatories [12].

Johnston and Mueller reported DC offsets of the total magnetic field of about 1 nT which were associated with both the M5.9 North Palm Springs and M7.1 Loma Prieta earthquakes in 1987 and 1990 respectively. They concluded that this was due to piezomagnetic effects due to stress removal on the rock [12].

These signals are in the same bandwidth as many other geomagnetic signals and it can be very difficult to determine which are genuine seismic signals and which are due to background variation. In order to have any chance of success, a large number of monitoring stations are required to reduce the influence of large scale

magnetic variations due to the ionosphere, similar to the $D_{st}$ index.

## 2.7 Seismic-Ionosphere Coupling

When an earthquake occurs it produces a series of shockwaves. The P-waves are compression waves, similar to sound waves, and can couple into the atmosphere. These waves take approximately 300 seconds to reach the upper atmosphere where they excite a resonance mode in the ionosphere. The oscillating ions in turn generate a magnetic field which can be detected using a SQUID magnetometer. These damped oscillations typically have a period of between 60 and 90 seconds and, because of their large wavelength, appear as a near-field source when observed from anywhere on Earth [13].

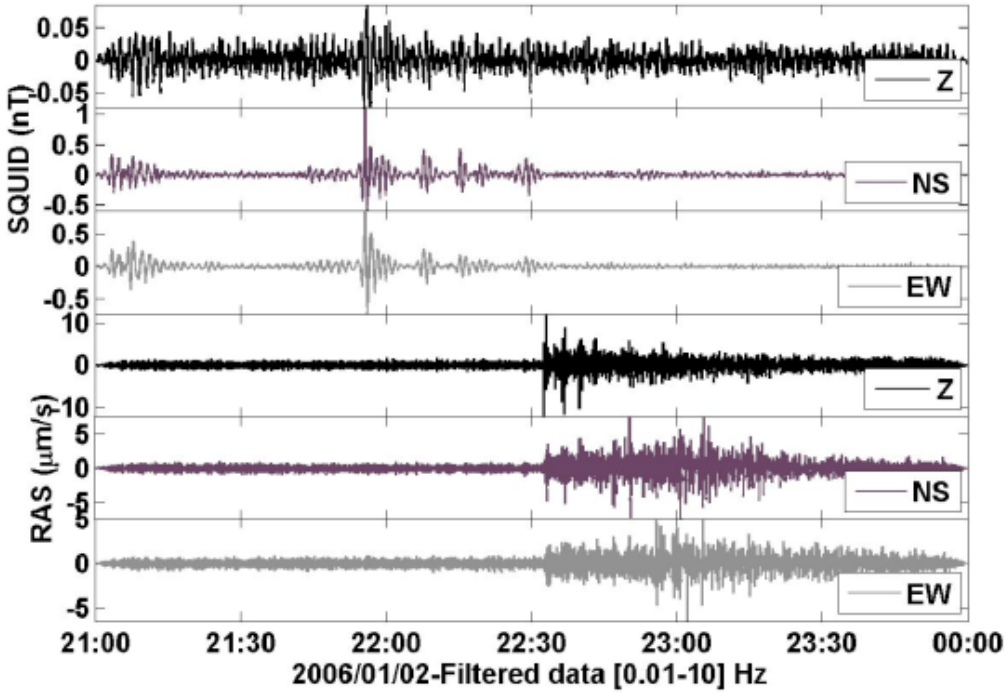


Figure 15: Simultaneous recordings of the reference magnetometer in the bottom three windows and the $[SQUID]^2$ system at LSBB in the top three on 2 January 2006. Several damped magnetic oscillation trains are occurring during a seismically calm period interrupted at 22h32 by the arrival of PKP waves from a M=7.2 earthquake near the Fiji Islands [13].

LSBB has managed to observe this phenomenon as seen in Figure 15. If Rustrel is not in the shadow-zone of the seismic waves, then a second smaller mesopause excitation can sometimes also be detected approximately 300 seconds after the P-wave is detected on the local seismometers.

The resonance of the mesopause can also be excited by a string electric field as observed by the $[SQUID]^2$ for one hour before the SichuanWenchuan quake in May 2008. Before the earthquake, the electric field intensity was so great that amateur footage showed rainbow coloured bands in the sky several hundred kilometres away from the epicentre (see Figure 16). The amateur video was analysed and the light phenomenon was in coincidence with the magnetic signals detected at LSBB. At the time when the first oscillations were detected, there had been no earthquake and during the whole hour only two quakes with Mw $>$ 3 occurred worldwide.

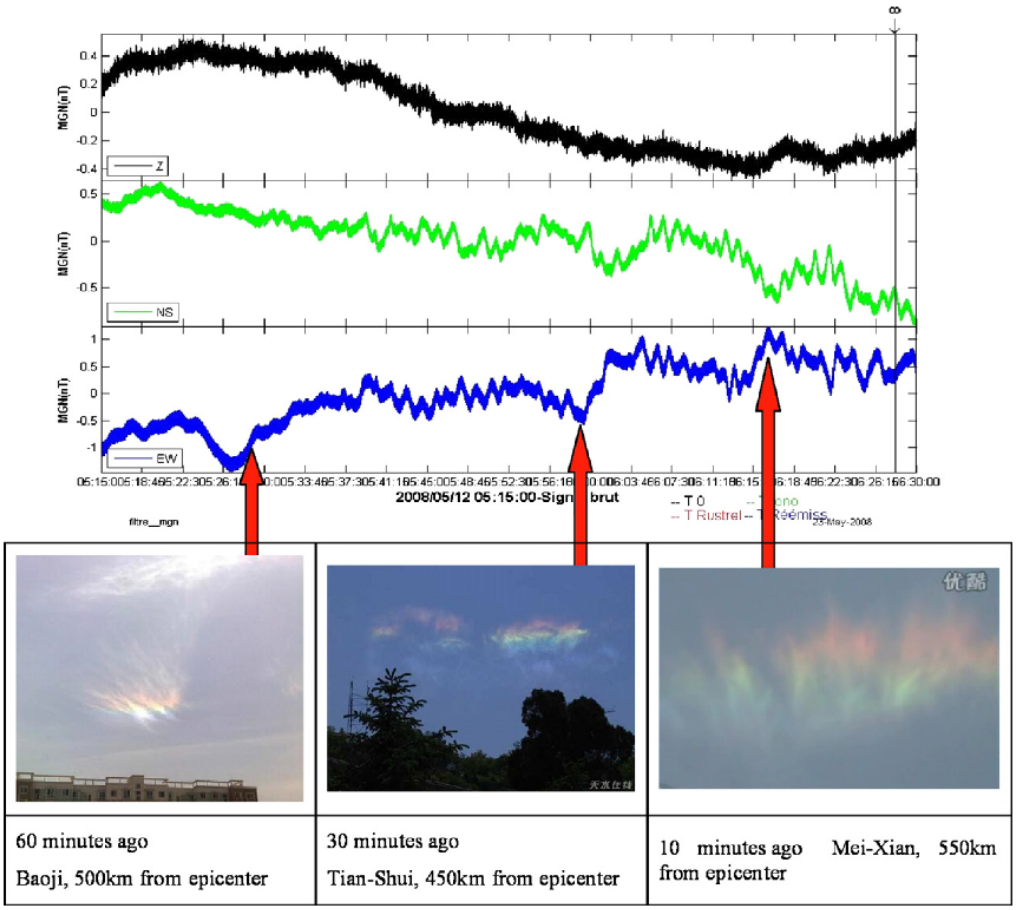


Figure 16: LSBB SQUID signal traces with amateur video footage near epicenter of SichuanWenchuan quake in May 2008. The traces show a clear oscillating signal at the same time as the aurora starting about an hour before the earthquake.

# 3 Superconductivity

This section provides a broad overview of superconductivity in order to provide a basic understanding of how the SQUID sensor works in Flux Lock Loop (FLL) mode. Thus, the theory will not be treated with the full mathematical rigour required to understand the quantum nature of this phenomenon. However, the contents of this thesis does not require that level of understanding and a simpler explanation that promotes clarity is more beneficial.

## 3.1 Brief History

Unless otherwise stated the material in this section is drawn from the text by Orlando[14]. Superconductivity was not observed until the early part of the twentieth century. Materials need to be cooled to extremely low temperatures, less than a few degrees Kelvin for pure metals, before they become superconducting. The equipment needed to cool the material sufficiently was not available before this time. This example supports my earlier statement that without advances in technology, new discoveries are sometimes impossible.

Cryogenics was born out of the desire to study the behaviour of gasses at low temperatures. By 1898, James Dewar was able to liquefy hydrogen at a temperature of 20 K, and helium remained the only element not to be liquefied. The technological challenge posed by liquefying helium attracted the attention of many researchers world wide. Heike Kamerlingh Onnes began his liquefaction program in 1882 in the Netherlands. It took his lab 16 years to discover a method of successfully doing so, and by 1908 his team had managed to produce liquid helium at a rate of 0.28 litres per hour. This process required the development of the most sophisticated cryogenic technology at the time and for many years Kamerlingh Onnes' laboratory dominated the field for many years.

Liquid Helium is an important cryogenic liquid as its boiling point is extremely low, 4.2 K. This enables cryogenic research in low, stable temperature environments by simply immersing the material under investigation into a bath of liquid helium. Onnes used this method, still in use today, to study the electrical resistance of metals at low temperatures. Originally his studies began with platinum and gold, but he was concerned that impurities in the metals were causing errors in his experiments. He thus decided to change the material to mercury. Mercury is a liquid at room temperature and hence standard distillation processes can be used to produce ultra-high purity samples. The distilled mercury was placed in glass capillary tubes and immersed in liquid helium for his experiments.

In 1911 one of Onnes' assistants, Gilles Holst, immersed a sample of mercury and measured the resistance curve as shown in Figure 17. The curve shows an abrupt change in the resistance of the sample down to zero at a particular temperature. The fact that the resistance becomes immeasurably small was not in itself surprising, but the resistance was expected to approach zero in a smooth manner as the temperature was reduced, not drop suddenly. Onnes was suspicious of the result and performed the experiment many times. Only after several more samples were tested, and similar behaviour was observed, did Onnes report that below a critical temperature, "the mercury passes into a new state, which on account of its extraordinary electrical properties may be called the superconducting state" [14]. What Onnes had discovered is today called the critical temperature, $T_c$, of the material. The critical temperature is a property of the material itself, below which it becomes superconducting.

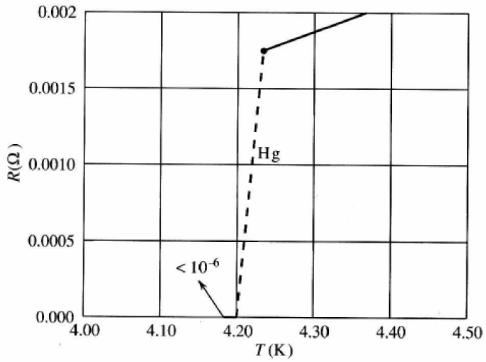


Figure 17: Resistance-Temperature graph showing the transition of mercury into the superconducting state at approximately 4.2 K. [14].

In 1913, Onnes had won the Nobel Prize in Physics for his research into the properties of materials at low temperatures. In the same year it was discovered that there was a threshold value of the current density that can be carried by a superconductor. This is called the critical current density, $J_c$, beyond which the material loses its superconductivity. Onnes found experimentally that this quantity was a function of the temperature of the superconductor. As the temperature is lowered, the critical current density increases linearly as shown in (3.1) up to some maximum value $J_{co}$, which is dependant on the material,

$$J_c(T) = J_{co}\left(\frac{T_c - T}{T_c}\right), \text{with } T <= T_c. \tag{3.1}$$

Similarly he found that the superconducting state can also be destroyed by applying a strong enough magnetic field to the sample. This maximum field value is called the critical field, $H_c$, and a sample exposed to a stronger field loses its superconducting properties. This value is also dependent on the temperature of the material. The lower the temperature of the material, the higher the critical field became, as shown in (3.2), up to a maximum value of $H_{co}$ at 0 K. This behaviour is shown for several materials in Figure 18.

$$H_c(T) = H_{co}\left[1 - \left(\frac{T}{T_c}\right)^2\right], \text{with } T <= T_c. \tag{3.2}$$

As cryogenic technology developed and became more common in the 1920s, more and more laboratories started to study superconductivity. The next major discovery was made by Walther Meissner and Robert Ochenfeld in 1933 while experimenting with single crystals of tin. They found that for low magnetic fields, a superconductor does not conserve the amount of magnetic flux as a perfect conductor would, but rather it expels that flux. If the magnetic flux was lower than the critical field, Meissner and Ochenfeld found that the flux density inside the bulk of the material was essentially zero. A material that minimises the amount of magnetic flux inside it is called a diamagnetic material. Thus, since the flux inside a superconductor is zero, it is called a perfect diamagnetic material. This property is caused by what is today known as the Meissner effect (see Section 3.2). This effect shows that superconductivity is more than simply zero electrical resistance and any theory attempting to describe it needs to take this phenomenon into account.

The search for materials with higher critical temperatures continued slowly, and it was only in January 1987 that Paul C. W. Chu and Maw-Kuen Wu demonstrated that $YBa_2Cu_3O_7$ (known as YBCO) has a critical

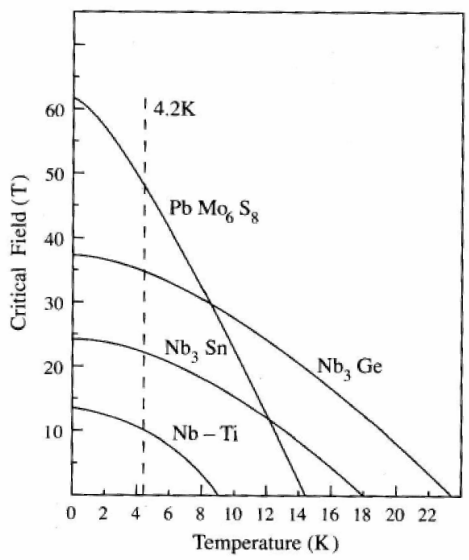


Figure 18: The critical magnetic field strength, $H_c$, of several superconductors as a function of temperature. Each material remains superconducting for fields less than the critical field. Notice that materials with higher critical temperatures tend to have higher critical fields [14].

temperature of 95 K. This discovery was significant because it enabled the use of readily available liquid nitrogen as a cryogen instead of liquid helium, which is expensive and hard to come by. This gave birth to a new class of superconductor known as High Temperature Superconductors (HTS). The SQUID magnetometer in use at SANSA is made from YBCO and hence we only require liquid nitrogen for the device to function which greatly reduces the complexity of the system.

## 3.2 The Classical Model of Superconductivity

The classical model of superconductivity was determined experimentally by Fritz and Heinz London in 1935. Thus the model does not attempt to describe how superconductivity works, but rather provides a mathematical description of the observed phenomena. In particular it describes the relationship between voltages and alternating currents in the superconductor, as well describing the Meissner effect. The classical model can be used in many problems, but under certain conditions the model is longer be valid and a more advanced theory must be considered, such as the macroscopic quantum model of superconductivity discussed in Section 3.3.

Equation 3.3 is called the First London equation, and can be thought of as an equivalent of Ohm's Law for superconductors:

$$\mathbf{E} = \frac{\partial}{\partial t}(\Lambda \mathbf{J}_s), \tag{3.3}$$

where,

$$\Lambda = \mu_0 \lambda^2 = \frac{m_s}{n_s q_s^2}, \tag{3.4}$$

and $\mathbf{J}_s$ is the supercurrent density, $\lambda$ is the penetration depth of the material while $m_s$, $n_s$, and $q_s$ is

the mass, number, and charge of the superelectrons respectively. Similar to Ohm's law, the First London equation relates the voltage generated across a superconductor to the current flowing through it. There are however a few differences. Ohm's law shows the relationship to be linear and independent of frequency, while (3.3) is frequency dependent. On closer examination, (3.3) is very similar to the voltage developed across an ideal inductor, and indeed superconducting circuits are often simplified to exactly that. In the First London Equation the "inductance" term is represented by $\Lambda$ and is described by (3.4). Earlier it was mentioned that superconductors are perfectly diamagnetic and hence expel all magnetic fields inside the material. The magnetic fields do however penetrate the surface of the material. The penetration depth of the material, $\lambda$, determines how quickly the magnetic field inside a superconductor will decay with distance. As such it is analogous to skin-depth in electromagnetism with the exception that it is independent of frequency. The penetration depth is an inherent property of the superconducting material. For materials such as Nb-Ti and $Nb_3Sn$, as well as high-temperature superconductors, $\lambda$ is typically in the region of 0.1 $\mu$m [14].

Certain properties of superconductors can be modelled by simply making resistive terms zero. However, one of the main differences between a perfect conductor and a superconductor becomes apparent when the magnetic field inside the material is considered. The magnetic field inside a perfect conductor is determined by the initial conditions and changes in external field does not modify the internal field, however inside a superconductor the magnetic field always reduces to zero. Thus, a perfect conductor is a flux conserving medium while a superconductor is a flux expelling medium. This fact is captured in (3.5) and is known as the Second London equation [14]:

$$\nabla \times (\Lambda \mathbf{J}_s) = -\mathbf{B}. \tag{3.5}$$

Essentially it describes how the currents, $\mathbf{J}_s$, inside a superconductor will be established such that they produce a magnetic flux that exactly cancels out the external magnetic flux, $\mathbf{B}$. This describes the Meissner effect and ensures that the magnetic field will not be able to penetrate the bulk of the material. This is similar to how currents are induced according to Lenz' and Faraday's laws. Furthermore, the Meissner effect gives rise to two types of superconductors illustrated in Figure 19.

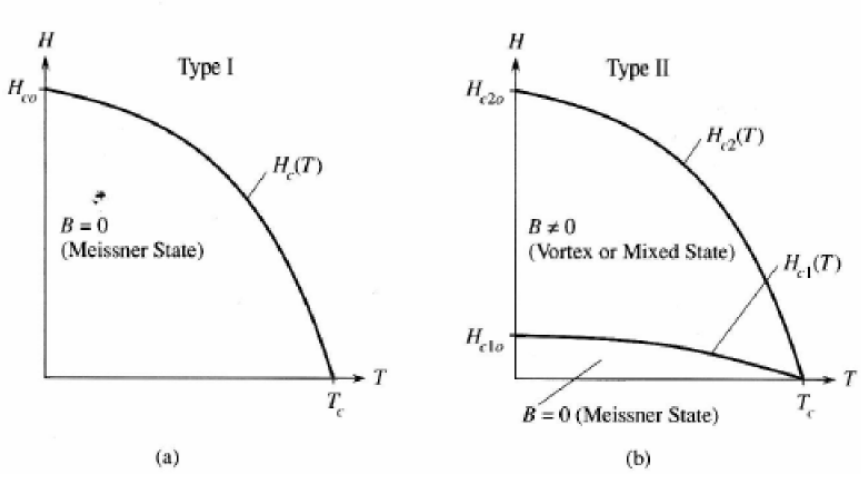


Figure 19: The H-T phase space for a) type I and b) type II superconductors [14]

At applied field strengths less than the critical field, a type I superconductor will expel flux from the material and hence be in the Meissner state. This type of superconductors usually consists of pure elements. They are limited in their usefulness, because these types also tend to have a low critical magnetic flux density [14].

Type II superconductors have a more complex behaviour. They are characterised by two critical field values, $H_{C1}$ and $H_{C2}$, at any given temperature as shown in Figure 19. If the applied magnetic flux is lower than $H_{C1}$, the superconductor will exhibit the usual Meissner effect and expel the flux from the bulk of the material. If the field is greater than $H_{C2}$, then superconductivity will be destroyed in the material. However, for field strengths between these two values, the material enters what is know as a mixed or vortex state. In the mixed state the material no longer exhibits perfect diamagnetism, but rather allows small discrete quantities of magnetic flux to penetrate the material. The flux penetrates the material at concentrated sites, known as Abrikosov vortices, and forms a regular triangular lattice in the material as seem in Figure 20. The flux in each vortex has been found experimentally to always be the flux quantum, $\Phi_0$, which will be described in Section 3.3. These vortices were successfully described theoretically by Alexei Abrikosov in 1957, thus they now carry his name [14]. Since the SQUID at SANSA is made from a type II superconductor, the formation of these vortices are of particular interest as the random motion of these vortices in the HTS SQUID gives rise to instability and low frequency 1/f noise.

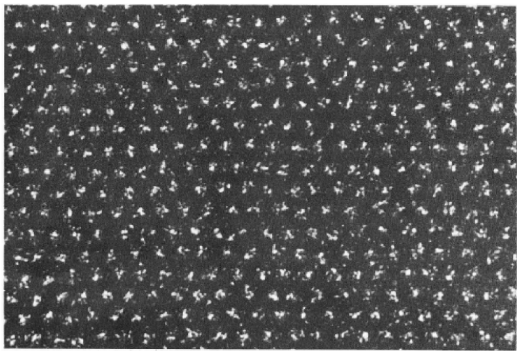

Figure 20: A type II superconductor showing the location of Abrikosov vortices. The photograph reveals the triangular array of vortices formed when a superconducting sample of YBCO is placed in a magnetic field. The applied field strength is 4 mT and the distance between centres is approximately 0.8 $\mu$m [14].

To gain a deeper understanding of why superconductors have a critical field, we must consider an argument from thermodynamics. When a material becomes superconducting, it does so because it is energetically favourable to do so. Thus the free energy in a superconductor, $G_s$, is less than the free energy in a normal conductor, $G_n$. However, since magnetic fields contain energy, it also requires energy to expel the magnetic field. The energy content in a volume due to the presence of a magnetic field is given by,

$$U = \frac{VB^2}{8\pi}, \tag{3.6}$$

where $V$ is the volume and $B$ is the magnetic flux density in that volume. Thus the total change of free energy in the system is given by,

$$\Delta U = (G_s - G_n) + \frac{VB^2}{8\pi}. \tag{3.7}$$

If the change in free energy is negative, $\Delta U < 0$, it implies that changing to the superconducting state will be energetically favourable. However, if the magnetic flux is increased to the point where $\Delta U > 0$ it is no longer beneficial to become superconducting and hence the material will revert back to being a normal conductor [15]. From this the critical field can be derived by simply setting $\Delta U = 0$ and solving for $B$. Doing so yields the equation,

$$B_c = \sqrt{\frac{(G_n - G_s)8\pi}{V}}, \tag{3.8}$$

where the reader is reminded that $B = \mu H$, which links the critical magnetic flux density, $B_c$, to the critical magnetic field, $H_c$. This gives rise to a critical current for a material to remain superconducting. Every current also produces a magnetic field. If the field generated by the current flowing in the material produces a magnetic flux that exceeds the critical field, then the material will revert back to being a normal conductor. The magnetic flux produced at the surface of a circular wire is given by,

$$B = \frac{\mu_0 I}{2\pi r}, \tag{3.9}$$

where $I$ is the current, and $r$ is the radius of the wire. To find the critical current, we substitute the critical flux density, $B_c$, and solve which yields,

$$I_c = \frac{2\pi r B_c}{\mu_0}. \tag{3.10}$$

If the current exceeds this value, the outer layer of the wire will become a normal conductor. This will effectively reduce the radius of the wire, further reducing the critical current. The net result is that the entire wire leaves the superconducting state [15].

The Two-Fluid model completes the description of Classical Superconductivity [14]. In the Two-Fluid model, superconductivity arises when two electrons become bound together in what is known as Cooper pairs, after L.N. Cooper who proposed the concept in 1956. Electrons would normally repel each other since they have the same charge, but in the presence of the positive nuclei in a metallic crystal lattice, these electrons can be bound together through phonon interactions. A phonon is similar to a sound wave, but it operates between the positive nuclei in a crystal lattice. If one nucleus were to move, the electromagnetic forces on the surrounding nuclei would cause them to move as well. Phonons can promote the pairing of electrons by increasing the local positive charge by forcing two positive nuclei closer together as the phonon wave passes. This slight increase in the positivity attracts a nearby electron, thus further binding the two nuclei together. This results in an even greater concentration of the positive charges which in turn can attract a second electron, thus forming a Cooper pair [15]. In this bound state, if the one electron moves, the other one has to move with it because of how they interact with the positive nuclei around them. This behaviour also presents an intuitive understanding for the need to cryogenically cool the material. If the electrons and nuclei have too much thermal energy, their random motions would easily overwhelm the delicate Cooper pairs and the motion of the electrons would remain uncorrelated. The formation of Cooper pairs also helps to understand why the electrons can flow without resistance. In a normal conductor the electrons experience resistance because they scatter off the

vibrating nuclei. In a superconductor, the random motion of the nuclei is reduced and the phonon interaction between the nuclei and electrons can promote the flow of current without "collisions" [15].

In the Two-Fluid model, both electrons and superelectrons are present when the material drops below the material's critical temperature, $T_c$, and as long as the material's temperature does not drop to 0 K, some of the normal electrons will always remain. The electrons and superelectrons are treated as two different fluids inside the superconductor that do not interact with one another. The penetration depth can be related to the number of superconducting electrons through (3.4). If combined with the empirically determined equation,

$$\lambda(T) = \frac{\lambda_0}{\sqrt{1-(\frac{T}{T_c})^4}}, \text{ for T} \leqslant T_c, \tag{3.11}$$

and solving for the number of superelectrons, $n_s$, (3.12) can be derived [14],

$$n_s(T) = n_{s0}\left(1-\left(\frac{T}{T_c}\right)^4\right), \text{ for T} \leqslant T_c, \tag{3.12}$$

where

$$n_{s0} = \frac{m_s}{{\lambda_0}^2 {q_s}^2 \mu_0}. \tag{3.13}$$

Thus, the number of superelectrons increases smoothly and monotonically as the temperature is reduced below $T_c$. Furthermore, we know that the superelectrons make a Cooper pair and hence require two normal electrons to form, thus we can relate the maximum number of superelectrons to the total number of electrons in the material [14],

$$n_{s0} = \frac{1}{2} n_{tot}. \tag{3.14}$$

Thus, the total number of superelectrons can also be written as

$$n_s(T) = \frac{1}{2} n_{tot}\left(1-\left(\frac{T}{T_c}\right)^4\right), \text{ for T} \leqslant T_c. \tag{3.15}$$

This implies that there are two media which can carry electrical current. The lossless superelectrons and the lossy normal electrons. This can be modelled using a lumped circuit model with two parallel branches. One branch contains a resistor and an inductor and represents the normal electrons, the second branch contains only an inductor representing the superelectrons, as shown in Figure 21.

If the circuit is driven by a DC source, then the inductors will appear as short circuits and all the current will flow through the superconducting channel with no loss. If however, the driving frequency was not zero, then a voltage drop would result across both channels, as described by the First London Equation. This in turn would cause a small amount of current to flow through the lossy, normal conducting channel [14].

## 3.3 The Macroscopic Quantum Model of Superconductivity

While the classical model is useful it does not provide much insight into superconductivity, since it is an ad-hoc theory determined from experiment. Superconductivity is based on the classical hypothesis that the electrons do not scatter off the positive atomic nuclei and hence experience no resistance. While having an infinite scatter

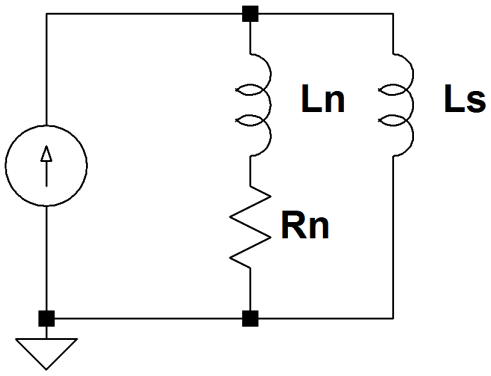


Figure 21: The lumped circuit model for a supercoductor showing a resistor and an inductor in the conducting branch, but only an inductor in the superconducting branch [14].

time does explain the experimental observations, it does not explain why the electrons will never scatter. Fritz London used Schrödinger's quantum wave equation as a possible explanation for supercurrents.

According to quantum mechanics, the movement of electrons, particularly the orbit around the nucleus, can be described by a wave equation. Usually wave equations are used to describe how the amplitude of a wave changes with time and position. This equation can be used to describe the height of a water wave for example. Schrödinger used this equation to describe the probability of a particle occurring at any position in time and space. Thus, a quantum wavefunction does not describe where exactly an electron will be, but rather what the probability is that an electron will be in a particular area at a particular time. This uncertainty is inherent to quantum mechanics and is a fundamental characteristic of the field [16].

In a normal conductor the quantum wavefunctions for each electron is unrelated to any other electron. Thus, there is no quantum phase coherence between the electrons. If a material is cooled sufficiently, this changes. When a material becomes superconducting, a large number of electrons condense into a single quantum state and their phases can be described by a single quantum wavefunction, hence there is coherence on the macroscopic scale [15]. Thus, a single wavefunction can describe the behaviour of an entire group of Cooper pairs. Knowing the phase in one part of the superconductor, automatically tells you the phase in any other part. This is known as a "many-body wavefunction". It is important to realise that the wavefunction does not, and cannot, describe the state of an individual Cooper pair. It only describes the behaviour of the system as a whole since the individual Cooper pairs are constantly being created and destroyed [15]. Similarly a wavefunction cannot be used to describe the motion of an individual water molecule in an ocean wave. Rather it simply describes the height of the entire collection of water molecules that form the wave at any point in time and space. More specifically, the squared modulus of the wavefuction is the density of the superelectrons at a particular point and time [14].

The wavelike nature describing the behaviour of the Cooper pairs also gives rise to flux quantisation. Around any closed superconducting loop, the wavefunction must be single-valued. Thus, any full rotation around a superconducting loop must translate to a $2\pi$ phase shift in the wavefunction. This condition in turn gives rise to the fact that the flux contained inside the loop must be an integer number of the flux quanta $\Phi_0 = 2.07 \times 10^{-15}$Wb. To understand why, consider a free electron's normalised wave function, written as $\Psi(x) = e^{\frac{jpx}{\hbar}}$, where $p$ is

linear momentum along the $x$ axis. From electromagnetism it is known that the momentum of a charged particle in a magnetic field is influenced by the Lorentz force. This is captured in the canonical momentum, $p + qA$, where $p$ is the mechanical momentum, $q$ is charge (-2$e$ for Cooper pairs), and $A$ is the magnetic vector potential. Thus the free electron wavefunction can be written as,

$$\Psi(x) = e^{\frac{j(p+qA)x}{\hbar}}. \tag{3.16}$$

From this equation it can be seen that the phase of the wavefunction is dependant not only on the position, but also on the applied magnetic field from the vector potential term. This is because the vector potential is related to the magnetic flux by the curl of the vector potential, $B = \nabla \times A$

The charge of the Cooper pair is $-2e$, thus the wavefunction becomes,

$$\Psi(x) = e^{\frac{jpx}{\hbar} - \frac{j2eAx}{\hbar}} \tag{3.17}$$

As the Cooper pair makes one complete rotation around the superconducting loop, the first phase term, $\frac{jpx}{\hbar}$, will reduce to zero while the second phase term becomes a line integral of $\frac{2eA}{\hbar}$. Through the use of Stokes' theorem it can be transformed into an area integral of the curl of A over the area enclosed by the loop. This means that the change in phase, $\Delta\phi$, around the loop can be found as follows [15]:

$$\Delta\phi = \frac{1}{\hbar}\oint \vec{p}\cdot\vec{ds} + \frac{-2e}{\hbar}\oint \vec{A}\cdot\vec{ds} \tag{3.18}$$

$$\Delta\phi = 0 + \frac{-2e}{\hbar}\oint \vec{A}\cdot\vec{ds} \tag{3.19}$$

$$\Delta\phi = \frac{-2e}{\hbar}\iint \Delta\times\vec{A}\cdot\vec{da} \tag{3.20}$$

$$\Delta\phi = \frac{-2e}{\hbar}\iint \vec{B}\cdot\vec{da} \tag{3.21}$$

$$\Delta\phi = \frac{-2e}{\hbar}\Phi. \tag{3.22}$$

Since we know that the phase change around the superconducting loop must be a multiple of $2\pi$ we can take the above calculation further,

$$n2\pi = \frac{2e}{\hbar}\Phi \tag{3.23}$$

$$\Phi = \frac{2n\pi\hbar}{2e} \tag{3.24}$$

$$\Phi = \frac{n\pi\hbar}{e}, \tag{3.25}$$

and finally by setting n = 1, we obtain the flux quantum:

$$\Phi_0 = \frac{\pi\hbar}{e} = \frac{h}{2e} = 2.07\times10^{-15}Wb \tag{3.26}$$

## 3.4 Josephson Devices

The Josephson junction is a simple yet remarkable component in superconducting electronics. It can be thought of as the transistor of the superconducting world. With this device it is possible to build sensitive magnetic field sensors as well as superconducting digital circuits with extremely efficient and fast switching times. What makes this device remarkable is that it functions on the basis of quantum tunnelling. In classical mechanics a ball cannot roll up a hill without sufficient energy being injected into the system. As the ball rolls up the hill, its kinetic energy is being converted into potential energy. The ball will slow down and, if its original kinetic energy was not high enough, the ball will stop before reaching the top and roll back down again. This hill can be thought of as a potential barrier. Similarly, potential barriers exist in quantum mechanics. A Josephson junction is made using a superconducting strip that has been interrupted by an insulator, a normal conducting metal or by a narrowing of the material. This results in a potential barrier for the electrons in the superconductor and, according to classical physics the electrons will not be able to move through this barrier. However, an electron is a quantum particle and thus exhibits wave-particle duality. Under certain conditions it appears to be a particle, and under others it behaves like a wave. In the case of the potential barriers of the Josephson junction, its wavelike nature is of importance. This wavelike nature is captured in the Schrödinger equation for a free particle:

$$\frac{d^2\psi}{dx^2} + \frac{8\pi^2 m}{h^2}[E - E_{pot}(x)]\psi = 0. \tag{3.27}$$

The probability density can be found by taking the squared modulus, $|\psi|^2$, of the function. If the potential energy in the region the particle is travelling through, $E_{pot}$, is zero, then the probability density of the wavefunction will remain constant. If the potential energy is higher than the wave energy, $E$, then the probability density of the wavefunction will decay exponentially while in this region. If the wavefunction reaches the other side of the potential barrier, it will continue with a lower constant amplitude than before. This property is called quantum tunnelling (see Figure 22) and it allows particles to have a finite probability of moving through potential barriers that would be forbidden under classical mechanics [16].

Figure 23 shows a typical Superconductor-Insulator-Superconductor (SIS) Josephson junction. Each superconductor can be described by the complex wavefunction,

$$\Psi = |\Psi|e^{i\theta}. \tag{3.28}$$

Across the junction, there is a difference between the phase of the wavefunctions. The difference in phase is a function of the supercurrent flowing through the junction and is described by,

$$I_s = I_c \sin(\phi) \tag{3.29}$$

with

$$\phi = \theta_1 - \theta_2, \tag{3.30}$$

where $I_s$ is the supercurrent, $I_c$ is the critical current of the junction, and $\phi$ is the phase difference between the wavefunctions. Thus, even though there is an electrical insulator between the two superconducting materials,

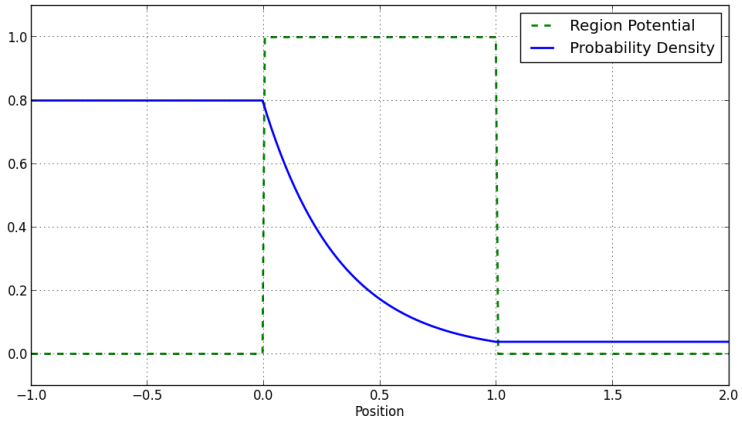


Figure 22: The probability density of a particle as well as the regional potential energy (in arbitrary units). When the particle is in a region where the potential energy is zero, the density function remains constant, while travelling through a region where the potential is greater than the energy of the particle the probability function decays exponentially until it reaches the other side of the barrier. If the barrier is small enough, there is a finite probability that the particle can move through that barrier.

there is still a supercurrent due to tunnelling electrons which links the two wavefunctions together. When the phase difference is constant, the voltage across the junction is zero. This is sometimes called the DC Josephson effect. However, if the difference in phase changes with time, a voltage is produced. This is described by the relation,

$$\frac{d\phi}{dt} = \frac{2\pi V}{\Psi_0} \tag{3.31}$$

and is known as the AC Josephson effect. Integrating (3.31) and substituting the result into (3.29) yields the alternating current

$$I_s = I_c \sin(\omega t) = I_c \sin\left(\frac{2\pi V}{\Psi_0} t\right). \tag{3.32}$$

Essentially the Josephson junction acts like a superconducting short for V=0 and like an ideal voltage controlled oscillator for V $\neq$ 0. [17]

## 3.5 DC SQUID

A Superconducting QUantum Interference Device (SQUID) can be constructed by interrupting a superconducting loop with either one or two Josephson junctions. If one junction is used an AC or RF SQUID is produced and will not be considered here. In this thesis, the DC SQUID will be considered which is constructed using two junctions in a parallel configuration as shown in Figure 24.

As before, the currents in the junctions are characterised by $i_1 = I_c \sin(\phi_1)$ and $i_2 = I_c \sin(\phi_2)$ respectively. Note that the two junctions have the same critical current. Thus the total current can be given by

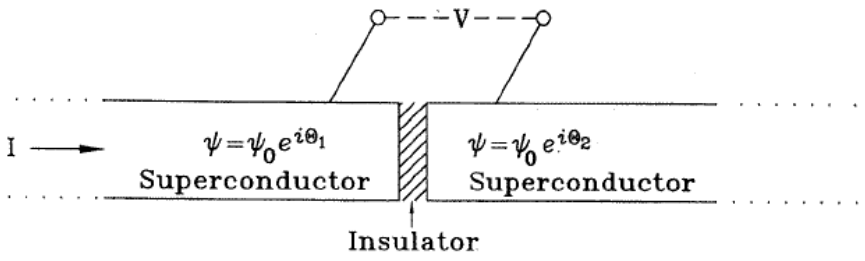


Figure 23: A superconducting strip interrupted by an insulating layer. The insulating layer forms the potential barrier required for quantum tunneling to take place. The phase of the superconducting wave becomes a function of the current flow through the junction, which leads to the unique electrical properties of the junction [18]

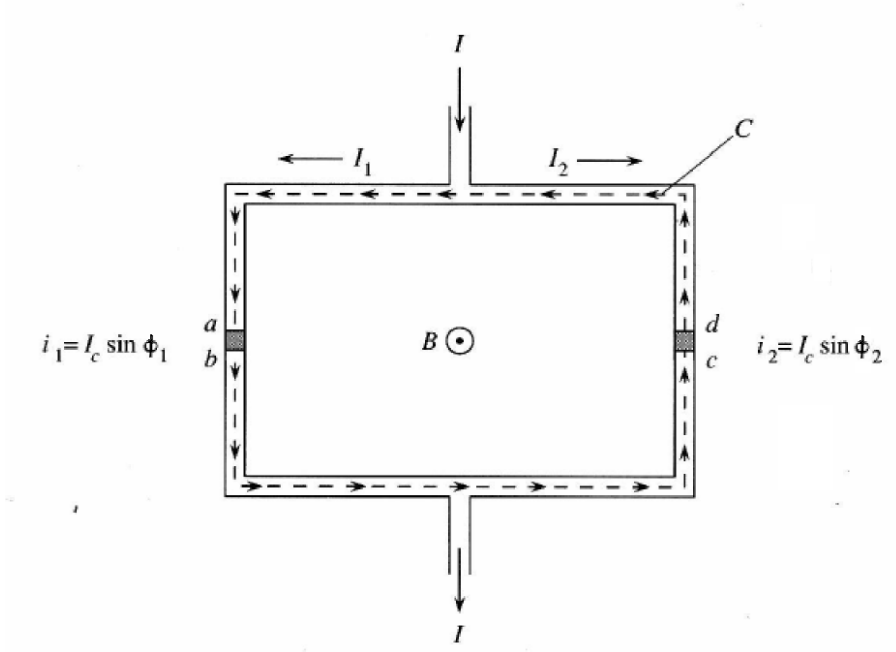


Figure 24: Two Josephson junctions in parallel in a superconducting loop forming a DC SQUID. The integration path 'C' is shown with a dotted line [14].

$$I = I_1 + I_2 = I_c \sin(\phi_1) + I_c \sin(\phi_2) \tag{3.33}$$

$$= 2I_c \cos\left(\frac{\phi_1 - \phi_2}{2}\right) \sin\left(\frac{\phi_1 + \phi_2}{2}\right). \tag{3.34}$$

The difference in the phases can be found by integrating $\nabla\theta$, the gradient of the supercurrent phases, around the closed path of the SQUID loop:

$$\oint_c \nabla\theta \cdot \mathrm{d}\mathbf{l} = 2\pi n \tag{3.35}$$

$$= (\theta_b - \theta_a) + (\theta_c - \theta_b) + (\theta_d - \theta_c) + (\theta_a - \theta_d). \tag{3.36}$$

Assuming that the superconducting wire is thicker than several penetration depths, the integration path

can be taken deep inside the superconductor where the integral involving the supercurrent is negligible. This is because the supercurrent only flows on the surface of the material. The contributions due to the other terms can be calculated from the gauge-invariant phase difference across the junctions, the derivation of which can be found in the text by Orlando [14],

$$(\theta_b - \theta_a) = -\phi_1 - \frac{2\pi}{\Phi_0}\int_a^b \mathbf{A}\cdot \mathrm{d}\mathbf{l}, \tag{3.37}$$

$$(\theta_d - \theta_c) = \phi_2 - \frac{2\pi}{\Phi_0}\int_c^d \mathbf{A}\cdot \mathrm{d}\mathbf{l}, \tag{3.38}$$

$$(\theta_c - \theta_b) = -\frac{2\pi}{\Phi_0}\int_b^c \mathbf{A}\cdot \mathrm{d}\mathbf{l}, \tag{3.39}$$

and

$$(\theta_a - \theta_d) = -\frac{2\pi}{\Phi_0}\int_d^a \mathbf{A}\cdot \mathrm{d}\mathbf{l}. \tag{3.40}$$

Substituting equations 3.37 - 3.40 into (3.36) yields the required difference in the phase. The integral of the magnetic vector potential, $\mathbf{A}$, around the closed loop is equal to the total flux inside the loop.

$$\phi_2 - \phi_1 = 2\pi n + \frac{2\pi}{\Phi_0}\oint_c \mathbf{A}\cdot \mathrm{d}\mathbf{l} \tag{3.41}$$

$$\phi_2 - \phi_1 = 2\pi n + \frac{2\pi\Phi}{\Phi_0}, \tag{3.42}$$

where $n$ is an integer, $\Phi$ is the external flux, and $\Phi_0$ is the flux quantum. Substituting (3.42) into (3.33) and simplifying yields the total current in the superconducting loop

$$I = 2I_c\cos\left(\frac{\pi\Phi}{\Phi_0}\right)\sin\left(\phi_1 + \frac{\pi\Phi}{\Phi_0}\right). \tag{3.43}$$

It is of interest to know what the maximum current is that we can bias the SQUID with before it loses its superconducting qualities. If we further assume that the magnetic flux produced by the superconducting loop is significantly smaller than the external flux, then the maximum bias current can be found from (3.43). At a given external flux, $\Phi$, the current $I_{max}$ is found by maximizing (3.43) with respect to $\phi_1$ as follows:

$$\frac{\mathrm{d}I}{\mathrm{d}\phi_1} = 2I_c\cos\left(\frac{\pi\Phi}{\Phi_0}\right)\cos\left(\phi_1 + \frac{\pi\Phi}{\Phi_0}\right) = 0 \tag{3.44}$$

$$\therefore \cos\left(\phi_1 + \frac{\pi\Phi}{\Phi_0}\right) = 0. \tag{3.45}$$

Thus, at the maximum current values

$$\sin\left(\phi_1 + \frac{\pi\Phi}{\Phi_0}\right) = \pm 1, \tag{3.46}$$

and the maximum current can then be found by taking the absolute value of (3.43) at these values for $\phi_1$. This yields an approximation to the maximum current in the SQUID ring

$$I_{max} \approx 2I_c \left| \cos\left(\frac{\pi\Phi}{\Phi_0}\right) \right|. \tag{3.47}$$

This function describes the maximum current that can flow in the SQUID, as a function of the external flux, while still remaining in the superconducting state. A simplified SQUID electrical diagram is shown in Figure 25. Note that each Josephson junction is manufactured with a small resistor in parallel, to eliminate hysteresis in the V-I curve of the junction.

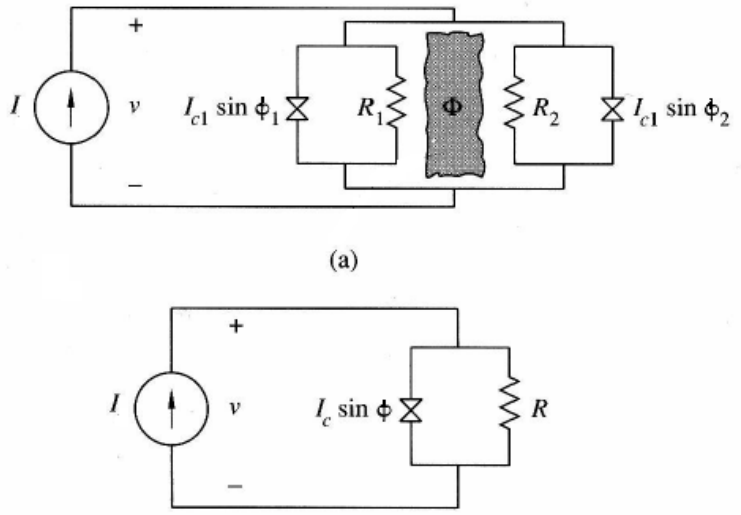


Figure 25: (a) Two generalised Jospehson junctions that have been damped with parallel resistors. The grey area represents the flux passing through the superconducting ring. (b) An equivalent circuit when the self-inductance of the loop is negligible [14].

It can also be shown that the two junctions can be simplified and redrawn as a single equivalent junction and resistor pair as shown. If the biasing DC current is greater than $I_c$ at zero applied flux, then a voltage will develop across the junction. The voltage will have a DC component, $\langle v \rangle$, given by

$$\langle v(t) \rangle = IR\sqrt{1 - \left(\frac{I_{max}}{I}\right)^2} \qquad \text{for } I > I_c. \tag{3.48}$$

Thus, substituting in (3.47), the relationship between the applied flux and the developed voltage can be found using,

$$\langle v(t) \rangle = IR\sqrt{1 - \left[\frac{2I_c}{I}\cos\left(\frac{\pi\Phi_{ext}}{\Phi_0}\right)\right]^2}. \tag{3.49}$$

This voltage can be measured using conventional electronics to determine the flux density threading the superconducting loop. Equation 3.49 has a period of $\Phi_0$ [14], thus one method of determining the change in flux is by counting the number of cycles of the voltage output. This is not the best method of determining the flux however, and a more sensitive technique called a flux lock loop is described in the next section.

## 3.6 Flux Lock Loop Operation of DC SQUID

In the previous section it was shown that the DC SQUID can be used as a non-linear magnetic flux-to-voltage transducer. In order to linearise the output of the SQUID and to achieve maximum sensitivity, the sensor is placed inside a Flux Lock Loop (FLL) configuration. A schematic representation of the system is shown in Figure 26. In this configuration, the flux is not detected directly by the SQUID loop itself. Instead an external pick-up coil, $L_p$, is inductively coupled with the SQUID loop, $L$. This maximizes the sensitivity of the SQUID since the pick-up coil can be made much larger than the SQUID loop. A constant bias current, $I_B$, is driven into the SQUID loop and is large enough to force the Josephson junctions out of the superconducting state. A voltage will then develop across the junctions that is a periodic function of the flux through the SQUID loop as shown previously. The voltage across the SQUID forces current to flow through a parallel inductor that has been inductively coupled to an external amplifier.

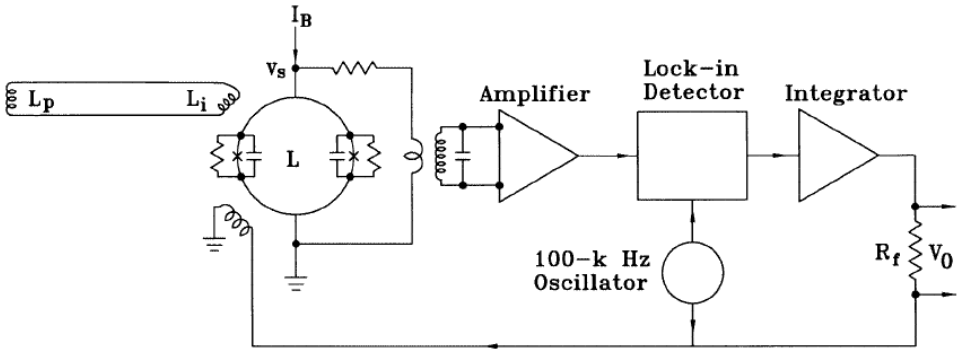


Figure 26: Schematic of the pick-up coil, input coil, SQUID and flux-locked loop. A change in magnetic field at the pick-up coil, with inductance $L_P$ , induces a change in field at the input coil, with inductance $L_i$ . The SQUID is inductively coupled to the input coil and detects a change in magnetic flux. The voltage response of the SQUID $V_S$ is the input to the flux-locked loop, which uses a modulating flux scheme, explained in the text, to maintain the SQUID at a peak on the V-$\Phi$ curve. The user measures a change in $V_O$, which is proportional to the feedback from the loop and hence to the change in magnetic field at the pick-up coil. [18].

A small coil is inductively coupled to the SQUID and connected to an external oscillator. The oscillator has a fixed frequency, usually above 100 kHz, and a constant amplitude corresponding to $\frac{\Phi_0}{2}$, while the DC current through the coil is variable. If the phase of the SQUID is at a maximum of the transfer function, then the flux generated by the oscillator will result in an output voltage with twice the frequency of the oscillator as seen in figures 27 and 28. This position in the transfer function is the working point of the SQUID and the FLL will always attempt to keep the SQUID here by adjusting the DC current through the oscillator coil. The spectrum shows no component at the oscillator frequency and hence no adjustment needs to be made by the FLL [18].

If the flux through the SQUID were to change, then the position in the transfer function would shift and distort the output signal. When this occurs, harmonics at the same frequency as the oscillator will appear on the output signal, as seen in figures 29 and 30. The lock-in detector uses this and adjusts the DC current value of the oscillator to compensate for the change and move the SQUID phase back to the maximum value.

The amplitude and phase at the oscillator frequency is considered an error signal, and by integrating the

error signal the output of the SQUID can be linearised and a large dynamic range is possible. A standard data acquisition system is used to read the output voltage, $V_0$, which is proportional to the change in magnetic flux through the SQUID since it was switched on. Note, that the SQUID is not capable of reading the absolute magnetic field magnitude, it can only detect the change from its initial start-up value, however only the alternating magnetic flux is usually of interest.

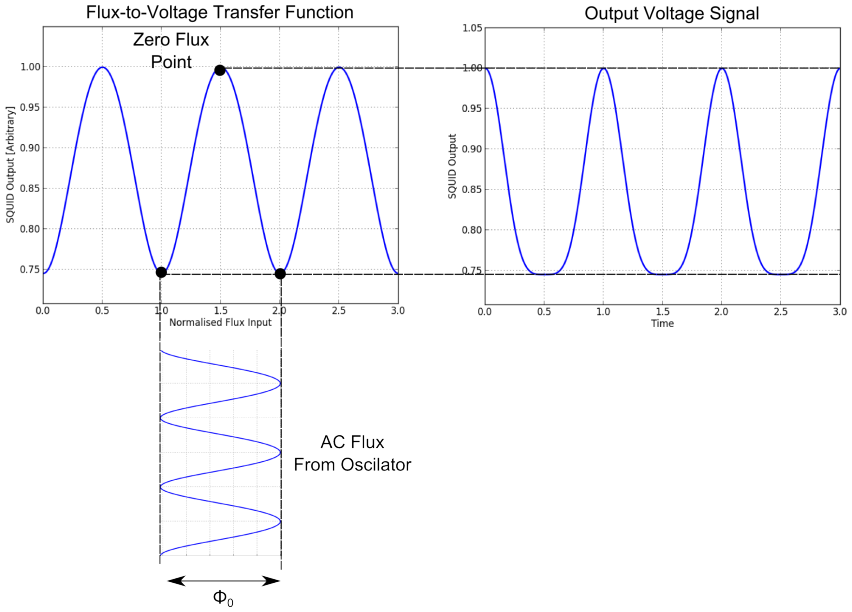


Figure 27: The transfer function of the SQUID in FLL mode. The FLL ensures that the DC working point remains at the maximum of the transfer function.

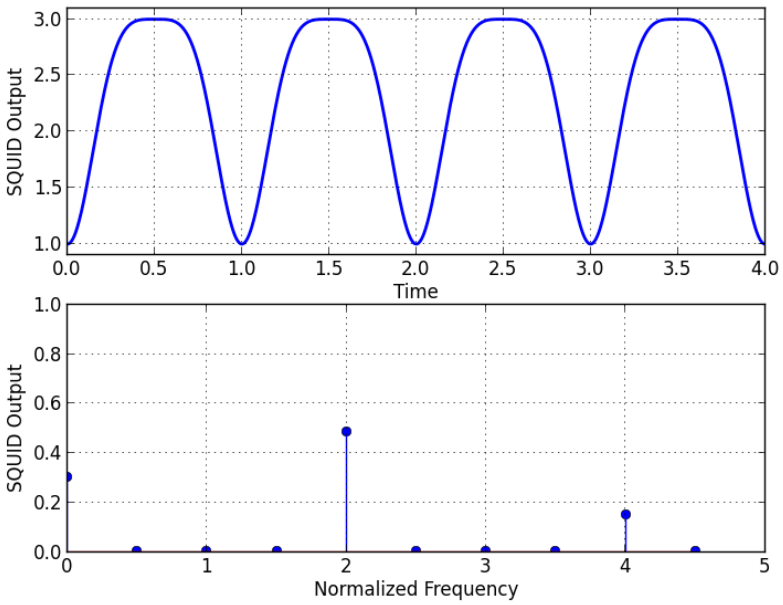


Figure 28: Graph showing the time signal and frequency spectrum of the SQUID output when locked-in to transfer function maximum.

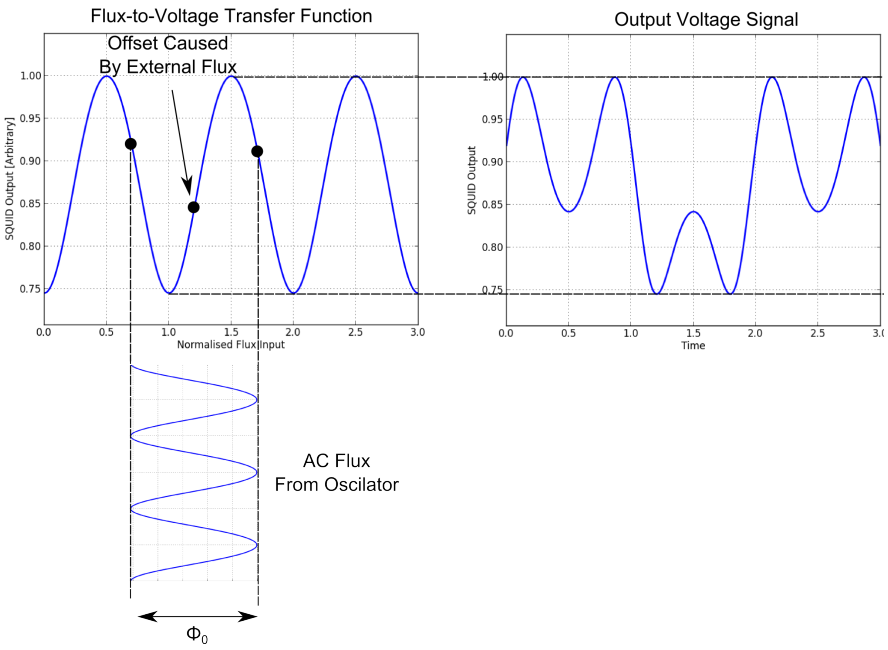


Figure 29: The transfer function of the SQUID in FLL mode. The external flux causes the working point to shift, causing distortions in the output signal which can be detected.

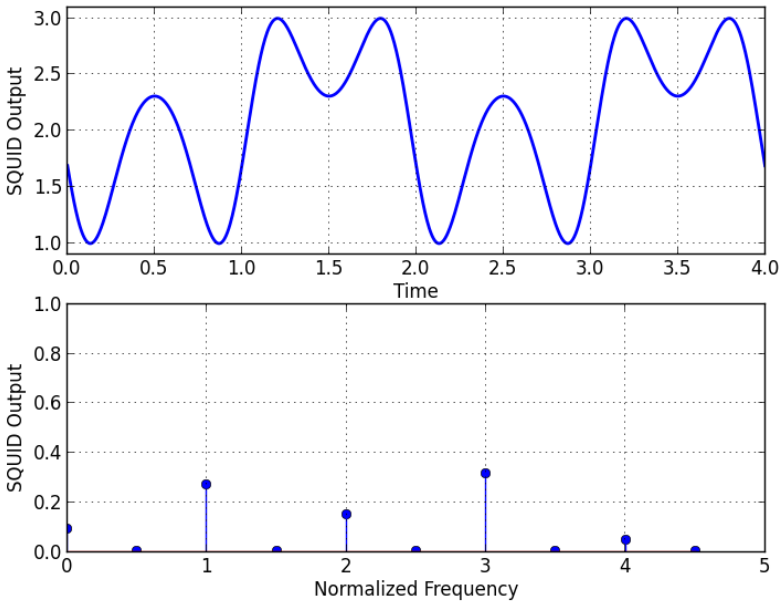


Figure 30: Graph showing the time signal and frequency spectrum of the SQUID output when the phase is shifted by 0.2 $\Phi_0$. Notice the increase in the amplitude at the oscillator frequency.

## 3.7 SQUID Tuning Using The FFT

The SANSA SQUID requires the user to tune several parameters on the FLL via a computer interface before proper operation can begin. During the tuning process, a 100 Hz test signal as well as a 128 kHz biasing field is applied to the SQUID. The purpose of the tuning is to ensure that the 128 kHz signal is as small as possible,

and that the output from the test signal is the "WM" shape similar to Figure 29. It should be noted that the SANSA SQUID's working point is not around the maximum of the transfer function, but rather where the slope is maximum. Regardless, the principle remains the same.

By continuously performing an FFT on the output signal, the user can monitor these frequencies directly, as oppose to monitoring the time varying signal which can be difficult to use. The parameters can then easily be tuned to ensure that the 128 kHz biasing signal is a minimum, the 100 Hz test signal is a maximum, and that only even or odd harmonics (depending on the SQUID) appear on the output signal. Once this is done, the tuning is complete.

# 4 Traditional Magnetometers

In order to fully understand the advantages that the SQUID magnetometer has to offer, it is beneficial to consider the properties of the current sensor technology available. This section aims to provide an overview of the typical sensors that are used to measure magnetic signals and their typical performance characteristics. While it is difficult to provide a complete list of performance characteristics, it is hoped that by analysing several systems that exist it is possible to get a general sense of what is typical with the various sensors. Table 3 shows the results of this investigation.

| **Device** | **Example System** | **Bandwidth** | **Noise** | **Sampling Resolution** | **Sensor Gain** |
|---|---|---|---|---|---|
| Induction Coils | Svalbard | 2.5 Hz | 10 pT/$\sqrt{\text{Hz}}$ @ 1 Hz (16 pT rms) | 1 pT.Hz | 150 $\mu$V/(nT.Hz) |
| Proton Precession | GEM Systems GSM-19T | 2 Hz | 150 pT/$\sqrt{\text{Hz}}$ @ 1 Hz (210 pT rms) | 10 pT | |
| Overhauser | GEM Systems GSM-19 | 10 Hz | 15 pT/$\sqrt{\text{Hz}}$ @ 1 Hz (47 pT rms) | 10 pT | |
| Optically Pumped | GEM Systems GSMP-35 | 20 Hz | 0.3 pT/$\sqrt{\text{Hz}}$ @ 1 Hz (1.3 pT rms) | 0.1 pT | |
| Fluxgate | Bartington Mag-03 | 1000 Hz | 0.6 pT/$\sqrt{\text{Hz}}$ @ 1 Hz (19 pT rms) | 8 pT | 143 $\mu$V/nT |
| SANSA HTS SQUID | Star Cyrogenics | 125 Hz (filtered) | 0.084 pT/$\sqrt{\text{Hz}}$ @ 10 Hz (0.94 pT rms, rated) | 0.6 pT | 0.53 V/nT |
| LTS SQUID | LSBB | 125 Hz (filtered) | 0.002 pT/$\sqrt{\text{Hz}}$ (0.022 pT rms) | 0.0015 fT to 0.15 fT | 0.06 to 6 V/nT |

Table 3: The table shows a comparison between various magnetometers from actual devices produced by leading manufacturers or systems that have been deployed for geomagnetic measurements. Notice how the SQUID magnetometers outperform all other sensors.

## 4.1 Induction Coils

Induction coils, also known as search coils, work use Faraday's law as their main operating principle:

$$V = -N\frac{d\Phi}{dt}. \tag{4.1}$$

As the rate of change of magnetic flux through the coils is increased, so is the induced voltage where N is the number of windings of the coil. Thus, this system cannot detect a DC field and the sensitivity will increase with frequency. A system for measuring geomagnetic pulsations has been deployed in Svalbard [19].

The system comprises of six stations each with two 160,000 turn coils of number 36 copper wire mounted on 0.8 m long by 2.5 cm diameter annealed mu-metal cores. The coil gain is 150 uV/(nT Hz) and the signal from the coils is further amplified until the the system response is 4.43 V/(nT Hz). The frequency response is DC  2.5 Hz (-3 dB corner frequency) with a resolution of approximately 10 pT at a specified frequency [19].

While the operating principles of the device are comparatively simple and the sensors are also fairly easy to construct, the performance is significantly less than what can be achieved using a SQUID magnetometer for the detection of ULF waves.

## 4.2 Proton Precession Magnetometer

The Proton Precession Magnetometer (PPM) is based in the principle that the magnetic moment of a proton acts like a tiny bar magnet. When exposed to a strong magnetic field, the magnetic moment of the protons will align to the excitation field. When the external field is released, the protons will realign to the ambient

field, and in the process of doing so will behave like small gyroscopes and precess around the ambient field. The precession frequency is proportional to the ambient field, and thus by measuring the precession frequency, the ambient field strength can be determined [20]. This device is ideal when the orientation of the sensor is difficult to guarantee and the signals of interest are relatively large, such as during magnetic site surveys.

Typically the device consists of a container filled with a fluid that has a high concentration of protons (water and kerosene are common). A coil is then wrapped around this container. These coils are responsible for generating the external field that aligns the magnetic moments of the protons, as well as detecting the precession frequency of the excited protons. To take a measurement, the coils are thus energized and remain on while the protons align. After a period of time this external field is released and the protons are allowed to precess. These oscillations quickly decay due to interactions with other particles, but while the precession occurs it produces a small alternating current in the excitation coil. The small signal is amplified and presented to a phase comparator. The output of the comparator is fed into a Voltage Controlled Oscillator (VCO) running at around 64 times greater than the input frequency. The output frequency of the VCO is reduced by 64 and fed back to the phase comparator. As long as the input frequencies of the phase comparator are different, the output voltage will change, hence changing the frequency produced by the VCO until the VCO has locked on to the precession frequency. Once the VCO has locked on to the precession frequency, a counter is started for a fixed period of time, effectively measuring the precession frequency. Through calibration the output of the counter can be related to the measured field strength [4]. A schematic of a proton precession magnetometer circuitry can be found in Figure 31.

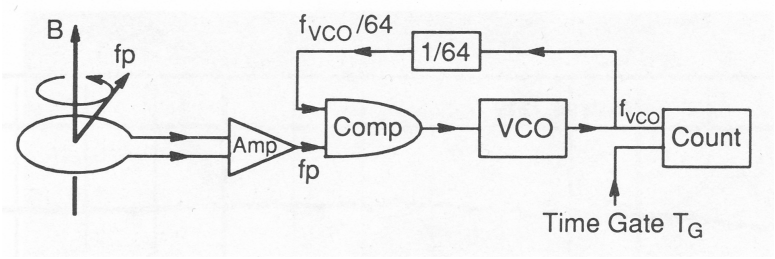


Figure 31: Schematic illustration showing how absolute measurements of the total magnetic field are made using the principle of proton precession [4].

A PPM uses a fundamental property of matter to obtain absolute magnetic field measurements. While it is not able to directly measure the vector components it does provide unbiased measurements. One of the shortcomings of the PPM is that the sampling rate is normally quite low, typically about 2 Hz, which makes it impractical to measure higher frequency geomagnetic signals such as Schumann Resonances. The typical resolution for commercial systems is in the order of 0.1 nT and have a typical noise level of 0.1 nT RMS @ 1 Hz [21].

Overhauser magnetometers use a similar mechanism to PPM systems in that they rely on the precession of hydrogen atoms in the external field, however they tend to be more sensitive with a higher sampling rate. These magnetometers have reported sensitivity levels in the order of 10 $\text{pT}/\sqrt{\text{Hz}}$ with a typical sampling rate of 10 Hz [22].

## 4.3 Optically Pumped Magnetometer

The Optically Pumped Magnetometer (OPM) is based on the Zeeman effect. To understand how these sensors work, a brief description of energy quantisation is required. An electron orbiting a nucleus is in a bound state. When quantum particles, such as electrons, are in a bound state, it implies that their energy levels are also fixed at certain discrete values. As an analogy, consider a string with length $L$ fixed at both ends. Because the ends are fixed, they cannot move and only an integer number of half-wavelengths can set up a standing wave on the string according to:

$$L = \frac{n\lambda}{2}, \text{ for } n = 1, 2, 3, ... \tag{4.2}$$

The number $n$ can be considered a *quantum number*, since it only allows discrete values for the number of half-wavelength on the string. An electron can also be described by a wavefunction and, since it is locked into a fixed orbit around the nucleus, only certain discrete energy levels will be allowed. The lowest of these energy levels is called the *ground state* and the higher energy levels are called *excited states*. An electron can move from the ground state to an excited state by absorbing a photon, if that photon's energy is equal to the difference in energy of the two states. The excited states are however unstable, and the electron will move back to the ground state, after a random time interval, by emitting a photon with energy equal to the difference in energy levels between the two states [16].

A second concept is required before the OPM functionality can be described, the quantum concept of *spin*. Spin is an inherent property of atomic particles and characterised by the particle having an intrinsic angular momentum. For Fermions, such as electrons, protons and neutrons, the spin value is 1/2 and can either point "up" or "down". Spin gives rise to a small magnetic dipole moment inherent to the particles. If the particles are exposed to an external magnetic field, the spin dipole moment will align to the external magnetic field. To do this a torque must be generated and act on the electrons to change their orientations. By changing the orientation, the magnetic field is performing work on the electron and hence transferring energy to it, changing its energy level. If the two dipole moments are orientated in different directions, "up" and "down", a different amount of work will be required to change its orientation and hence a different amount of energy will be transferred. This splitting in the energy levels of the electron is known as the Zeeman effect, as illustrated in Figure 32.

To turn this effect into a functional magnetometer we require the following apparatus. Two glass cells containing a metallic vapour (e.g. Rubidium) and a light sensor are placed in line. The first cell is heated, causing it to emit light at a very specific energy level. The light is then passed through a circular polarising filter before it shines into the second cell. The combination of the heated light source and the filter ensures that the only one transition is possible, between energy levels 2 and 3. Energy level 3 is unstable and will decay randomly back down to energy levels 1 and 2. However, once the electron is in energy level 1, there is no way for it to move to a higher energy level and it remains there. Initially some of the photons are absorbed by the alkali vapour and hence the light intensity on the sensor is reduced. As more and more electrons get trapped in energy state 1, more light is allowed to pass and the light intensity on the sensor increases [22, 4].

The gap in energy between energy levels 1 and 2 are due to the Zeeman effect, and the greater the external

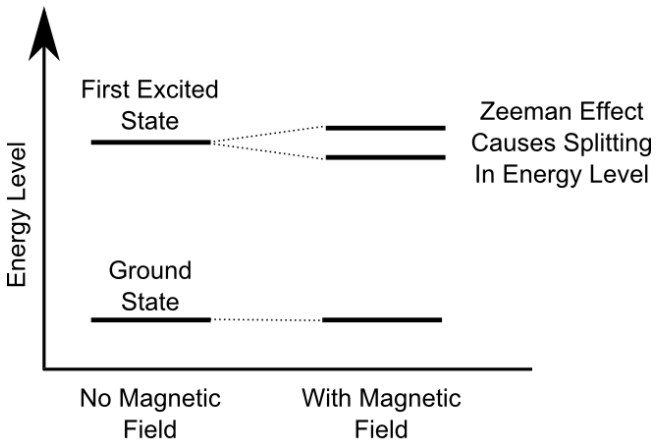


Figure 32: As a bound electron is exposed to a magnetic field, the energy level of certain orbitals will split into multiple smaller levels due to the interaction between the spin dipole moment of the electron and the external field.

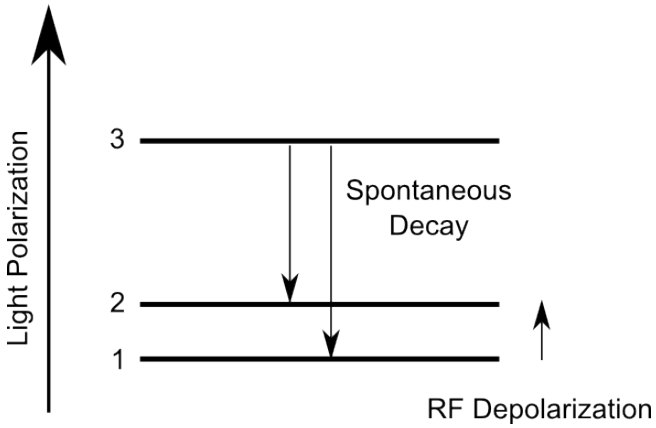


Figure 33: Incident light raises the energy level from energy state 2 to 3. From here it decays randomly to energy state 1 and 2. Eventually all the electrons will be in energy state 1 changing the optical properties of the vapour which can be detected. An RF signal is used to "reset" the energy levels of the vapour and the process can start again. The frequency of the RF signal is determined by the external magnetic field [22].

magnetic field the larger this energy gap becomes. A coil is wrapped around the second cell and by passing an RF signal through the coils, the frequency of which corresponds to the energy difference between states 1 and 2, the system can be reset. This process is called RF depolarisation (see Figure 33). The frequency of the RF field required to repopulate energy 2 varies with the ambient magnetic field and is called Larmor frequency. The polarization and depolarization of the alkali vapour causes the light intensity to become modulated by the RF frequency. By detecting the light modulation and measuring the frequency, the value of the magnetic field can be obtained [22, 4].

The OPM is an has a sensitivity comparable to the SQUID magnetometer in the order of 327 $\mathrm{fT}/\sqrt{\mathrm{Hz}}$ over a bandwidth of 26 Hz. However, in the presence of environmental noise, this sensitivity drops to 130 $\mathrm{pT}/\sqrt{\mathrm{Hz}}$ [23]. They also have the advantage of not requiring cryogenic cooling like SQUID magnetometers. However, compared to SQUID magnetometers the bandwidth of the OPM is relatively low, in the order of 10's of Hz [23]

and dependent on temperature. This is still sufficient to monitor low frequency geomagnetic signals, but would be unable to measure higher order Schumann resonances. The OPM is also a scalar instrument which places it at a disadvantage over the SQUID which is a vector magnetometer. However, given the sensitivity, this device may still be a viable alternative to the SQUID in locations where cryogenic cooling is impractical.

## 4.4 Fluxgate Magnetometer

The fluxgate sensor uses the hysteresis properties of iron as its operating principle. When iron is exposed to a magnetic field, the material itself becomes magnetised. However, the amount by which the material becomes magnetised with external field is non-linear and also has hysteresis.

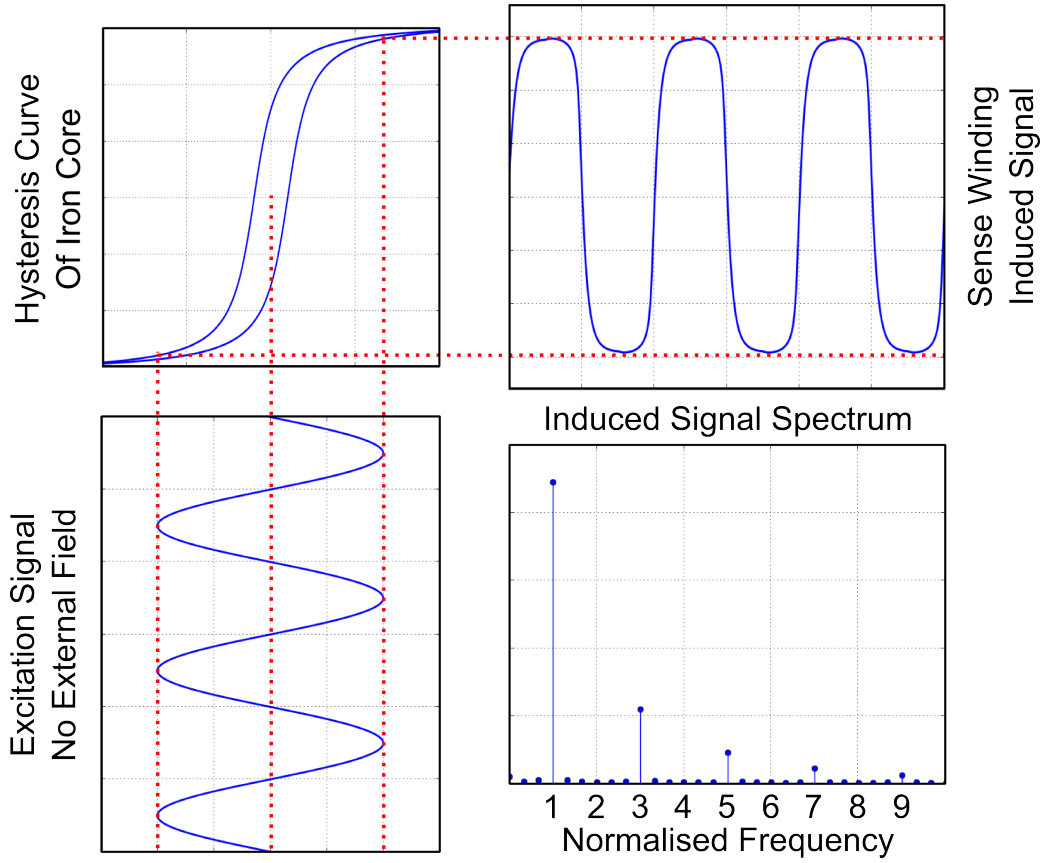


Figure 34: The transfer function and resulting spectrum of a fluxgate's output with no external magnetic field. As the excitation signal passes through the iron core, the hysteresis response curve of the core deforms the induced voltage on the sense winding and only produces odd harmonics.

By winding a coil around an iron core and driving a current with a fixed frequency through it, the core will follow this hysteresis curve. This winding is called the drive winding. If the field generated by the excitation coil is large enough the core will be driven into saturation, this leads to the flux inside the core to become distorted. A second winding is wrapped around the core to detect the distorted excitation signal, this is called the sense winding. If no external magnetic field is present, then the BH-curve will be traversed symmetrically which results in only odd harmonics of the drive frequency appearing on the sense winding (Figure 34). If an external field is present, the output reaches saturation in one half-cycle sooner than on the other half-cycle. The

result is that even harmonics of the drive frequency now appear on the output (Figure 35). The amplitude and phase of the even harmonics are proportional to the magnitude of the external flux around the core axis [4].

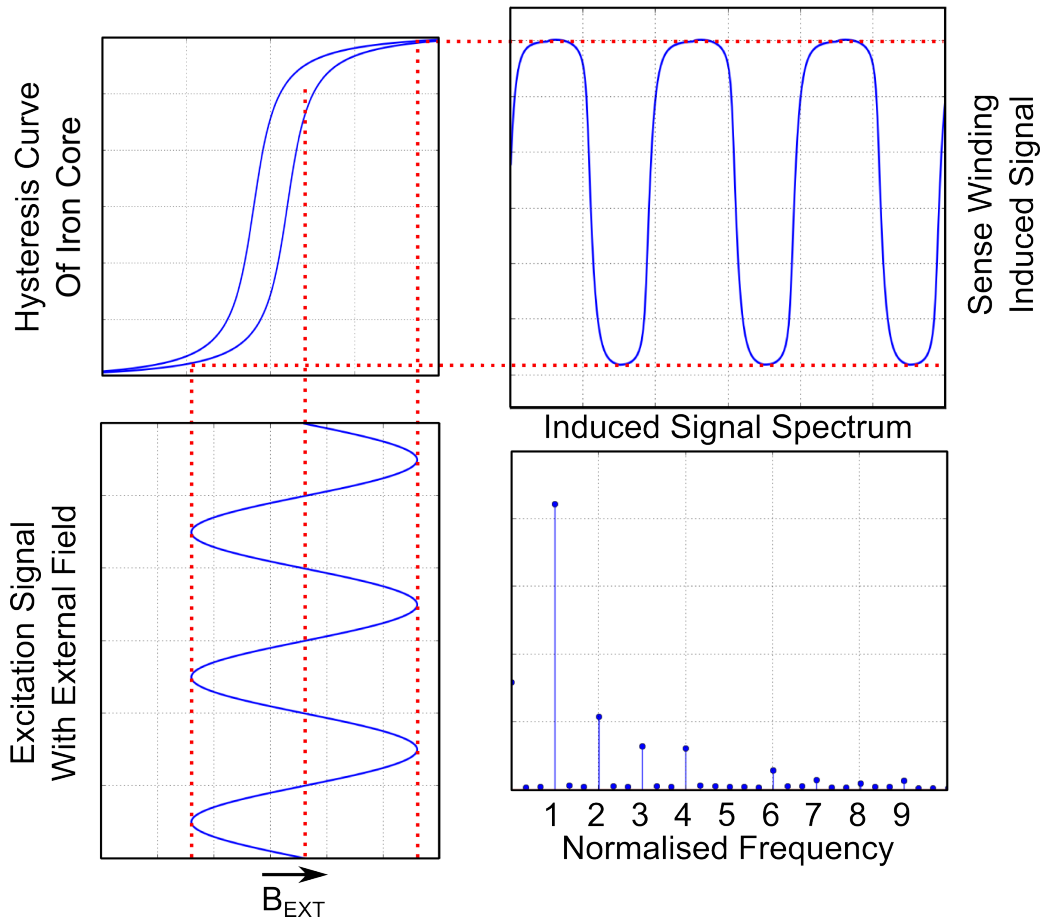


Figure 35: The transfer function and resulting spectrum of a fluxgate's output with an external magnetic field. As the excitation signal passes through the iron core, the hysteresis response curve of the core deforms the induced voltage on the sense winding. However, the external field causes the core to reach saturation in one half cycle before the other. The result is the appearance of even harmonics in the output signal.

Electronics can now be used to extract the relatively weak even harmonics and amplify them. A fluxgate magnetometer is not an absolute magnetometer like the PPM, and hence it must be calibrated against a set of standards. To conform to observatory standards, the calibration procedure is involved and difficult and includes sensor offset, sensitivity, temperature coefficients, and alignment angles. Despite these difficulties, they are still widely used as they offer a comparatively wide bandwidth and good noise characteristics. Fluxgate magnetometers have much better frequency characteristics than PPM and OPM, because of continuous reading as oppose to discrete sampling. Because of this they are also less susceptible to being overloaded by a strong noise signal, like from the 50/60 Hz power grid [20].

Fluxgates have several implementations that are used which trade-off various performance characteristics. The lowest noise topologies appear to be the Ring Core or Racetrack configurations, each with a noise level of approximately 15 pT rms over an unknown frequency range [24]. Futhermore, Mattia Butta has done work on reducing the sensor noise in orthogonal fluxgates. They report a reduction of the noise floor 2.5 pT/Hz and 7

pT/Hz noise at 1 Hz [25]. The Bartington Mag-03 fluxgate is rated as a low noise instrument and reports a noise level of 6 pT/Hz at 1 Hz [26] with an output gain of approximately 0.11 V/$\mu$T.

# 5 SQUID Observatory

Site selection is a complex procedure that involves many factors that need to be taken into account. Some of these factors are easy to balance while others require intuition based on incomplete data. The main reason for moving the SQUID to a remote location is to get it as far away from man-made magnetic signals as possible, in order to maximise the benefit of the sensor. However, placing the SQUID in a location that is too remote and difficult to access is also not advisable as it is likely to lead to poor maintenance and consequently unreliable data. Arguably, the decision of where to build the remote station is one of the most important choices that need to be made. Based on the recommendations from the International Association of Geomagnetism and Aeronomy (IAGA) [27], INTERMAGNET [28], and a chapter by Trnkoczy [29] on setting up a remote seismic station, the author will attempt to summarise the main points that need to be taken into account when selecting a potential site for the SQUID magnetometer, as well as present guidelines for the construction of the SQUID hut and observatory layout.

## 5.1 Station Layout and Design Summary

Before the discussion on where to place the remote station, it is beneficial to discuss the design and requirements of the station itself. Once the requirements for the station are understood, a more meaningful choice of location can be made. We start the discussion by looking at the layout of a traditional magnetic observatory as shown in Figure 36.

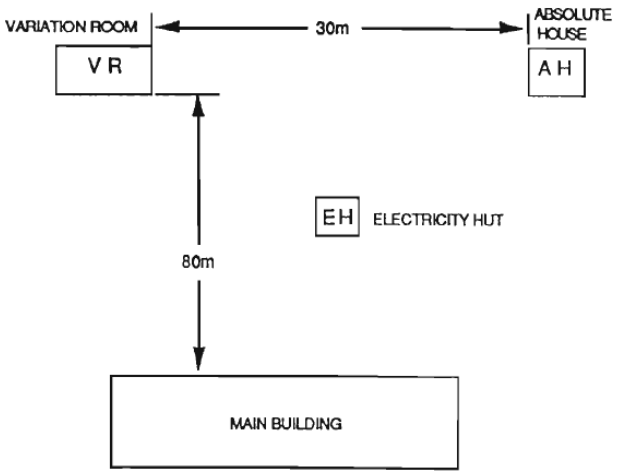


Figure 36: Layout of a magnetic observatory with small buildings. The distances between the houses are typically minimal, but can vary, depending on the instruments in use [27].

A traditional magnetic observatory consists of four structures. The main building holds all the computers and equipments needed for the staff to make use of the observatory data and maintain the site. In permanently manned stations, this building may have accommodation for the staff.

The second building is the electricity hut. This structure contains a battery bank that provides uninterrupted power to the critical systems of the observatory. It also has a means of recharging the batteries, either through a connection to the national power grid or through a secondary means such as solar panels. It is not strictly

required to house this in a separate building, as these functions could be included in the main building. The reason for having a separate building is attempt to limit the amount of electrical noise that couples onto the cables that lead to the variometers and the absolute hut due to human activity in the main building. Figure 37 shows how the IAGA recommends the wiring of the observatory should be done [27]. The 'Y' layout is to attempt to make the cables as short as possible and keep the loop area of the cables as small as possible to limit inductivly coupled noise signals.

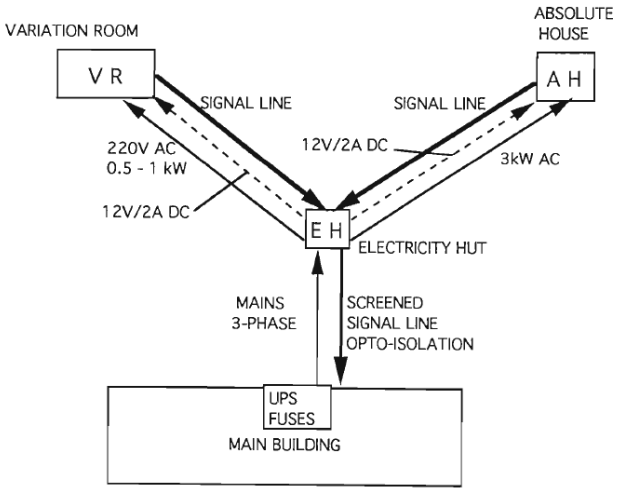


Figure 37: A possible wiring diagram for a magnetic observatory. All cables should be buried in the ground to reduce the risk of lightning damage. These cables should also be marked and shielded. The signal cables should have optical isolation at both ends and, if possible, fibre optics should be used instead of metallic signal cables [27].

The absolute hut houses a series of instruments designed to measure magnetic declination and inclination, as well as the long term magnetic field strength. The procedure for measuring these values is very strict, clearly defined, and have to be taken manually by an operator, typically a few times a week, due to the lack of quality automatic instruments. The INTERMAGNET manual recommends using a proton precession magnetometer for the field magnitude, and a fluxgate mounted on a theodolite to measure the inclination and declination [28]. Through careful measurements, using these instruments, a baseline for the observatory can be defined over time.

The variometer hut holds magnetic sensors that measure the short term variation in the local magnetic field. INTERMAGNET states that their sampling rate needs to be at least 1 Hz for vector magnetometers and a period of 30 seconds for scalar magnetometers [28]. The measurements from the variometer hut are not typically compared to the measurements from the absolute hut, since the data of interest is the short term variation in magnetic field rather than the baseline of the area [10]. According to INTERMAGNET however, all variometer data must include the best available baseline reference available [28]. This requirement may have to be relaxed for a remote SQUID site in favour of a cleaner magnetic signal that can possibly be obtained from a more remote unmanned site.

Figure 38 shows a schematic diagram of a proposed SQUID observatory based on the recommendations of the IAGA for a traditional observatory [27]. As can be seen, the basic structure remains the same. It was chosen not to include an absolute house as this is not strictly needed to observe the short term signals that

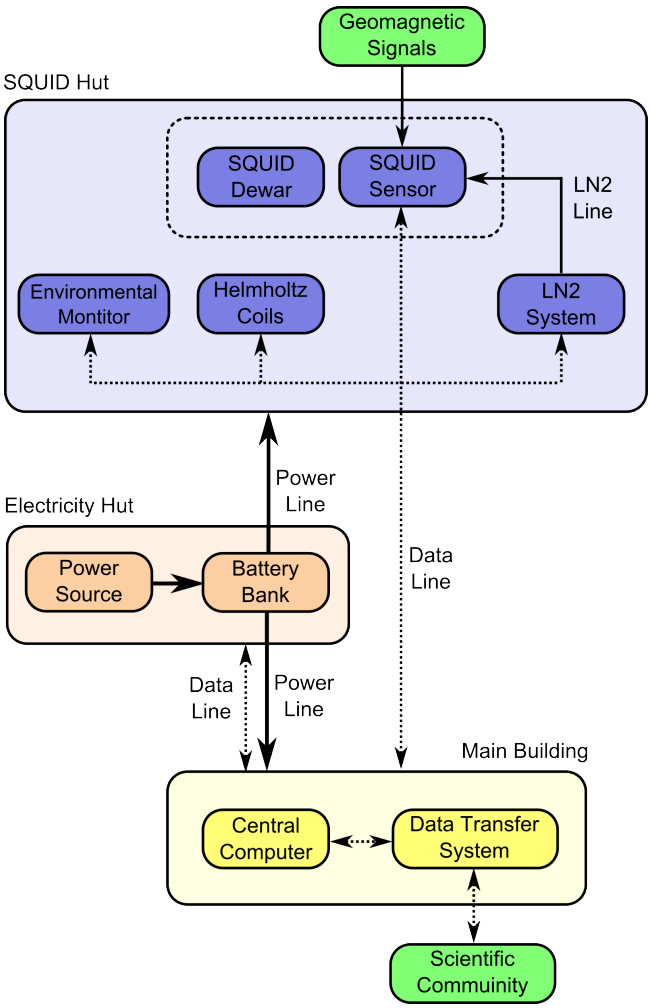


Figure 38: A schematic representation of the SQUID observatory buildings, their functions and how they are connected.

the SQUID would be suitable to detect. Furthermore, the SQUID station would most likely be unmanned and hence including these manual instruments would be meaningless.

One of the distinct differences between a traditional magnetic observatory and a SQUID observatory is the fact that the latter requires cryogenic cooling. As mentioned in a previous section, there are two main types of superconductors, namely High Temperature (HTC) and Low Temperature (LTC) superconductors. SQUID magnetometers are cooled using immersion cooling, which essentially means that the SQUIDs are placed in a suitable cryogenic liquid, in most cases either liquid nitrogen or liquid helium. This technique is favoured over using a cryocooler due to the magnetic and vibrational noise that they generate. The cost and availability of liquid helium makes its use impractical in many cases, and hence the majority of observatories would be forced to use liquid nitrogen and consequently a HTC SQUID. As heat leaks into the SQUID dewar, the liquid nitrogen will slowly boil off and will need to be replenished periodically. This will be discussed in greater detail in Section 7.

The SQUID hut also contains an environmental monitor, which should at the very least include a temperature sensor. As the temperature inside the SQUID hut changes, the support structures of the SQUID will deform

slightly due to thermal expansion. This expansion may be enough to cause a disturbance on the SQUID output and hence should be monitored. To understand the nature of this problem a brief example is used to illustrate. The rated sensitivity, $\sigma$, of the SANSA SQUID is 1.9 nT/V, assuming there is no noise and that the sensor is exposed to a modest flux of 30 $\mu$T. If it is assumed that the SQUID's maximum output voltage is $\pm$10 V and it is sampled by an 18-bit analogue-to-digital converter. Thus, the magnetic flux that corresponds to the least significant bit on the digital output is approximately,

$$\frac{\sigma \Delta V}{2^b} = \frac{(1.9 \times 10^{-9})(20)}{2^1 8} \approx 145 fT. \tag{5.1}$$

As the sensor is rotated, the change in magnetic flux that the sensor is exposed to can be described by,

$$\delta B = B_0(1 - \cos(\theta)), \tag{5.2}$$

assuming a perfectly uniform field. To produce a change of 145 fT, according to these assumptions the minimum rotation angle can be calculated as,

$$\theta = \cos^{-1}\left(1 - \frac{\delta B}{B_0}\right) = \cos^{-1}\left(1 - \frac{145 \times 10^{-15}}{30 \times 10^{-6}}\right) \approx 0.006^\circ. \tag{5.3}$$

The SQUID would only need to rotate by approximately 6 millidegrees, or 22 arcseconds. Thus, even minute changes in the orientation of the SQUID could result in changes in the output. As suggested by the IAGA [27], it may also be advisable to place tilt sensors on the SQUID support structures to directly measure the deformation, but these changes are typically very small and difficult to measure. It was found that any signals transmitted between the SQUID hut and the control room should be as an analogue voltage signal, as oppose to a serial signal such as RS-232. Serial transmissions from an environmental monitor, placed in the SQUID hut, were clearly visible on the output of the SQUID and the instrument had to be removed and redesigned to correct this.

Figure 38 shows a Helmholtz coil system placed inside the SQUID hut. This system is composed of three orthogonal Helmholtz coil pairs that surround the SQUID sensor. These coils serve two purposes, firstly they are there to cancel out the Earth's magnetic field during the cooling of the SQUID. By cooling the SQUID in a low magnetic field, theory tells us that the number of Abrikosov vortices (see Section 3.2) that form in the HTC superconductor can be reduced. The coils can then be switched off slowly and exposed to the Earth's unattenuated magnetic field. Their second function is to aid in orientating of the SQUID to True North. Both of these aspects are discussed in more detail in Section 8.2 and 8.3 respectively.

One other key difference between a SQUID station and a traditional observatory is the sampling rate. As mentioned earlier, an INTERMAGNET observatory is expected to sample its vector magnetometers at a rate of 1 Hz [28]. The SQUID, however, is typically sampled at 125 Hz to be able to detect higher frequency geomagnetic disturbances such as Schumann resonances. In Figure 37 it is suggested that AC power be fed to all the buildings on site. This may be acceptable for low frequency measurements, but it is very likely to spoil at least part of the spectrum detectable by the SQUID. It is thus recommended that all power at the SQUID station be kept at DC. All the equipment on site can be modified to operate off DC power and thus there is no reason to risk contaminating the site with AC power.

The electricity hut contains a battery bank that would typically be recharged using a solar panel. The batteries would then feed into a power regulator that distributes the power throughout the station. To limit the size of induced currents on the power systems, the loop area of the cables should be kept as small as possible. This implies that the buildings would typically be placed in a line rather than a triangle, with the power hut placed in the middle to keep power lines short. Induced currents, due to geomagnetic signals and man-made interference, can appear on the power lines and can feed into the electronics of the system, which in turn would affect the output and lead to higher noise signals on the SQUID. While high quality amplifiers do have large power supply rejection ratios, it is still worthwhile to limit the potential noise sources in any sensitive system.

As before the main building hosts the bulk of the electronic equipment that operates the station. Typically there would be a small on-site server where data is stored temporarily before being transmitted to a central repository. The data network could also be used to remotely monitor the condition of the observatory and issue commands, such as diagnostics on subsystems. A detailed description of the computer and telemetry network is beyond the scope of this thesis, but a brief outline will be presented here.

The telemetry system will be an essential component for the successful operation of a remote station, thus a reliable yet affordable connection to the site needs to be created. The internet provides a convenient platform for the exchange of data and it is believed that connecting to it will be the simplest method of connecting the station to the central data server.

The telephone network is the simplest method to create a robust connection to the internet through a DSL/ADSL connection, however in a remote location, no telephone network may be available. If the telephone network can be extended to the remote site then this may be a good option, however construction and maintenance cost of the line should be taken into account as well.

The other option is to make use of the free ISM radio bands, however using these frequencies come with many restrictions that may make it impractical for use with the SQUID observatory. According to FCC regulations, the maximum allowed transmission power is limited [30], and hence the maximum transmission range is typically less than 10 km. Making use of the ISM bands also implies that there would need to be a second station that would receive the data from the SQUID station and then relay it to the central database through the internet.

Perhaps the best solution to remote connectivity is a satellite based internet connection. There are many commercial products available and all that is required is a communications dish at the remote station connected to a modem. Typically the upload speeds are limited to 512 kbit/s and the download speed can be up to 16 Mbit/s [31, 32, 33]. This technology does suffer from rain fade and solar activity can also interfere with broadcasts, however these problems are temporary and the station could save the data locally until it can be broadcast.

## 5.2 Buildings and Materials

The materials used in the construction of a magnetic observatory need to be carefully tested before being included in the project. A lot of effort goes into finding and testing a site with favourable magnetic properties and it would be unfortunate if the site was ruined due to the inclusion of magnetic materials during construction. It has been found that even materials that claim to be non-magnetic by hardware suppliers, once tested, proved to deform the magnetic field. While a SQUID can only detect time-varying signals it is still important to

| Object | Distance [m] |
|---|---|
| Safety pin | 1 |
| Belt buckle | 1 |
| Watch | 1 |
| Metallic pen | 1 |
| Knife | 2 |
| Screwdriver | 2 |
| Hammer | 4 |
| Spade | 5 |
| Bicycle | 7 |
| Motor cycle | 20 |
| Car | 40 |
| Bus | 80 |

Table 4: The table shows the distance at which the object, if suitably placed and oriented, would produce a disturbance in the ambient magnetic field of 1 nT [27].

keep the area magnetic clean as far as possible. The SQUID is also a vector magnetometer, and magnetic materials in the area will change the amplitude and direction magnetic signals around them. This in turn will affect deductions made from the data that relate to the magnitude or direction of the detected signal and hence magnetic materials around the SQUID should be avoided if possible. The requirements for the station are so specialised, that the material selection should not be left to the construction contractors, but rather be supervised by someone familiar with the material requirements of a magnetic observatory.

The testing procedure is relatively simple, and hence should be performed on all materials that will be used in the observatory construction. A magnetically clean room should be used for the testing procedure. Magnetically clean means that the magnetic field over the test area should be uniform in intensity and direction. Any magnetic materials or power lines will deform the magnetic field that the sample is exposed to and could alter the outcome of the test. The person performing the test should also ensure that they have no electronic or magnetic materials on them, such as cellphones, glasses, belt buckles, and even certain shoes and buttons. Table 4 shows typical distances at which common objects cause a magnetic disturbance of 1 nT. This table illustrates the amount of care that needs to be taken to ensure that iron or magnetic objects are not in the vicinity of the sensor.

While the test is performed, the background magnetic field is likely to change due to diurnal variations in the Earth's magnetic field which would bias the test results, fortunately there are two methods of correcting for this. It is recommended that absolute magnetometers be used for this test as we are only interested in the magnitude and not the direction of the field. Furthermore, a vector magnetometer does not always have uniform responses along its different axes, if not properly calibrated, and could influence the results. If two magnetometers are available, the correction is straightforward. One magnetometer is placed in the test area and is used to detect the deformation of the field due to the object under test. The second magnetometer is placed several meters away from the test area and used to measure the variations in the background field. First,

a baseline measurement is taken to measure the difference in the readings of the two magnetometers with no object under test:

$$B_b = B_1(0) - B_2(0). \tag{5.4}$$

The object being tested is then placed in the test area, note that the orientation of the object may also influence the test result. The test object is measured at several distances away from the magnetometer, typically in steps of 10-20 cm. The deformation can then be estimated by subtracting the background field and the baseline measurement from the first magnetometer:

$$\Delta B = B_1(t) - B_2(t) - B_b. \tag{5.5}$$

If only one magnetometer is available, suitable measurements can still be made. Similar to before, the magnetometer is placed in the test area with no object under test. The magnetic field value as well as the time of the measurement is recorded for later use. The object under test is then introduced and the magnetic field as well as the time of the measurement is recorded at each distance. A second baseline measurement taken after the test is completed. By interpolating between the two baseline measurements, an estimate for the background field can be found at each sample time and subtracted from each data point:

$$m = \frac{B_{end} - B_{start}}{t_{end} - t_{start}} \tag{5.6}$$

$$\Delta B = B(t) - m(t - t_{start}) - B_{start}. \tag{5.7}$$

When using this technique, it is advisable to perform the test as quickly as possible since the linear interpolation will only be accurate over a relatively short time scale, possibly as short as a few minutes depending on ionospheric conditions. It is advisable to check with the closest magnetic observatory if there are any magnetic storms occurring before the tests are performed.

During the construction phase there are certain precautions that are recommended. As far as possible, all magnetic material, such as iron nails, should be replaced with non-magnetic materials, even in the scaffolding. The reinforcement bars in concrete are usually made from iron. Naturally these would not be allowed, however aluminium can be used as a substitute [27]. It is quite common for tools to go missing during construction, and these tools could influence the magnetic properties of the site. Thus, at the end of each day, each tool should be accounted for.

The three main requirements for the SQUID hut is a stable pillar for the SQUID, stable temperature inside the hut, and non-magnetic materials in the building [27]. The magnetic sensor is usually placed on a non-magnetic pillar that has been decoupled from the rest of the building. In practice this is done by excavating a hole up to 2 meters deep and lining it with a vibration absorbing material such as polyurethane or Styrofoam, typically the lining is between 5-10 cm thick. The pillar is then placed inside this hole and provides a stable base for the SQUID [27]. If wind were to cause the building to shake, the pillar should limit the amount of vibration that gets transmitted to the SQUID.

Changes in temperature in the support structures for the SQUID cause minor deformations due to expansion and contraction, which will affect the orientation of the SQUID and hence the output signal. In moderate

climates, temperature stability can be achieved by using cavity walls, or an insulated lining. A cavity wall is essentially just a wall with a large gap filed inside it filled with an insulator like polystyrene sheets, often used in construction. The walls of the SQUID hut at SANSA are approximately 30 cm thick, thus the insulating layer inside the cavity is roughly 10 cm thick. Similarly the roof has a ceiling with insulating material between the two layers. The hut is also constructed with the door facing South, away from the mid-day sun in the southern hemisphere, to limit the amount of thermal radiation it receives. The door is the one weakness of the SANSA SQUID hut's thermal protection as it is a simple single layer wooden door with little protection from the elements. A better solution is to build a screen in front of the door, or to have a double door system. The entire building is also painted white to limit the amount of absorbed thermal energy. The building has no windows as this would spoil the insulation provided by the walls. It has also been suggested that placing the room under ground will provide the best thermal insulation [27], however this is not advisable since it would increase the risk of creating a dangerous oxygen poor atmosphere, due to evaporating liquid nitrogen displacing the air, that could lead to asphyxiation of anyone entering the chamber.

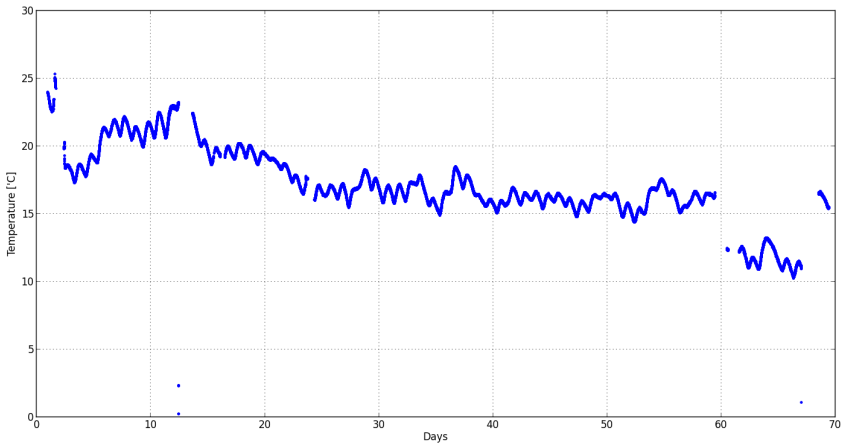


Figure 39: The figure shows the data from a temperature sensor that was placed inside the SANSA SQUID hut for a period of 70 days from 30 March to 26 June 2014. The cavity walls ensure that the maximum measured daily change in the hut's temperature was only 2.8°C even though the average daily temperature variation on the outside was closer to 11°C [34].

Figure 39 shows the data taken by a temperature sensor placed inside the hut for a period of 70 days. Even though the insulation limits the daily variation to only 2.8°C, as the seasons change the mean temperature changes more dramatically which supports the need to monitor the temperature in the SQUID hut. Considering all these factors, the optimal design for the SQUID hut is shown in Figure 40, which contains an isolation pillar, cavity walls and a two door system.

## 5.3 Site Selection

This section outlines the main aspects that need to be taken into account when selecting a location for the SQUID observatory. A detailed study using geographical information systems techniques to identify possible

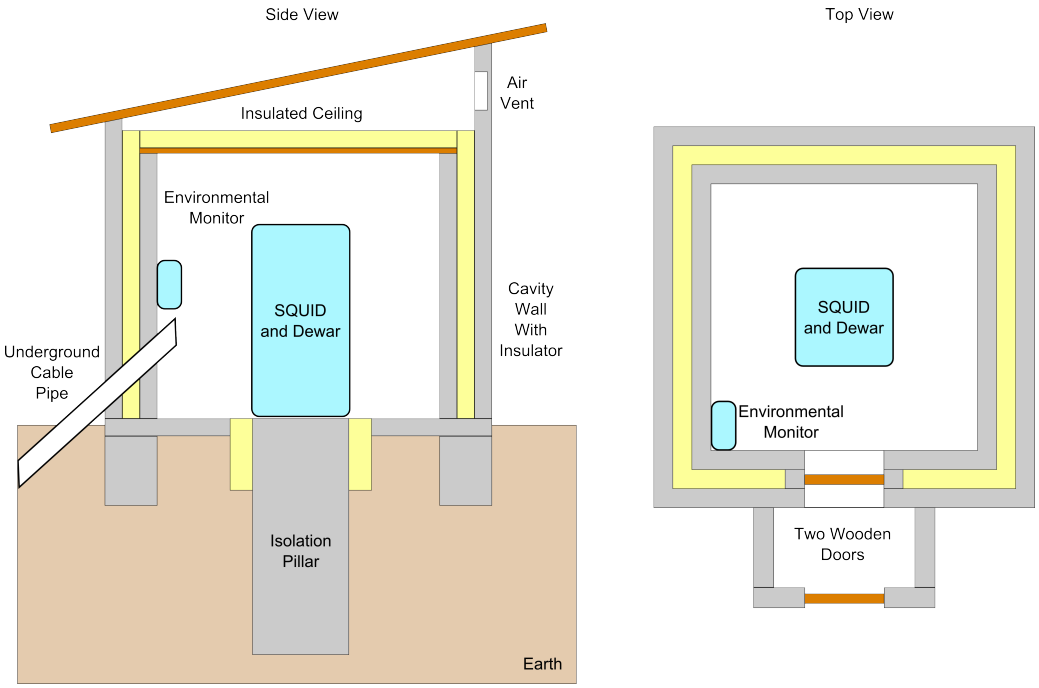


Figure 40: Taking all the recommendations into account, the figure shows a possible design for the structure of the SQUID hut. The design is very similar to what has been constructed at SANSA and what is recommended for standard observatory sites. It should be noted that the isolation pillar must be large enough to accommodate the liquid nitrogen dewar.

locations is out of the scope of this thesis. Rather, it is hoped that this section could be used by a future student or researcher as a starting point for their own project. The five main aspects that need to be taken into consideration are [29]:

- Maintenance and construction access
- Magnetic properties of site
- Power supply
- Data links
- Security

Typically a study would start by using maps and data from local authorities. Once the relevant data has been collected, it could be used to identify several possible sites for field study. Given the list of important factors, typical data that would be required include:

- Road networks
- Geological maps revealing magnetic mineral deposits
- Town maps
- Urban development plans

- Power, pipe and telephone networks
- Cellular network coverage for data exchange
- Contour maps

## 5.4 Maintenance and Construction Access

Even though the aim of the SQUID station is to be as autonomous as possible, relatively easy access to the site is still important. Firstly, the site will contain buildings which need to be constructed. Thus, the area must be accessible in the very least by a pickup truck if not by a larger vehicle. If the site is too far away from a nearby town for a daily commute, temporary housing will also be a concern for construction and maintenance teams. Since the construction is a once-off expense, lack of access may be less of a concern if the site has very favourable magnetic properties.

The SQUID needs to be cooled using liquid nitrogen which would need to be shipped in periodically. If the site has large on-site LN2 storage tanks, then refill trips would needs to be made less regularly. However, larger refill tanks may need to be transported with a truck and hence a road may need to be constructed, or a pre-existing road has to exist. If the tanks are made small enough that they can be carried by one or two technicians, then a road to the site may not be strictly necessary, but more frequent supply trips will have to be made. Currently the SQUID system at SANSA uses a 34 litre dewar, which weighs approximately 45 kg when full, and needs to be refilled every 3-4 weeks. This container can be carried by two people fairly easily, but the terrain cannot be too uneven or steep. This naturally leads to the next constraint, the site cannot be located too far from a reliable source of liquid nitrogen. Currently, the liquid nitrogen for Hermanus is shipped from Stellenbosch. The two towns are connected by a good quality road network, and the distance between the towns is roughly 100 km and takes 1.5 hours to travel one-way. Thus far, this arrangement has not resulted in any supply issues. If the road network is of poor quality however, the travel time would increase dramatically. Thus the amount of travel time is the important factor to consider here and the number of man-hours that can be dedicated to transporting the liquid nitrogen.

The need for liquid nitrogen refill trips can be eliminated, or reduced, by installing a small scale liquid nitrogen generator on-site. There are many models available and typically produce in the order of 10 litres of liquid nitrogen per day and consume less than 3kW of power [35, 36]. The production rate is high enough that it would only need to operate for a few days per month to keep the system cooled. The power consumption is low enough that it is reasonable to run it from an inverter and a battery bank. However, these systems do make use of helium compressors operating at 50 Hz and are likely to produce EM signals that would be detected by the SQUID. To reduce the noise on the SQUID, the compressor would need to be placed far away from the sensor, but pumping liquid nitrogen through long transfer lines also produces large amounts of waste as the liquid nitrogen evaporates while the transfer line is cooled.

## 5.5 Magnetic Survey

Aeromagnetic maps are sometimes used by mining companies to look for mineral deposits. These maps can also be used to look for areas with a large scale uniform magnetic field. This data can then be combined with

all the other information to identify potential locations for the SQUID observatory. Once these sites have been selected, they will need to be visited for more detailed study. One of the important aspects of the site is its magnetic profile. This can be found by performing a magnetic survey.

Local anomalies that can interfere with the SQUID include man-made signals as well as natural and artificial structures which deform the local magnetic field. Both of these would interfere with the quality of data taken by the SQUID and hence should be avoided.

One of the objectives of the magnetic survey is to determine the structure of the magnetic field around the proposed SQUID site. The survey typically produces two maps, one which shows the vertical gradient of the magnetic field and a second which shows the magnetic field strength at some fixed distance above the ground. By examining these maps, variations in the background field can be detected and these locations can be avoided, thus the final position of the SQUID hut can be determined. The goal is to place the SQUID in a location where the field is as uniform as possible, relative to its surroundings, in order to conform with international observatory standards [28, 27].

Before any measurements are taken, it would be beneficial to do a visual inspection of the site. Many man-made objects, such as powerlines and machinery, will generate magnetic interference and the first step in choosing the site should be to avoid these structures. While a minimum distance cannot be offered, it is safe to say that the further away the site is from these objects, the more likely it would be to be clear of magnetic interference.

The choice of magnetometer with which to perform the survey is an important one. The magnitude of the magnetic field is more important than the orientation. This also makes performing the survey simpler as the orientation of the magnetometer is not a concern. A magnetometer that measures the absolute field strength, such as a proton precession magnetometer, is favourable over a vector magnetometer like a fluxgate. While in principle it is possible to use a three-axis fluxgate to find the total field, this approach has a few practical issues. Firstly, there might be some misalignment of the sensing elements, resulting in the measured total field strength being dependent on the orientation of the fluxgate. Secondly, fluxgate magnetometers do not inherently measure the magnetic flux density, but rather give the value relative to some baseline. This baseline is dependant on calibration and may change over time [20]. Although small, these effects cause errors in the measurements and thus should be avoided where possible.

Proton precession magnetometers are better suited for surveys since they inherently measure the total field, thus avoiding the potential problems associated with fluxgate magnetometers. Due to the way these sensors measure the magnetic field, they are sensitive to interference from alternating magnetic fields which can result in inconsistent measurements. If measurements do not appear to be repeatable, the sensor may be suffering from interference and which would exclude the site from suitability for a SQUID station. In this event, a fluxgate magnetometer could be used to test for time varying signals in the area.

Once a site has been found that is free of any obvious sources of magnetic interference, the survey can begin. The first step is to plan how the survey will be done at the proposed site. A grid needs to be laid out that will mark the positions at which measurements will be taken. Depending on the desired accuracy, the grid can be measured out using either a marked rope or a theodolite with electronic distance measurement. The measurement points should be marked with non-magnetic markers, such as chalk powder or non-magnetic pins

that can be retrieved later. The most convenient method is to use a magnetometer that has a GPS unit built in. Given that we are not interested in the exact position which the magnetic anomalies may be, but rather a overall sense of the site, this method may still be acceptable.

Most magnetic surveys can take several hours to complete and in this time the magnetic field of the Earth will change due to diurnal variations. These variations need to be taken into account and corrected for, otherwise the data will be meaningless. This is typically done by placing a magnetometer at a base station that is out of the way of the main survey area. This magnetometer will record the magnetic field at regular intervals and time-stamp the data. This data can then be used to remove the diurnal variations in the time-stamped survey data. Since the diurnal variations are relatively slow, they only need to be measured once every few minutes, 5 to 30 minute intervals are commonly used [20]. Interpolation can then be used to correct the grid data. It is advisable to check with the local space weather agency if there was any serious solar activity which would have resulted in large variations in the magnetic field due to interactions between the solar wind and the ionosphere. These variations could lead to inconsistent data.

One of the configurations of the magnetic sensors used for the survey is called a gradiometer. Typically a gradiometer is constructed by using two magnetometers and separating them by a known distance, typically 0.5 or 1 m [20]. The gradient is then approximated by taking the difference between two simultaneous measurements of the magnetometers and dividing by the known separation. Since the magnetometers are placed a discrete distance apart, the approximation of the magnetic flux gradient is more precise the further the source is from the sensors. However, from magnetic field theory we know that the magnetic field of a source decays as $r^{-3}$ , while the gradient of that field decays as $r^{-4}$. Thus, as the source moves further away from the sensors it will be harder to detect using a gradiometer than it would be to use a single magnetometer [20]. Both single instruments and gradiometers have their advantages, and for a site survey it would be ideal to perform measurements with both instruments. Fortunately this can be done trivially by simply using the data from either one or both of the sensors to generate the field or gradient maps respectively. One of the anomalies that can be detected by the survey is the presence of buried magnetic objects. These objects typically have magnetic profiles as shown in Figure 41. The magnetic profile of these buried objects is dependent not only on its shape, but also on the latitude of the site, since the Earth's magnetic field will be different. Thus, to accurately identify anomalies takes an experienced surveyor.

Spacial aliasing may occur if "step size" is chosen to be too large, however this is typically not a problem given that the expected distortions are much larger than the typical spacing of the grid.

Once the magnetic field and gradiometer maps have been analysed and a site has been found where the magnetic field lines appear to be uniform, the next phase of the survey can begin. The observatory area should preferably not have a horizontal gradient larger than a few nT every 10 meters [27]. The second survey attempts to measure the dynamic components of the magnetic field. While it is unlikely that a survey tool with the same sensitivity as the SQUID can be found, the instrument should have the same bandwidth as the proposed SQUID station. A fluxgate magnetometer is well suited to this task. The Bartington Spectramag-06 has a flat pass-band of up to 1 kHz [26], while most SQUID stations for geomagnetic research will have a sampling rate much lower than this. At SANSA, 125 Hz is used since it is fast enough to capture the "high frequency" signals, such as Schumann resonances at 33.8 Hz. Thus, if there are any strong (relative to the sensitivity to the SQUID) time

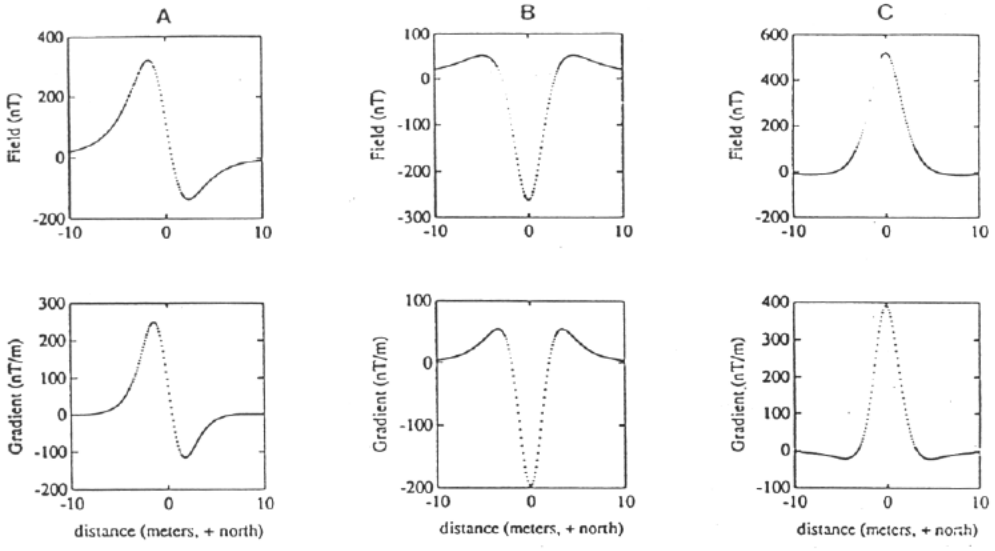


Figure 41: Field strength and gradient for a dipole source (i.e. a sphere uniformly magnetized by the geomagnetic field) as a function of horizontal distance along the Earth's surface in a South-North direction. The source has a horizontal position of 0 m and is buried at 2 m. The field and the gradient are measured at a point 2 m above the ground surface. A) Source located at mid-latitude, magnetic declination 0°, magnetic inclination 45°. B) Source is located near equator, magnetic declination 0°, magnetic inclination 0°. C) Source is located near pole, magnetic declination 0°, magnetic inclination 90°[20].

varying magnetic signals the fluxgate should be able to detect them. This will not guarantee that the site will be free of magnetic interference, but it will exclude sites that are clearly contaminated.

A fluxgate will need to be placed at each of the proposed locations at the site and allowed to take data for as long as possible. At least 24 hours of data is recommended during a weekday to show typical working conditions. A spectrogram for each dataset can now be found and checked for contamination. It is advisable to display the signal magnitude in logarithmic units to help make any small signals stand out.

Once both of these surveys reveal that the site is free of contamination, it can then be added to the final list of sites for consideration.

## 5.6 Proximity to Towns

Urban settlements are a challenge when selecting an observatory site. Naturally, urban environments generate large amount of magnetic noise due to power lines, traffic and industry. A first step was to place the observatory far from urban environments, but what is harder to predict is how those urban environments will change in the decades to come. If care is not taken, one may find that the once perfect site becomes contaminated when the local authorities build a nearby railway line, or the town expands to such a degree that the noise it generates becomes visible on the SQUID.

It would be beneficial to contact the nearby town planning authorities and work with them to understand what the plans are for the town in future. It may also be beneficial to study historical data of the town to understand what its typical development rate is. If the town area does start to converge on the observatory, it

would be worthwhile to establish a reserve area around the observatory, similarly to what was done at SANSA. The IAGA recommends that the boundary should be at least 300 m from the observatory site and at least 1 km to the nearest railroad [27]. These recommendations were made for traditional magnetometers and it is reasonable to expect that for a SQUID magnetometer these distances would be significantly greater. Due to the lack of data we cannot provide accurate estimates, however if we concede that the HTS SQUID is at least 10 times more sensitive than a fluxgate magnetometer, and the magnetic fields decay as $r^{-3}$, the minimum radius to the boundary fence should be in the order of 650 m and 2.2 km to the nearest railroad.

An unfortunate consideration that needs to be taken into account is the possibility of vandalism to the observatory. A remote magnetic observatory has the unique difficulty of being unable to be protected by nearby fences do to their magnetic properties. Currently this is still an unsolved problem and may be worth taking into consideration when selecting a site.

# 6 Remote Power System

There is a high probability that the chosen site for the SQUID observatory will not have direct access to the national power grid. Even if a grid connection is available it may still be desirable to have a standby battery system in the event of a power failure. Without this backup system, the power to the site would simply fail and unwanted gaps in the data would result. Fortunately, these systems exist as off-the-shelf commercial products and no attempt will be made in this thesis to improve on these designs. Rather, an outline will be presented that will help future designers, unfamiliar with the technology, to gain an understanding of these systems before investigating commercial solutions. This thesis will only present photovoltaic (PV) systems as they have been proven to be reliable, long lasting and require minimal maintenance. They also have the advantage, when compared to wind turbines, of only producing quasi-DC currents that should limit their effect on the station's magnetic spectrum.

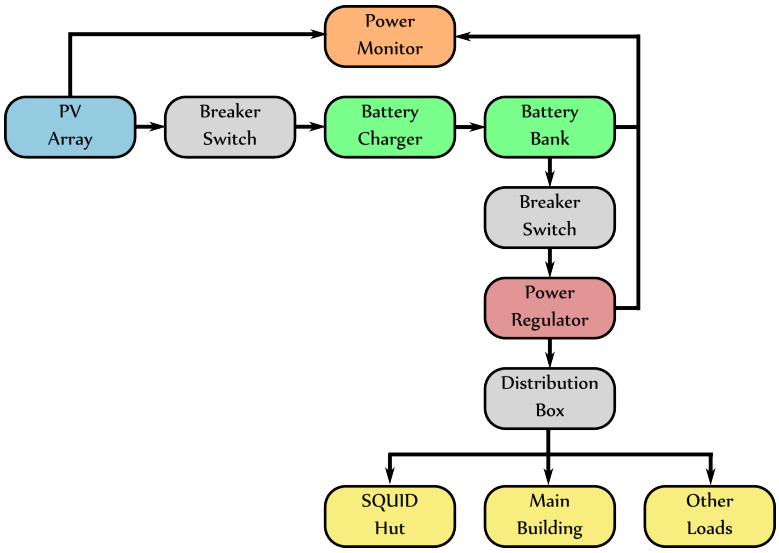


Figure 42: All the essential components for a typical grid-isolated photovoltaic power system [37].

Figure 42 shows the basic elements of a photovoltaic power system. The distribution board and the breaker switches are there to isolate the various sub-systems when maintenance needs to be performed. These also act as a failsafe if a short circuit were to occur somewhere in the system. The breaker would trip and shut down power until the fault can be repaired. In case of a failure to the power system, it would be advisable to have an isolated system in place to inform the relevant personnel of the failure and ensure that maintenance is done quickly and limit downtime.

The power monitor could help facilitate this function as its main purpose is to inform those responsible about the status of the power system. Typically these systems monitor and record the amount of power produced by the photovoltaic (PV) array, the state of charge of the batteries, and the power used by the station. Monitoring these parameters will help administration staff decide when the batteries or PV array should be replaced, as their performance deteriorates over time, as well as when general maintenance needs to be performed. Typically, PV arrays come with a 25 year guarantee on their output capacity, and after this period the solar panels are guaranteed to only degrade to 80% of their rated output [38] [39]. Thus the system designer should take this

into account when sizing the array.

The batteries in the system are usually the lead-acid type. They are typically low maintenance, relatively easy to use, and have a working life of a few years to a decade. Amongst lead-acid batteries there are several subtypes including flooded, sealed, gel-cell, and Absorbed Glass Mat (AGM). For remote applications that require low maintenance, the traditional flooded batteries are typically not used [40]. According to experiments performed by the United Arab Emirates University, which compared Gel type batteries to AGM batteries, found that the AGM batteries provided higher discharge capacity, power and efficiency by 8%, 3.6%, and 8% respectively [41]. Batteries are sensitive to temperature fluctuations, thus these should be stored in an insulated space, and in extreme cold climates a small heating unit may be required. The battery charger also needs to take this into account, as the charging voltage will also vary with temperature, and hence a temperature compensated charger should be considered. As can be seen in Figure 43, at low temperatures the resistivity of the electrolyte increases and reduces the battery's ability to deliver current. At high temperatures, the battery's capacity increases, but at the cost of shorter lifespan [41]. When monitoring batteries there are three important parameters that should be observed, these include cell voltage, current, and temperature [41]. If the batteries are used beyond their rated limits, they are likely to become damaged which will lead to increased cost, due to replacement, and possibly downtime of the observatory.

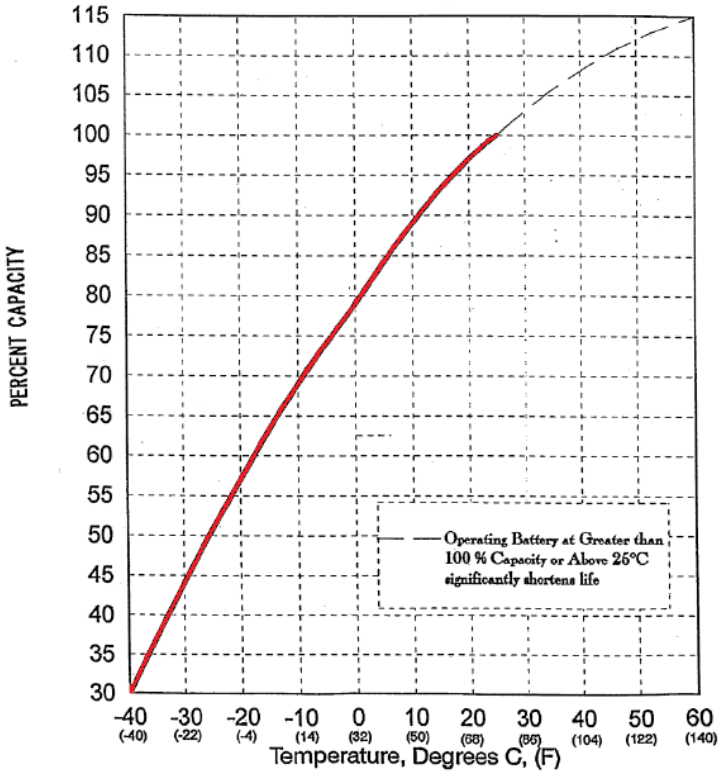


Figure 43: Capacity of the Concorde PVX series sealed AGM battery as it changes with temperature [37].

Battery capacity is normally rated in Amp-hours (A.h) or Watt-hours (W.h), and these parameters can be used to calculate how long the batteries can deliver power to a load for. For example, if a 100 A.h battery is used and 5 A is drawn from it continuously, then the battery is expected to last 20 hours before being completely depleted. Similarly a 12 V, 100 A.h battery can deliver 1.2 kW.h of electricity. It is recommended never to

discharge a lead-acid battery to more than 50% of its rated capacity, as it may shorten the battery's working life [37]. The capacity of the battery bank will greatly depend the maximum length of time that the station is required to run with no or minimal power from the solar panels. As an example, assume that the remote SQUID station requires 200 W of power on average, a low power computer uses less than 30 W of power and the SQUID electronics uses approximately 45 W of power, which still leaves a reasonable amount power for other subsystems. Climate data for the given site should then be used to help estimate the solar potential of the site. Assume that the system has to run without power from the solar array for 5 days. The longer this period of time, the larger and more expensive the battery bank will be, but the lower the probability of running out of power due to long periods without sunshine. Detailed climate information about the site would help the designer choose an appropriate value. Over the course of these 5 days, with a constant power draw of 200 W, the system would need to deliver 24 kW.h of electricity. Taking into account the maximum discharge of 50%, this value increases to 48 kW.h, and finally if we assume a power regulator efficiency of 95%, the value would need to be adjusted to a further 50.5 kW.h. This is as,

$$C_P = \frac{24nP_L}{\eta_S C_{min}}, \tag{6.1}$$

with $C_P$ the system capacity in kW.h, $P_L$ the station load in kW, $n$ the number of days the station should be able to function without sun, $\eta_S$ the power regulator efficiency, and $C_{min}$ the minimum fractional state of charge.

Now that the station capacity is known, the batteries can be selected. This can be a complex choice based on equipment available and budget. However, for this example, a 24 V lead acid battery will be used. Thus, the capacity of the battery can be determined as,

$$C_A = \frac{C_P}{V_{bat}}, \tag{6.2}$$

with $C_A$ the battery capacity in A.h and $V_{bat}$ the battery bank voltage. With these values the battery bank capacity is calculated to be approximately 2100 A.h. The battery banks are normally constructed by placing several batteries in parallel.

The efficiency of charging lead acid batteries depends on various factors including the state of charge of the battery and the rate at which the batteries are charged. Figure 44 shows how the charging efficiency changes as the state of charge increases: the greater the state of charge, the lower the efficiency. In general, a charging efficiency of 85% is accepted as a reasonable value for batteries that remain close to fully charged and will be used in this analysis [42]. The charging efficiency, $\eta_C$, is the ratio between the number of A.h or kW.h that can be extracted from the battery for every A.h or kW.h delivered to the battery.

Sizing of the solar panels is the next major consideration. First, the various mounting options should be considered. The simplest method is to mount the solar panel to a fixed bracket that cannot be changed once installed. This is the simplest method, but also produces the least amount of power due to it not tracking the sun during the day or seasons. Mounting the solar panels with a tracking system can increase the power yield between 20 % and 40% [37], but this does require the installation of electric motors which may or may not interfere with the SQUID. The final option is to use a mounting system that can be adjusted by maintenance staff as the seasons change to compensate for the change of the sun's path across the sky. When selecting the

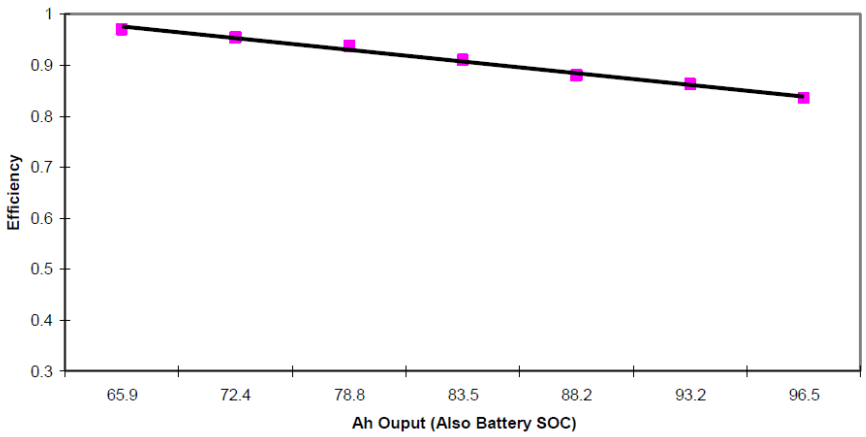


Figure 44: The charging efficiency of a lead-acid battery as a function of its state of charge. Adapted from [42].

location for the solar panels at the SQUID site, care should be taken to place them far from the SQUID sensors, but also far from anything that could cast a shadow on the panels. Any shadows on the panels greatly reduce their ability to provide power and should be avoided [43].

In general the solar panels should be pointing North in the Southern hemisphere and South in the Northern hemisphere and the tilt angle of the panel should be the same as the latitude of the site [44]. Solar panels are typically rated with a particular power output, however these ratings can be misleading since it does not take the actual conditions of the site into account and rather uses a standard light source, usually 1000 W/m$^2$, to derive the power rating. The units for solar radiation are often displayed in units of kWh/m$^2$/day, thus a more useful measure of the solar panel can be found by dividing the rated power of the solar panel by the test conditions to calculate an *effective area*, $A_{eff}$, defined as,

$$A_{eff} = \frac{P_{rated}}{I_{test}}. \tag{6.3}$$

The effective area would be the size of the solar panel if it was 100% efficient at converting incident radiation into useful electricity. Thus, a 350 W solar panel, tested with a 1000 W/m$^2$ light source, would have an effective area of 0.35 m$^2$. This effective area can be multiplied by the daily solar radiation density, $I_{sol}$ in units of kW.h/m$^2$/day, to calculate the daily power output of the solar panels in kW.h:

$$P_{sol} = I_{sol} A_{eff}. \tag{6.4}$$

Next the power resource of the site needs to be estimated. The map shown in Figure 45 shows the average annual solar power density in South Africa. This map is useful for selecting a general area with promising solar potential.

This map has two shortcomings however, it only shows the annual average solar power density, while a more useful data set would show the average daily power density for a particular month. One source of this data is Meteonorm [46], which is an organisation that provides global solar data as one of their products. Based on Figure 45, Sutherland appears to be a viable location in terms of its solar resource. The town itself is very small and mainly supports a sheep farming community. There is also a nearby optical observatory, with some of

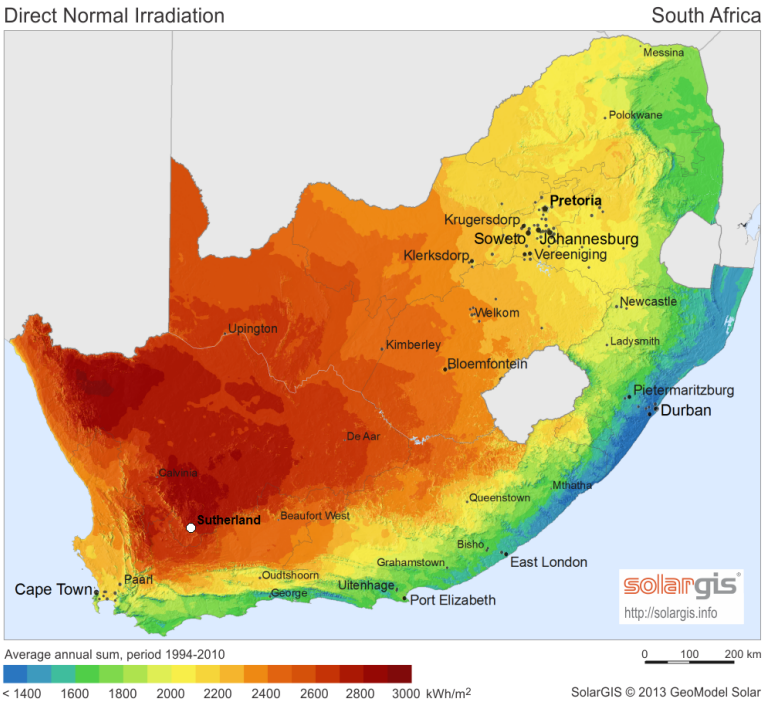


Figure 45: A map of the average annual solar power received in South Africa [45].

the telescopes making use of liquid nitrogen [47], thus a reliable supply of liquid nitrogen to the area is already available which at first glance may make this a suitable location for a remote SQUID station.

Table 5 shows the average daily solar power density in Sutherland for a given month, and can be used to estimate size the solar panel array. To calculate the average daily value, we can divide this number by the number of days in that month to generate the daily mean solar power available. The solar panels need to be sized to ensure that there is excess charging capacity for the batteries. The table shows that the minimum average daily power density is 5.0 kWh/m$^2$/day during June (Winter).

Keeping with the original assumptions of a constant 200 W power draw with a 95% efficiency, the station will require approximately 5.1 kW.h of electricity each day, which we calculate using,

$$d_P = \frac{24 P_L}{\eta_S}. \tag{6.5}$$

The excess power to charge the batteries now needs to be chosen. Typically this is done by choosing the number of days over which the station should be charged from minimum up to full capacity. The shorter the time period, the larger and more expensive the solar array will be, but if the array is too small it may be ineffective at keeping the array fully charged during cloudy months. For this example, a charging period of 7 days is chosen. The number of kW.h that needs to be stored each day in excess of ordinary power demands can now be calculated with,

$$d_C = \frac{C_P C_{min}}{m \eta_C}, \tag{6.6}$$

with $m$ equal to the number of days required for charging. Using this equation, the excess energy required for charging is calculated to be 4.3 kW.h. Thus, the total amount of energy that needs to be provided by the solar

| | Gk [kWh/m$^2$] | Daily Mean [kWh/m$^2$] |
|---|---|---|
| Jan | 238 | 7.7 |
| Feb | 207 | 7.4 |
| Mar | 217 | 7.0 |
| Apr | 189 | 6.3 |
| May | 165 | 5.3 |
| Jun | 150 | 5.0 |
| Jul | 168 | 5.4 |
| Aug | 191 | 6.2 |
| Sep | 207 | 6.9 |
| Oct | 228 | 7.4 |
| Nov | 226 | 7.5 |
| Dec | 236 | 7.6 |

Table 5: The estimated average daily solar resource for Sutherland, South Africa, generated using Meteonorm7's calculated value for the irradiation of global radiation on a tilted plane, Gk [46].

panels each day is the sum of the daily needs, $d_P$, and the excess charging needs, $d_C$, and sum to 9.4 kW.h.

The effective required area of the solar panels can now be estimated as:

$$A_{eff} = \frac{P_{sol}}{I_{sol}} = \frac{9400}{5000} = 1.88m^2. \tag{6.7}$$

Taking into account the ageing of the solar panels, the size needs to be increased by an additional 25% to compensate for the deterioration down to 80% after 25 years. Thus the final effective area for the solar panels is 2.35 m$^2$. If the 350 W solar panels described earlier are used, with an effective area of 0.35 m$^2$, then the station would require 7 panels or a 2.35 kW installed capacity.

A stand-by generator could also be installed for when solar power is not available and the battery levels become critical. The output power of the generator should be large enough to power the station as well as recharge the batteries in as short a period of time as possible. A 3 kW generator would charge the above system in approximately 11 hours, thus the magnetic spectrum of the SQUID site would only be disrupted for a short period of time assuming that the solar panels do not start charging in this time.

# 7 Liquid Nitrogen

Liquid nitrogen ($LN_2$) is the cryogen of choice for many HTS applications, as it is relatively easy to obtain and inexpensive. The cooling is performed by immersing the SQUID into an insulated dewar filled with ($LN_2$). This provides a simple and noise free method for cooling the SQUID to the required temperatures, however even though it is convenient its use is not entirely without risk and a certain level of care needs to be taken. This section describes the potential safety concerns when working with ($LN_2$), describes methods for monitoring its level in the dewar, as well as a scheme for pumping the ($LN_2$) from a refill dewar to the SQUID dewar.

## 7.1 Safety Concerns

### 7.1.1 Asphyxiation

Nitrogen gas is colourless and odourless and hence is undetectable without specialised equipment. When nitrogen boils off from its liquid form, its volume increases by a factor of approximately 700 [48, 49]. Thus if a ($LN_2$) dewar is placed in an enclosed space, without sufficient ventilation, the oxygen in the room would be replaced by nitrogen gas, especially if the room is left closed for long periods of time. At SANSA, this risk is minimised as the small room that holds the SQUID has two large doors that open to the outside and provide sufficient ventilation. If the doors were left closed while their was someone inside the hut, it could however pose a potential health risk. As the air is displaced by nitrogen gas, the decreased levels of oxygen can lead to dizziness, impaired judgement and even death. Normally, the oxygen concentration in air is approximately 20.9%, while the Occupational Health and Safety Administration of America considers an atmosphere which contains less than 19.5% oxygen to be hazardous [50]. Table 6 summarises potential health threats at various oxygen concentration levels.

| **Volume [% $O_2$]** | **Effect on a healthy person** | **Approximate time taken** |
|---|---|---|
| 15-19 | Deep breathing, faster heartbeat | Rapidly |
| 16 | Dizziness, slower reaction time | Rapidly |
| 15 | Impaired attention and coordination, intermittent breathing, rapid fatigue, loss of muscle control | Rapidly |
| 12 | Very faulty judgement, inability to move<br>Loss of consciousness, brain damage | 10 min<br>2 Hours |
| 10 | Inability to move, nausea, vomiting<br>Loss of consciousness | 4 Min<br>10 Min |
| 6 | Loss of consciousness<br>Coma<br>Death | 30 sec<br>1 min<br>5 min |

Table 6: Potential health hazards associated with an oxygen deficient atmosphere [50].

Because of these dangers, it is vital that all areas which contain liquid nitrogen be properly ventilated and that oxygen sensors be used to test an area before anyone enters. Due to the insulated nature of the SQUID huts, ensuring adequate ventilation may be difficult, thus it is recommended that care should be taken before

entering any enclosed space that has held liquid nitrogen for an extended period of time. One possible method for mitigating this risk is to seal the SQUID dewar and install a tube that will vent any excess gas safely to the outside. This will help ensure that the atmosphere inside the SQUID hut does not become oxygen deficient without compromising the thermal insulation of the building. However, this tube could also allow pressure variations from the outside to cause small vibrations on the SQUID which could lead to false signals. This effect is observed at LSBB as every time the main door is opened, a spike appears on the SQUID as a result of the pressure wave.

### 7.1.2 Cold Contact Burns

Liquid nitrogen's temperature remains at a constant 77.4 K at standard pressure [51], and thus can be extremely dangerous if skin contact should occur. Besides cold burns from direct contact with ($LN_2$), prolonged exposure to the cold vapour can damage the lungs and eyes. Fortunately it is not difficult to protect oneself by wearing proper protective equipment and handling cryogen with care. The following list describes the protective equipment recommended by AFROX [51]:

- Safety goggles should be worn when handling unpressurised cryogens.
- Full face shields should be used for pressurised systems.
- Loose fitting grease free nylon gloves should be worn (Non-porous and non-absorbent).
- Long sleeve shirts, long pants, no cuffs on trousers.
- All clothing should be non-absorbent.

Because liquid nitrogen has a very low viscosity, it will pass through any woven fabric very easily. All efforts should be taken to limit exposure to the cryogen and vapour boil-off. Handling of ($LN_2$) should be carefully planned in order to reduce unexpected events. Anyone working with liquid nitrogen should be familiar with safety and first aid procedures [48].

### 7.1.3 Pressurisation

Regardless of the quality of a dewar, there is always some heat that will leak in. The heat will cause the liquid nitrogen to slowly evaporate and the excess vapour needs to be removed from the dewar to prevent a build-up of pressure and potential catastrophic failure of the dewar. The resulting explosion poses a danger to any equipment and personal in the area. To prevent this, all dewars must be equipped with a pressure relief system that are checked periodically [48]. Often pressure vessels have redundant safety systems, such as a burst disk. If the primary pressure relief system were to fail, the burst disk is designed to rupture before the pressure vessel and prevent a catastrophic failure. Most cryogenic dewars have a vacuum shell that surround the cryogen. If the vacuum were to be suddenly lost it would result in a rapid loss of the cryogen and, if the vent tubes are not large enough for sufficient airflow, could lead to a dangerous build-up of pressure. Professional guidelines should be consulted when selecting pressure relief systems as there may be legal and safety implications for improper selection and installation of these systems [51].

Care should be taken when immersing substances into $LN_2$. Placing a room temperature object into the cryogen will result in a rapid boil-off of the $LN_2$. A path for the vapour should be provided in order to prevent a build-up of pressure and the object should be immersed slowly and carefully to limit the boiling rate. The gas that evolves from the liquid will be very cold and direct skin contact should be avoided as cold burns may result.

### 7.1.4 Ice Build Up

Ice will form on any uninsulated areas that is in contact with liquid nitrogen, specifically metal or Teflon pipes that are used to transport the liquid nitrogen. If the ice is allowed to keep growing, it can cause damage to surrounding equipment [48]. The two major concerns are the blocking of pressure relief systems and immobilisation of control valves. Most pressure relief systems work on the principle that, when the pressure builds to a predetermined value, it will vent the excess gas into the atmosphere and prevent further pressure from building. If however ice blocks the path for the excess gas to vent, it would seriously compromise the safety of the system. It is thus recommended that the pressure relief system be placed as far as possible from cold lines and preferably their pipes should never come into contact with the cryogen [49].

Preventing ice from forming on control valves is a little more challenging. Typically the cryogen has to flow through these valves and hence they will become cold, leading to the formation of ice. If the ice builds up sufficiently, it could result in the mechanism becoming frozen over, preventing an operator from using the valve. Even if the valve is still reachable, the ice could prevent, or make it harder for, the mechanism to move. To avoid these problems as much of the valve as possible is covered in insulation and the lever is mounted on a long axle to move it far from the cold source. In the case of the SQUID hut, this is less of a problem as control valves will only be used during the refill process. Typically this process only lasts a few minutes and is not enough time for critical levels of ice to form. Nevertheless, it is still useful to keep these facts in mind when considering a transfer system [48, 49].

## 7.2 Suitable Materials

Not all materials can be used at cryogenic temperatures as some become brittle and may fail if exposed to a mechanical load. Thus materials should be chosen carefully, especially if it is in direct contact with the cryogen. Table 7 is a list of materials which are suitable for cryogenic applications, although this is only a guideline and the datasheet for any material under consideration should be consulted first and small-scale tests performed.

Care should also be taken when introducing solder joints into any pipelines. In general, the tube material and the solder material have different rates of thermal expansion. The result is that the solder material deforms at a different rate than the tube material and over time this could lead to micro-fractures in the solder joint and leaks. It has been recommended that "silver solder" be used for all solder joints [53].

## 7.3 Liquid Nitrogen Monitoring

Immersion cooling is a simple and reliable method of cooling the SQUID sensors to the required temperature, but does require periodic refilling of the dewar. This method also has the advantage that no additional mechanical

| **Metallic Materials** | **Non-metallic Materials** |
|---|---|
| Austintic stainless steel (eg. 304 and 316) | $Teflon$® |
| Nickel-chromium alloys | $Mylar$® |
| Nickel | $Kapton$® |
| Monel 400 | G10 (PCB substrate) |
| Copper (Oxygen Free High Conductivity) | Various epoxies |
| Brasses | |
| Bronze | |
| Aluminium | |

Table 7: A list of known materials that are suitable for cryogenic applications [52, 51]

.

or electrical noise is introduced into the system. Since the system requires refilling, it is essential to know how much liquid nitrogen remains inside the dewar, especially in remote applications. There are several ways in which this can be measured and some of them will be discussed.

An ultrasonic range finder could be placed on the inside of the dewar lid and it could detect the distance to the liquid surface. There is however a problem with this technique. The range finder operates by sending out a high frequency burst and measuring the time until it detects the reflected sound. The calculation assumes that the speed of sound across the measured distance remains constant, however this is not true inside the dewar. The speed of sound varies dramatically with temperature and the top of the dewar may be close to room temperature, while the temperature just above the liquid nitrogen will be close to 77 K. As can be seen in Figure 46, over this temperature range the speed of sound varies by approximately 180 m/s and without knowing the temperature profile, it is unlikely to be an accurate measurement.

Infrared range finders were also found not to work due to the fact that liquid nitrogen is transparent to infrared. Hence, the top level of the liquid will not reflect the light and a direct measurement will not be possible. Placing a floating target on top of the liquid nitrogen was also considered, but due to space restrictions inside the dewar, this option was not viable.

Capacitive sensing is a common option for level sensing in liquid nitrogen applications. The dielectric constant of liquid nitrogen is 1.43, while that of air/nitrogen is very close to 1. Thus a capacitor can be constructed using multiple parallel plates or tubes that allow the liquid nitrogen to flow between the plates and act as a dielectric. The change in capacitance can then be measured and calibrated to give the level of liquid nitrogen. However, to measure the capacitance requires an alternating current to pass between the plates. This current will lead to a magnetic field in close proximity to the SQUID sensors and may disrupt the signal. If the frequency of the alternating current was made high enough then its effects on the SQUID may be negligible, however due to limited space inside the dewar for the electronics it was decided not to pursue this further.

Another option is to use several thermistors or zener diodes. Their properties vary considerably with temperature, as shown in Table 8, and make useful point measurements. They can be placed on a probe at regular intervals and used to measure the liquid nitrogen levels by simply testing the resistance or voltage of each. Additional care needs to be taken here. It is likely that over an extended period of time, the components

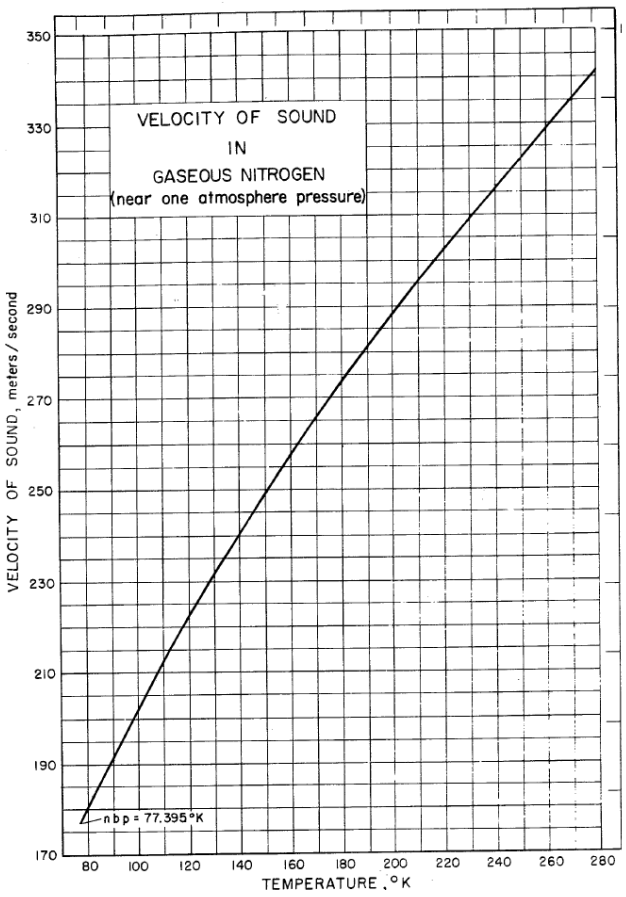


Figure 46: Speed of sound in nitrogen gas as it varies with temperature at standard pressure.

not submerged in the liquid nitrogen will be cold enough to give false readings. As a solution to this, it is proposed that heating resistors be placed in contact with the sensing elements. Before a level measurement is done the sensing elements are heated slightly. The elements in direct contact with the liquid nitrogen will cool down very rapidly, while those in contact with cold gas will do so more slowly. Thus, by measuring shortly after the heating period, an accurate measure of the liquid level can be achieved. While this method seems very promising, the heating resistors require a considerable amount of current (in the order of hundreds of mA), which in turn will generate magnetic fields and interfere with the SQUID. Thus, this option was also discarded.

Another issue with the capacitive and resistive measurements is that they need to be in direct contact with the liquid nitrogen. Anything placed inside the dewar that is also in contact with ambient room temperature will increase the rate at which the cryogen boils off. This is because they provide a conducting path for heat

| Device | Room Temperature | Liquid Nitrogen |
|---|---|---|
| Zener Diode | 1.9 V | 2.2 V |
| Resistor | 100.5 kΩ | 94.5 kΩ |
| Thermistor | 99.2 kΩ | 3.1 MΩ |

Table 8: The table was compiled by taking various passive components and submerging them in liquid nitrogen. Once cooled their properties could be measured.

into the dewar and has been found to dramatically reduce the time between refills.

Finally it was decided to use an aluminium strain gauge load cell, see Figure 47, to determine the weight of the dewar, and hence the level of the liquid nitrogen. The scale itself is placed on the isolation pillar of the SQUID hut, and the dewar rest permanently on the scale. The scale has also been designed to only move vertically even as the load cell itself flexes, thus limiting the change in sensor orientation as the liquid nitrogen level changes. A simplified schematic is shown in Figure 48.

Figure 47: An aluminium strain gauge load cell was used to determine the weight of the dewar, and hence the remaining quantity of liquid nitrogen. The scale and anti-tilt mechanism was placed on top of this type of load cell that could measure up to 100 kg.

The signal produced by the load cell is in the order of a few millivolts and hence need to be amplified. An instrumentation amplifier, INA129, was used to amplify the signal in the SQUID hut before transmitting it to to control room. Inside the control room this signal was sampled and the data is captured and stored on a local computer where it can be transmitted to a central database. Previously the digitisation of the signal was done in the SQUID hut and the value was transmitted to the control room via RS232, however it was found that the serial transmissions could be detected on the output of the SQUID and was thus the system was redesigned to transmit an analogue signal instead. The load cell scale has the advantage of never coming in contact with the liquid nitrogen itself. This avoids conduction of heat into the dewar and the limited space inside the dewar is not a concern.

## 7.4 Liquid Nitrogen Transfer

Under normal atmospheric conditions, liquid nitrogen's temperature is just below its boiling point, furthermore when it evaporates the liquid expands in volume by a factor of nearly 700. These two facts lead to a convenient method of transferring liquid nitrogen. A tube is placed at the bottom of the refill dewar along with a small heater and the dewar is then sealed. The other end of the tube is then placed in the empty dewar which is not sealed. Current is then passed through the heater and some of the nitrogen will start to boil off and pressurise the container. As the pressure builds up the liquid nitrogen is forced through the tube and into the empty dewar.

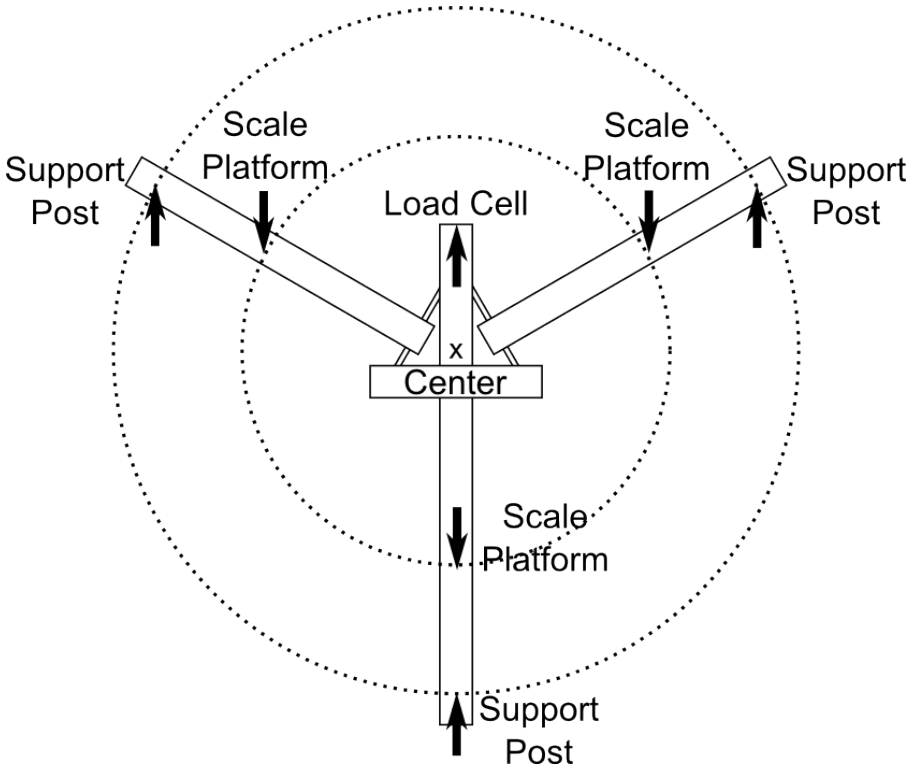


Figure 48: Simplified diagram showing top view of the scale mechanism. The three arms of the mechanism are arranged around a common central point, with the two diagonal arms being able to pivot in the vertical direction. The outer circle shows the positions of support posts, which the arms rest on. The inner circle shows the positions where the scale platform rests on top of the arms. The end of the central arm rests on the load cell. As the load is applied to the scale platform, the arms transmit the force to the load cell which flexes. The equidistant arrangement ensures that each arm tilts the same amount, hence limiting the change of orientation of the SQUID

There are several important safety aspects that need to be considered. The first point of concern is potential over pressurisation of the vessel. When dealing with a pressurised vessel it is important to have a safety mechanism that makes it unlikely for the pressure inside the vessel to exceed its safety limits.

The second issue is the material which the tube is made from. Certain materials become brittle when exposed to low temperatures and this could lead to cracks and leaks. Copper is a suitable material for the tube, it is easily acquired and relatively cheap. Teflon (PTFE) tubing is also suitable and provides more flexibility than copper, making it easier to use. Teflon is a thermal insulator, while copper conducts heat very well, furthermore the volumetric heat capacity of Teflon is 2.58 J/(K.cm$^3$), while that of Copper is 3.45 J/(K.cm$^3$). This implies that for similar sized tubing, the Teflon has less energy that will need to be transferred to the liquid nitrogen while it is being cooled. The end result is that less liquid nitrogen will be lost in the process. Insulation should be wrapped around all the tubing to limit transfer losses and to reduce the risk of frostbite due to accidental skin contact.

The third point is a pressure relief valve. Should the transfer need to be aborted it is not enough to simply switch off power to the heater. The dewar will still be pressurised and the transfer will continue until the dewar

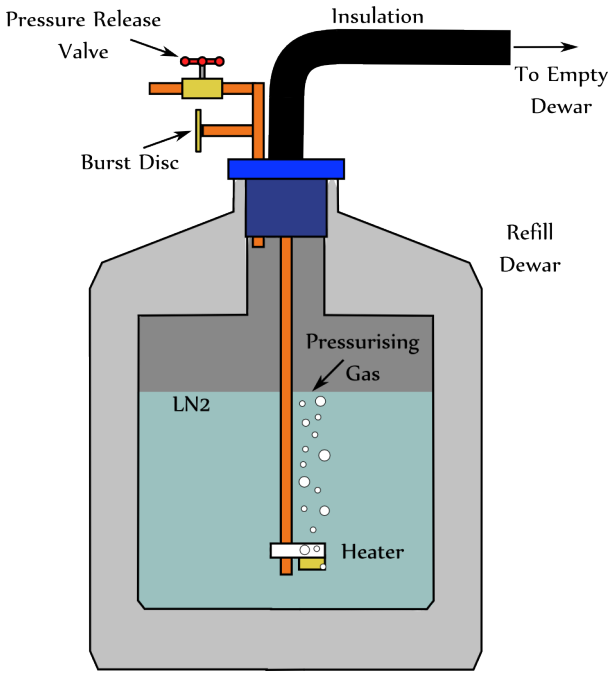


Figure 49: Liquid nitrogen transfer scheme using nitrogen vapour to pressurise the container

pressure equalises with the ambient pressure, which may take several seconds. Thus, a valve should be placed on the refill dewar which can quickly vent off the pressurising gas and stop the transfer. An overflow pipe should also be installed in the SQUID dewar to allow a controlled discharge of liquid nitrogen should too much liquid be transferred by accident.

Finally, the area in which the transfer is performed needs to be well ventilated. If this is not done the nitrogen gas could displace the air in the room and the associated health dangers discussed in Section 7.1.1.

In our prototype system, shown in Figure 49, a 2 Ohm resistor was used as our heating element and was powered by a 11.1 V Li-Po battery. This resulted in a maximum power of approximately 61 W and a measured transfer rate of 1.8 litres per minute. In the process of transferring 18.2 litres of liquid nitrogen, approximately 0.45 litres was lost. Thus, the transfer losses was measured to be 2.5%.

The steady state transfer rate can be estimated, by using the ideal gas law, as

$$PV = nRT, \tag{7.1}$$

by rearranging the equation and taking the derivative w.r.t. time. If it is assumed that the system is completely thermally insulated, and that during the transfer process the temperature and pressure remain constant, then the transfer rate can be expressed as,

$$\frac{dV}{dt} = \frac{RT}{P}\frac{dn}{dt}. \tag{7.2}$$

In the prototype system, for the transfer to take place the absolute pressure inside the dewar had to be approximately 105 kPa, and it is assumed that the temperature remained constant at 80 K, just above the boiling point of liquid nitrogen. Thus, (7.2) becomes,

$$\frac{dV}{dt} = 6.33e^{-3}\frac{dn}{dt}. \tag{7.3}$$

It would have been better to derive the constant experimentally, however due to limited time and testing equipment this was not feasible. The latent heat of liquid nitrogen, $L$, is 199.1 J/g and the molar mass, $M$, is 28 g/mol [51]. Thus we can define a new property called the molar latent heat,

$$L_m = LM \quad [\text{J/mol}]. \tag{7.4}$$

The rate at which the liquid nitrogen is converted into gas is calculated using:

$$\frac{dn}{dt} = \frac{W}{L_m}, \tag{7.5}$$

where $W$ is the power of the heating element. Substituting this back into (7.3) the transfer rate can be derived as,

$$\frac{dV}{dt} = 6.33e^{-3}\frac{W}{L_m} \quad [\text{m}^3/\text{s}]. \tag{7.6}$$

Equation 7.6 gives a transfer rate of 4.1 litres/min, which was calculated while the measured value was only 1.8 litres/min. However, this equation only includes the steady state transfer rate, while the measured rate also includes the initial period when the transfer lines had to be cooled.

# 8 Helmholtz Coils

Helmholtz coils are useful devices when working with low level magnetic fields. Their primary function is to create a quasi-uniform magnetic fields along their central axis. When three of these coils are placed perpendicular to each other they can be used to accurately and reliably generate magnetic fields in any orientation with magnitudes several times larger than the Earth's field. In this thesis, they were used primarily to cancel out the Earth's magnetic field while cooling the SQUID and to assist in the alignment of the SQUID to True North. Cooling the SQUID in a low magnetic field has been found to increase the sensor's stability by limiting the number of Abrikosov vortices that get formed in the material.

While investigating the properties of Helmholtz coils, it was also discovered that they could be used as passive low pass shields by short circuiting each coil pair. Upon further investigation it was found that the coils only produced useful attenuations when their dimensions were small, too small to be valuable in this project. This did, however, highlight the need to build the coil frames out of non-conducting materials to limit their affects on the magnetic fields at their core. This is particularly important if the SQUID is to remain permanently inside these coils as we propose. This chapter also gives an example of how to design a Helmholtz coil with its current source and proposes a method for correcting misalignment errors in a typical three-axes coil system.

## 8.1 Theory Of Operation

Helmholtz coils usually consist of a pair of identical, narrow, coaxial coils placed a specific distance apart. These coils are used to generate uniform magnetic fields along their axes and have a wide variety of uses. To understand how the coils function, we have to start with fundamental theory. Biot-Savart's law (illustrated in Figure 50) [54] states that the magnetic field generated by a current carrying conductor is proportional to the current in the wire and inversely proportional to the distance from the wire:

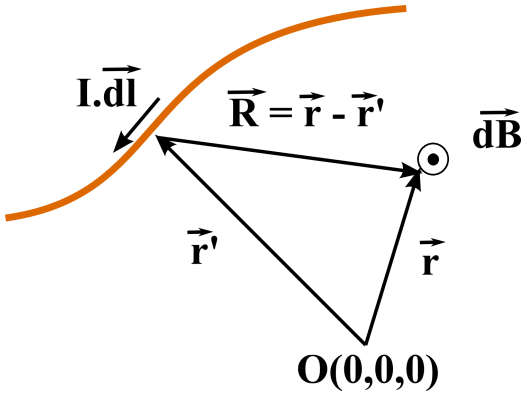


Figure 50: Biot-Savart's Law [54]

$$\overrightarrow{dB} = \frac{\mu_o}{4\pi} \frac{I\overrightarrow{dl} \times \overrightarrow{R}}{R^3}. \tag{8.1}$$

From (8.1) the magnetic field from any current distribution can be calculated, and hence can be used to describe the magnetic field of a coil system, as shown in Figure 51. The magnetic field produced at the centre of a circular coil can be calculated by integrating equation 8.1 along the current carrying loop in an appropriate

coordinate system. The resulting equation,

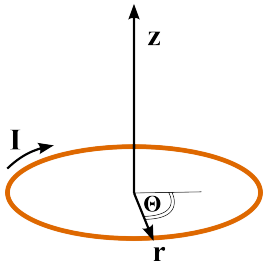


Figure 51: Magnetic field produced by a coil

$$\overrightarrow{B}(z) = \frac{\mu_0 N I r^2}{2(r^2+z^2)^{\frac{3}{2}}}\hat{z}, \tag{8.2}$$

shows the magnetic field density along the central axis of a circular loop of radius $r$, with $N$ turns in the coil, carrying a current of $I$. Thus for a two coil system, shown in Figure 52, the equation describing the field along the central axis is simply given by adding the field from two coaxial coils together:

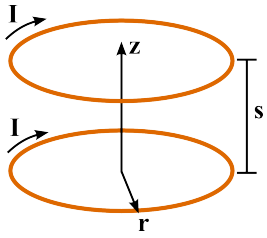


Figure 52: Magnetic field produced by coaxial coils

$$\overrightarrow{B}_{tot}(z) = \overrightarrow{B}(z) + \overrightarrow{B}(z-s) \tag{8.3}$$

$$\overrightarrow{B}_{tot}(z) = \frac{\mu_0 N I r^2}{2(r^2+z^2)^{\frac{3}{2}}}\hat{z} + \frac{\mu_0 N I r^2}{2(r^2+(z-s)^2)^{\frac{3}{2}}}\hat{z}. \tag{8.4}$$

In order for the coil pair to be considered a Helmholtz coil, the spacing of the two coils must be such that the second spacial derivative of the field distribution is equal to zero [55]. To understand the reason for this, consider Figure 53. It shows the magnetic field along the Z-axis of a circular coil. At a distance of r/2, the second derivative w.r.t. position passes through zero. This implies that the first derivative is equal to zero at this point, and hence the field is linear.

If a second identical coil is introduced and placed such that the linear regions overlap, as shown in Figure 54, then the two linear regions will add together creating an area where the magnetic field is constant.

The distance at which the second derivative of the magnetic field density becomes zero can be found as follows:

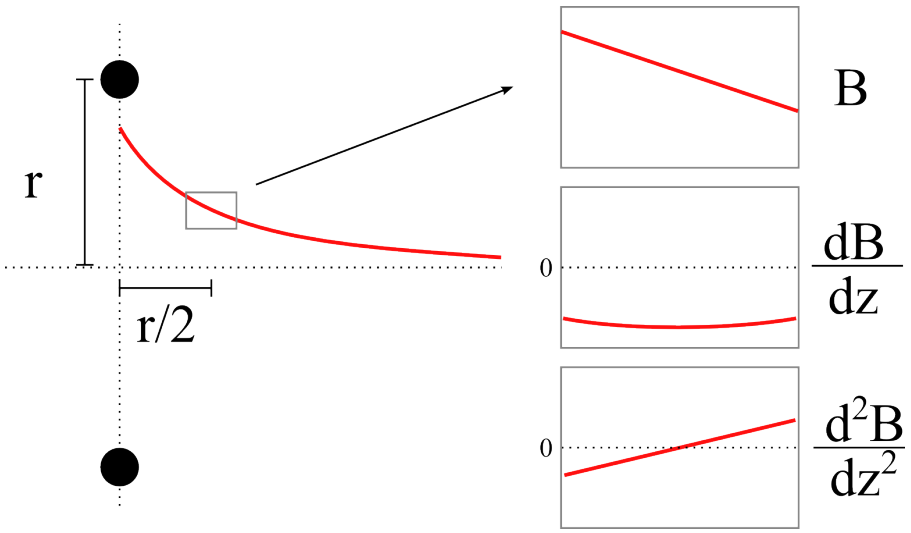


Figure 53: Magnetic field produced by the circular coil as a function of perpendicular distance from the coil, along the central axis. The radius of the coil is given by r and the inset shows the magnetic field and its derivatives at the distance r/2.

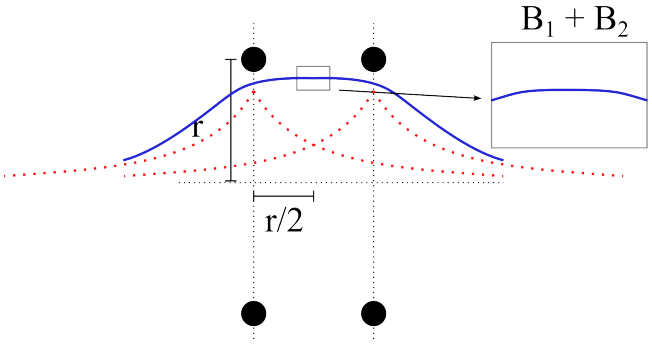


Figure 54: Magnetic field produced by circular coil showing Helmholtz condition. The dotted red line shows the magnetic field produced by each individual coil while the solid blue line indicates their sum.

$$B = \frac{\mu_0 NI}{2}\frac{r^2}{(r^2+z^2)^{\frac{3}{2}}} \tag{8.5}$$

$$\therefore \frac{dB}{dz} = -\frac{3\mu_0 NI}{2}\frac{zr^2}{(r^2+z^2)^{\frac{5}{2}}} \tag{8.6}$$

$$\therefore \frac{d^2B}{dz^2} = -\frac{3\mu_0 NIr^2}{2}\left(\frac{-5z^2}{(r^2+z^2)^{\frac{7}{2}}} + \frac{1}{(r^2+z^2)^{\frac{5}{2}}}\right). \tag{8.7}$$

Setting $\frac{d^2B}{dz^2} = 0$, the equation can be solved for the position along the z-axis where the Helmholtz condition is met:

$$\frac{d^2B}{dz^2} = 0 \tag{8.8}$$

$$\frac{-5z^2}{(r^2+z^2)^{\frac{7}{2}}} + \frac{1}{(r^2+z^2)^{\frac{5}{2}}} = 0 \tag{8.9}$$

$$\frac{-5z^2}{(r^2+z^2)} + 1 = 0 \tag{8.10}$$

$$5z^2 = r^2 + z^2 \tag{8.11}$$

$$z_0 = \pm\frac{r}{2}. \tag{8.12}$$

Thus, for a circular coil system, the Helmholtz condition occurs when the separation of the coils are equal to the radius, $s = 2z_0 = r$. Furthermore, to find the magnetic field at the centre of the coil system set $z = \frac{s}{2} = \frac{r}{2}$ in (8.4). When these two conditions are substituted into (8.4) and simplified, the magnetic field at the centre of the circular Helmholtz coil is found and described by,

$$B_c = \left(\frac{4}{5}\right)^{\frac{3}{2}} \frac{\mu_0}{r} NI\hat{z}. \tag{8.13}$$

The magnetic field for a square Helmholtz coil system can be found in a similar manner. Large square coils that will fit around the dewar tend to be easier to construct, since no special equipment is required to manufacture the coil frames. To find the magnetic field produced at their core, the problem needs to be divided up into eight integrals, one for each side of the coil pair, and the solutions can then be added together to give the solution for the full coil system. In order for a pair of square coils to be considered a Helmholtz pair, the coil separation needs to be $s = 0.5445l$, where $l$ is the side length of the square coil. The magnetic field at the centre of the square Helmholtz coil is given by,

$$B_s = \frac{4.072\mu_0}{\pi l} NI\hat{z}. \tag{8.14}$$

For the sake of brevity, these derivations have been omitted since they are very similar to the circular coils but the mathematics is more cumbersome. In general, the magnitude of the magnetic field at the centre of both coil geometries are in the form

$$|B| = k_g N|I|, \tag{8.15}$$

where $N$ is the number of turns, $I$ is the current through the coils, and $k_g$ is a constant determined by the coil geometry. For circular and square coils, $k_g$ is given by the following two expressions respectively:

$$k_{gc} = \left(\frac{4}{5}\right)^{\frac{3}{2}} \frac{\mu_0}{r} = \frac{899.2 \times 10^{-9}}{r}, \tag{8.16}$$

$$k_{gs} = \frac{4.072\,\mu_0}{\pi l} = \frac{1628.8 \times 10^{-9}}{l}, \tag{8.17}$$

where $r$ is the circular coil radius and $l$ is the square coil side length. From equations 8.16 and 8.17, it should be noted that for similarly sized coils, the square geometry produces a field magnitude that is 80% greater than the circular geometry. Other coil geometries, such as octagonal coils, do exist, but tend to be

harder to construct and hence are not that common. Configurations with a third coil called Maxwell coils tend to give better uniformity in the generated magnetic field, however the square and circular coils are the most the common and adequate for use in this project.

From (8.15), it should be noted that to generate a particular magnetic field, there is a trade-off between the number of windings and the current through the coils. Choosing a higher current will result in more complex power electronics but fewer windings on the coil, while keeping the number of windings high might simplify the power system but increase the cost of wire for the coils. There is no simple way to choose the optimum as it is dependant on many factors, but in this project it was found that keeping the maximum current below 2 Amperes kept the power electronics relatively simple, while also keeping the number of windings to a manageable number.

## 8.2 An Alternative To Metal Shielding

Magnetic shields are usually constructed from metals that have a high relative permeability. This results in magnetic field tending to move through the material rather than through the surrounding air. This property can be used to deflect magnetic field away from sensitive instruments, resulting in lower magnetic field densities where the instrument is placed. This is illustrated by the simple simulation shown in Figure 55 that was done using the magnetic simulation software FEMM [56]. The magnetic field density inside the shield is significantly lower than the external field because the magnetic field lines tend to move through the high permeability metal rather than the air inside the shield.

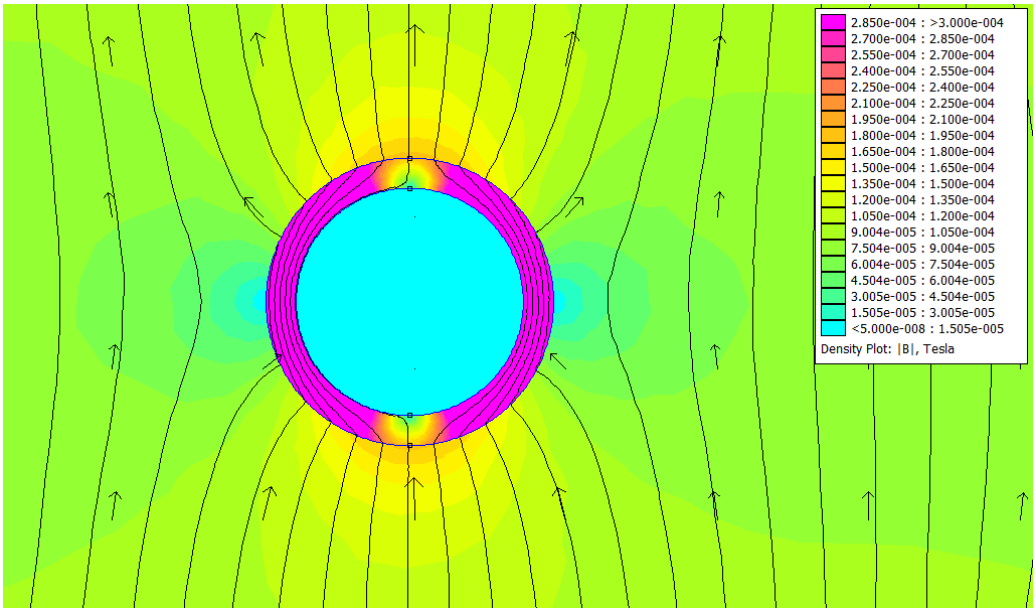


Figure 55: FEMM simulation of magnetic shield

Given the cost and complexity of operating a SQUID sensor when compared to traditional fluxgate magnetometers, it is important to ensure that the sensor is being used as effectively as possible. One of the factors that influences the performance of the SQUID is the magnetic field in which the SQUID is cooled. According to Braginski [57], as the magnetic field in which the SQUIDs are cooled is reduced, the low frequency noise of the SQUID is also reduced. If the SQUID is cooled in a large magnetic field, the formation of magnetic

Abrikosov vortices tends to occur in the superconducting material. These vortices jump between locations in the superconducting film called pinning sites and their movement gives rise to a random telegraph signal which has a 1/f power density spectrum which contributes to the low frequency noise below 1 Hz.

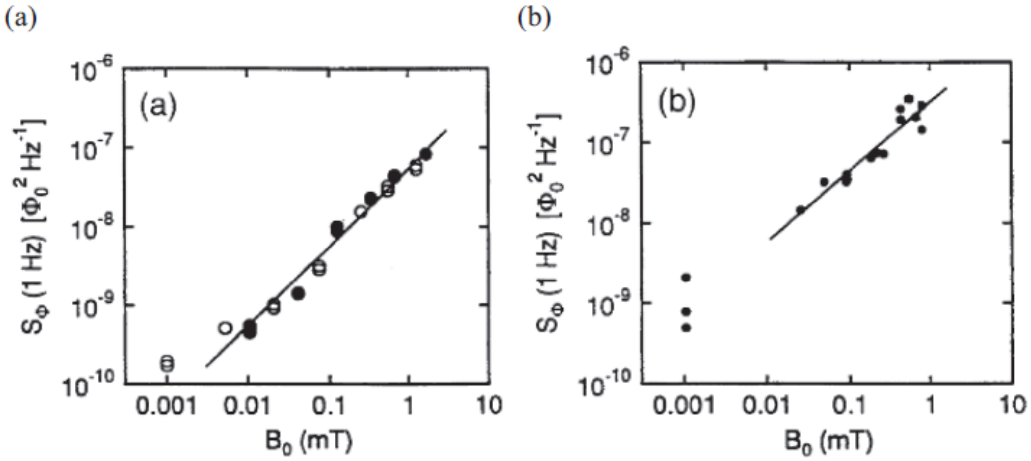


Figure 56: Flux noise $S_\phi$ (1 Hz) vs, cooling field $B_0$ (a) for a YBCO film at 77K (b) for YBCO dc SQUID with bicrystal junctions and 250 $\mu$m washer, measured with bias reversal [57]

By cooling the SQUID in a magnetic field free environment, such as inside a shield, it is possible to reduce the number of vortices formed and hence limit the 1/f noise generated in this manner, as shown in Figure 56 [57]. It should be noted that according to experimental evidence given by Dantsker et. al. [58] the increase of 1/f noise is only significant if the cooling field is greater than approximately 33 uT, depending on SQUID geometry. It is unclear what SQUID geometry is being used by the SQUID at SANSA, however it does appear that in general lowering the cooling field has positive effects on the noise level. We have found (see below) that cooling in a reduced magnetic field significantly improves stability of the SQUID sensor.

The magnetic vortices may also form in the superconducting material if it is exposed to a strong enough time varying magnetic field. For example, the removal of a high permeability magnetic shield placed around the SQUID could result in a magnetic field jump of 50 uT as the sensor is suddenly exposed to Earth's unattenuated magnetic field. This has been shown to increase the 1/f noise in the SQUID sensor, even after the shield was placed around the SQUID again [57].

This creates a conundrum for scientists wanting to use a SQUID for geomagnetic observations. It is desirable to cool the SQUID in a low magnetic field, but using a shield will also attenuate the signals that need to be detected. Secondly, the removal of the shield after cooling could result in large flux jumps and undo any benefit that was gained from the shield in the first place. The use of a metal shield has a few other problems when used with liquid nitrogen. High permeability shields tend to be expensive to construct and can be awkward to use. If the shield is large enough to fit around the liquid nitrogen dewar, the construction costs and complexity becomes significant and gaining access to the SQUIDs and the liquid nitrogen dewar becomes troublesome. If the shield is made small enough to fit inside the dewar and submerged in the liquid nitrogen, it can result in a significant loss of nitrogen as the shield is cooled. The ice formed on the shield during the cooling process also makes it difficult to remove the shield through the narrow neck of the dewar.

To solve these problems, it was decided to shield the SQUID using a three axis Helmholtz coil (Figure 57)

as opposed to traditional metal shielding. The Helmholtz coils have several advantages over metal shields for our application in this project. They are relatively easy and cheap to construct, thus keeping costs and lead time down. They can also be made large enough to fit around the liquid nitrogen dewar without significantly restricting access to the equipment inside. Furthermore, once properly calibrated and installed they can be used to cancel out the Earth's static field to a few nano-Tesla for cooling the SQUIDs. Once the SQUIDs are cooled they can be switched off very gradually, hence eliminating the large flux jump problem associated with the removal of the metal shield.

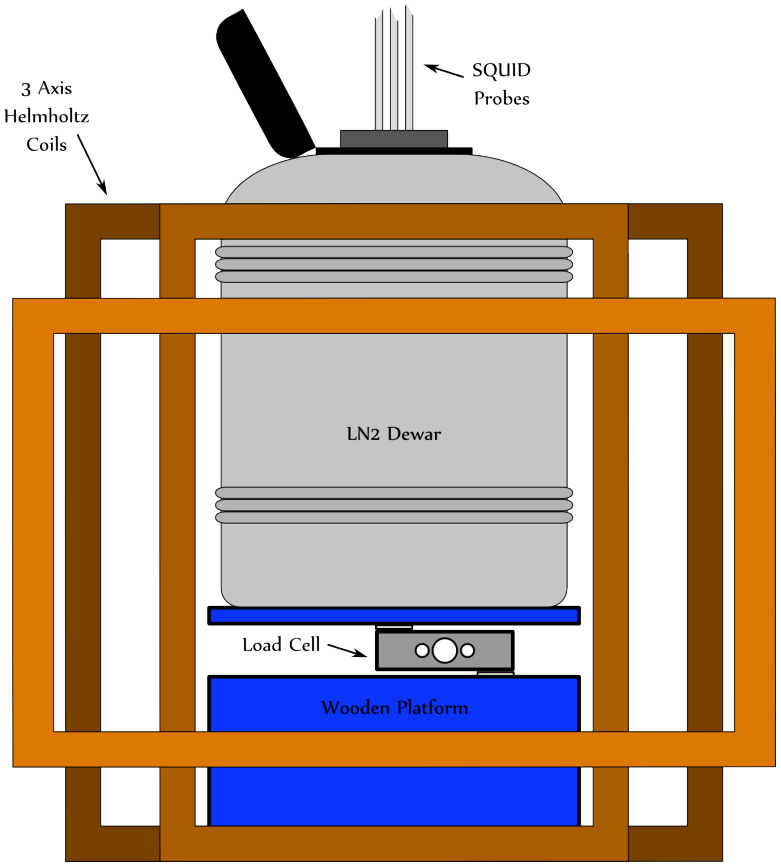


Figure 57: Coil system around the LN2 dewar with load-cell scale to measure LN2 level

Typically the cooling procedure should be done as follows to ensure optimal results. This also assumes that the coils have been properly calibrated as described in Section 8.6.

- Place the liquid nitrogen dewar inside the coils such that the SQUID's final position will be at the centre of the coil system. If this is not done, the generated fields can not be guaranteed to be uniform.
- Use the coils to cancel out the Earth's ambient magnetic field.
- Lower the SQUID into its final position in the liquid nitrogen.
- Once cold, switch on the SQUID control system and enable the built in heater to force the SQUID out of superconducting mode, then allow the SQUID to cool once more. Doing this allows the SQUID to cool in a zero ambient field without all the motion and vibration caused by lowering it into the liquid nitrogen.

- Switch the SQUID control system off and slowly shut the coils down. By switching off the SQUID's control system, you prevent its control system from trying to compensate for the coils shutting down. It is believed that this has caused stability problems in the past.
- Once the coils are switched off, the SQUID can be turned on once again and tuned.

During field testing at SANSA, the Y-channel in particular was found to be unstable. Once the SQUID was switched on it would drift towards the -10 V output rail within seconds. After tuning the SQUID using the FFT method described in Section 3.7, the stability was greatly improved, but it still tended to drift towards the -10 V rail in less than a minute with the occasional flux jumps visible on the signal. On the SANSA SQUID a flux jump is seen as a sudden change in the output signal, as the FLL locks on to the next closest working point on the sinusoidal transfer function of the SQUID. The SQUID was then cooled inside a 850 nT field produced by the Helmholtz coils, while the ambient magnetic field at SANSA is 25700 nT, and the output monitored for 10 minutes. Over this period, no appreciable drifting of the signal was observed. The coils were then slowly shut down using a dedicated analogue circuit over 20 minutes with the profile shown in Figure 58. It should be noted that an analogue circuit was used as a oppose to a digital circuit to ensure that the signal varies as smoothly as possible.

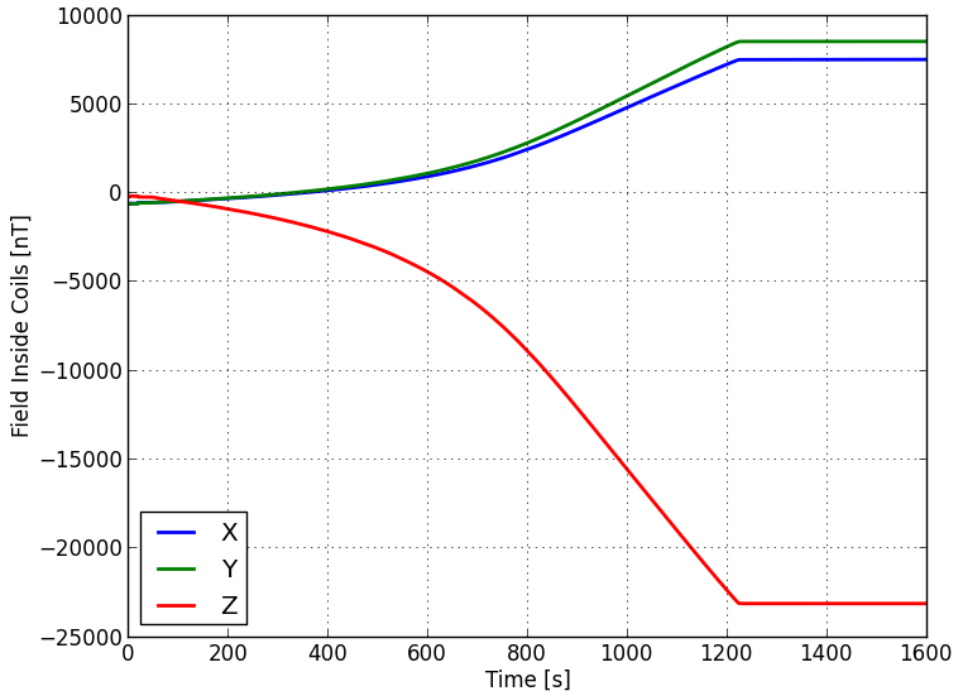


Figure 58: A Lemi-11 fluxgate magnetometer was placed inside the coils during a shut down test with a sampling frequency of 5 Hz. The magnetic field inside the coil were recorded as shown. The figure shows that the fields vary smoothly with no detectable jumps.

After the shut down procedure, the output signal was monitored again. The signal still appeared to be stable, however there may have been a slight tendency for the signal to drift, but to a much lesser degree

than before. Unfortunately, due to a problem with the data acquisition system at the time no data could be recorded. The tests show that the zero field cooling does seem to positively affect the stability of the SQUID and is recommended for SQUID operating in the ambient magnetic field [59]. It should be noted that the magnetic field at SANSA is relatively small, at 25 $\mu$T, when compared to European stations which have magnetic fields that are double that. Hence, stability problems due to high field cooling of the SQUID would only be worsened at those sites, and zero field cooling inside a Helmholtz coil should be considered.

As the test showed, it may be required to keep the coils permanently switched on to maintain the zero field in the interest of stability. This is not ideal, however, due to the potential of introducing more noise into the system. The main concern is that the current being sent to the coils, and hence the magnetic field, will change over time due to temperature variations and power supply problems. It is in principle possible to mitigate these problems by monitoring the temperature of the coil electronics as well as the current being transmitted to the coils. By doing so, it may be possible to subtract out and false signals caused by these variations.

A better solution would be to determine the optimal rate at which the current in the coils need to be reduced in order to not negatively affect the stability of the SQUID. Unfortunately, due to time constraints that experiment is beyond the scope of this thesis.

## 8.3 Alignment To True North

Aligning a system to True North can be a challenging task. It is desirable to align the SQUID sensor to True North to ensure that the data from various instruments and stations can be compared. It is also possible to rotate the SQUID data in post processing, however, to do this effectively the current orientation of the SQUID relative to True North, as well as the sensitivities of each axis needs to be known. To align the SQUID we will make use of the Helmholtz coil system placed around the SQUID. The coils, along with their control system, allows us to generate a magnetic field in any orientation. If the coil system is aligned to Magnetic North, and its control system compensates for the magnetic declination on the day of installation, then the coil system can generate a True North signal by taking the declination into account. Aligning the coil system to Magnetic North can be precisely done with the aid of a fluxgate magnetometer.

The following procedure attempts to eliminate the need for small manufacturing tolerances in the system while still allowing for accurate alignment of the SQUID:

The coil system is placed where the SQUID is to be installed and the X-axis of the coils is aligned to point roughly to Magnetic North (Figure 59).

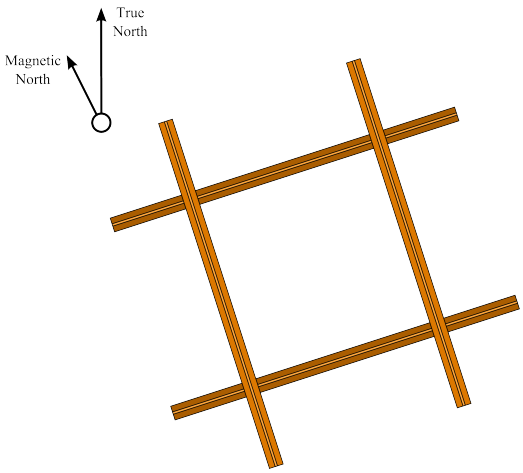


Figure 59: Helmholtz coils roughly aligned to Magnetic North.

A fluxgate magnetometer is placed at the center of the coil system. The fluxgate is rotated until it points directly to Magnetic North (Figure 60). When it is pointing in the correct direction the X-channel will be at a maximum, while the Y-channel is at a minimum.

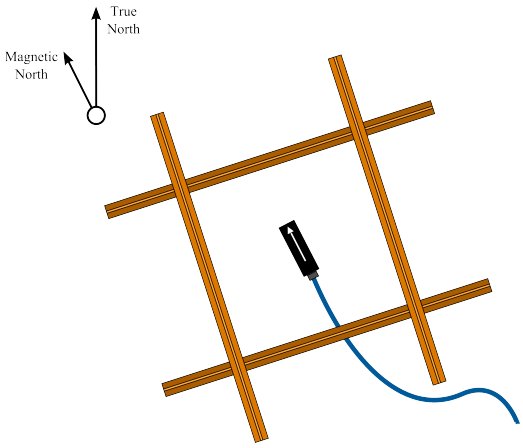


Figure 60: Fluxgate placed at centre of coils and accurately aligned to Magnetic North.

An alternating current is then passed through the X-axis of the coils (with the frequency being well within the bandwidth of the fluxgate), as shown in Figure 61.

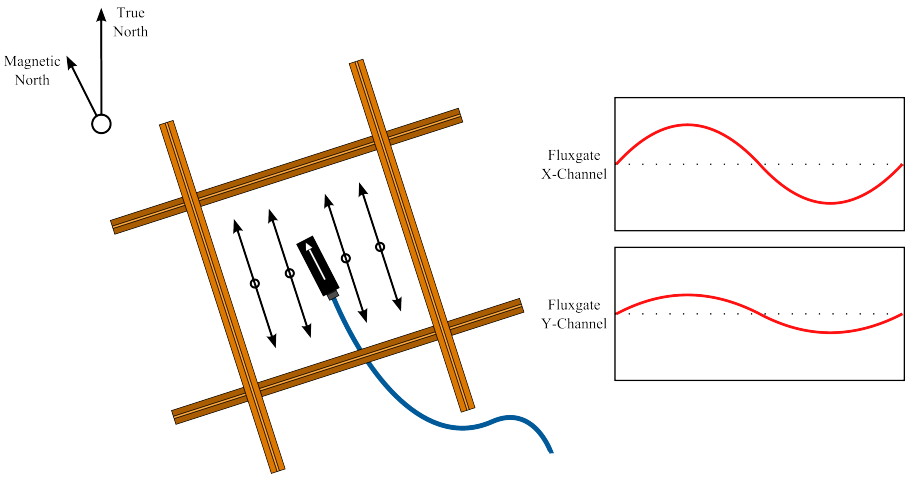


Figure 61: Time-varying signal generated in x-axis of coils (left panel). Typical output as shown in the right panel.

The coils are then rotated until the maximum field is detected by the X-channel of the fluxgate and a minimum by the Y-channel (Figure 62). It is important to ensure that the fluxgate does not move during this step. The coils are now aligned to Magnetic North.

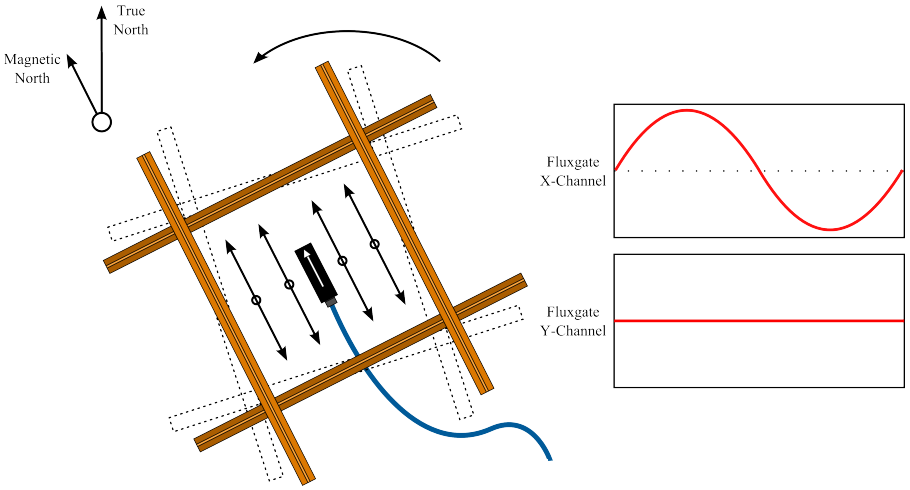


Figure 62: Helmholtz coils are rotated (without disturbing the fluxgate) until the output of the Y-channel is minimal.

The magnetic declination of the day can then be programmed into the control system of the coils, see Section 8.5.4, and hence generate a True North field. Once the SQUID is placed inside the coil system and cooled, a small alternating magnetic field can be generated in the direction of True North. Similar to before, the SQUID can be rotated until the maximum field appears on its X-channel and a minimum on its Y-channel. It is recommended that the SQUID be heated and cooled in a zero-field as described in Section 8.2 to remove any trapped flux.

It is recommended that the coil frame has a small mirror mounted to it, as demonstrated in Figure 63. This will enable a simple laser system to be used to assist in the alignment should the coils have to be removed and replaced at some point in the future. The principle is a simple one but it gives accurate results given its low cost

and complexity. An adjustable clamp with a lockable laser pointer is mounted to the inner wall of the SQUID building and a small mirror is firmly mounted to the frame of the coil system. The laser is then adjusted until it shines onto the mirror and the laser is then locked in place. The laser's reflection off the mirror onto the wall is then marked as a reference point. If the coils are rotated, the reflected dot will also move. Hence the only way for the dot to be reflected back to the marker on the wall is if the coils are placed in with the same orientation as before, in roughly the same position. If only one laser and mirror is used it is possible for large orientation errors to creep in if the coil's position is changed dramatically. Fortunately this is normally not a concern as the coils are likely to be placed in roughly the same position each time. Marks on the floor of the SQUID building can assist with this. If this is a concern, then a second laser and mirror can be installed at right angles to the first one.

To get an estimate of the placement accuracy of this system, consider Figure 64.

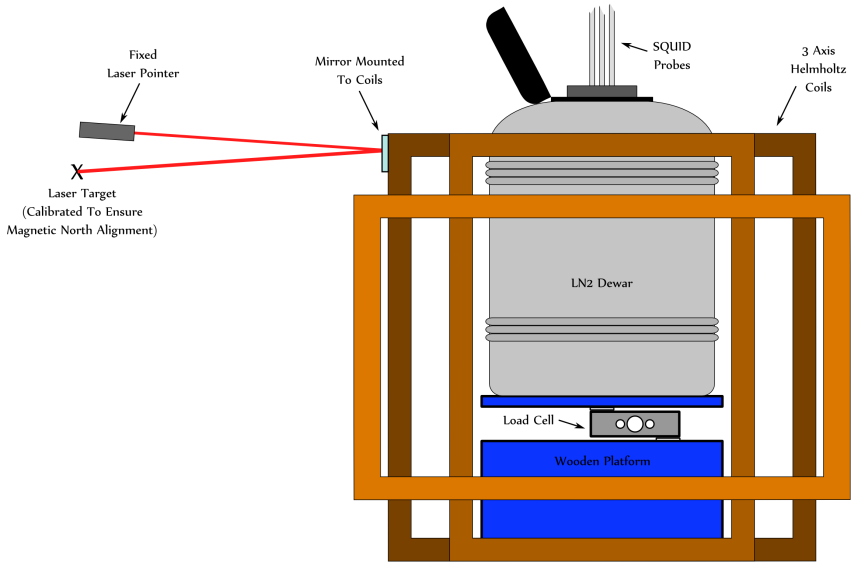


Figure 63: The proposed use of the laser system with the shield coils around the liquid nitrogen dewar

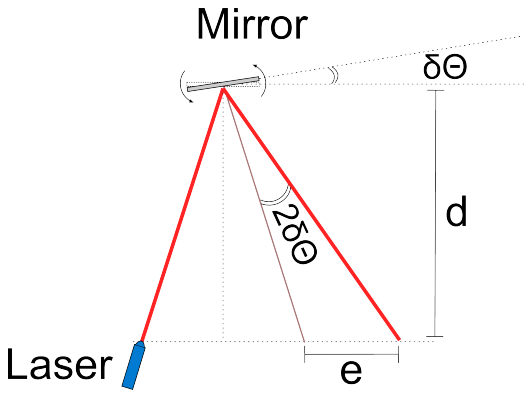


Figure 64: Laser orientation system: as the orientation of the mirror changes by angle $\delta\Theta$, the position of the reflected laser dot changes by $e$ from the zero position.

If the error angle is assumed to be small and as well as the original incident angle then the error angle can

be estimated by,

$$\delta\Theta \approx \frac{e}{2d}\left(\frac{180}{\pi}\right) \text{ degrees}, \tag{8.18}$$

where $d$ is the distance between the laser and the mirror and $e$ is half the beam width. If we assume that the system is aligned when at least half the laser beam hits the target and as a result that the change in angle, $\delta\Theta$, is relatively small, we can estimate the orientation accuracy of this system as depicted in equation 8.18. Typically the beam width is 3mm in diameter and the laser diode will be placed on the wall of the room roughly 1.1 meters away from the mirror. Under these circumstances, $e = \frac{3}{2} = 1.5$ mm and $d = 1.1$ meters. Substituting these values into (8.18) gives,

$$\delta\Theta = \frac{0.0015}{2.2}\left(\frac{180}{\pi}\right) = 0.039 \text{ degrees}, \tag{8.19}$$

which is a reasonable estimate for the typical orientation error, as verified by experimental results (see Figure 65.

A test was performed to determine the placement repeatability. A small mirror was placed on a Bartington Mag-03 fluxgate and a laser placed approximately 1.1 meters away. A 230 Hz current was then passed through a 1 metre square Helmholtz coil. This frequency was chosen as it was clearly visible using an FFT and not dominated by the harmonics of the 50 Hz power grid. The fluxgate was then orientated until the x-axis showed the maximum signal and the y-axis showed a minimum signal. The laser was then shone onto the mirror and the point of reflection was marked. The fluxgate was then removed, replaced and adjusted until the reflected laser was at the same position as before. This was repeated 40 times to determine the repeatability accuracy of this technique. The magnitude of the 230 Hz field in the X-axis and Y-axis was then used to estimate the placement orientation by taking the $\tan^{-1}$ of the channel values. The standard deviation of the placement error was found to be 0.031 degrees and the difference between the maximum and minimum error was found to be 0.129 degrees (as shown in Figure 65).

## 8.4 Passive Shielding With Helmholtz Coils

### 8.4.1 Theory

Normally Helmholtz coils are used by passing a current through them to produce a quasi uniform magnetic field. However, through experiments it was observed that if these coils were short circuited they could be used as a low pass filter to external uniform magnetic fields. As the magnetic field varies across the coils, a current will be produced inside the coils through induction. The currents will produce a magnetic field that opposes the external magnetic field, in accordance with Lenz's Law. The geometry of the coils ensures that the field produced at their centre is anti-parallel to the external field and the net result is a reduction of the magnetic field. It was found that the frequency response can be adjusted by changing the load with which the coils are terminated and that multiple coils placed inside one another can increase the maximum attenuation.

The advantage of this technique is that the cut-off frequency can be carefully designed for and construction of a Helmholtz coil is inexpensive. The coils also still give access to the device being shielded, where traditional mu metal shielding may not. Furthermore, the coils can be constructed using lightweight and non-magnetic

materials which may be advantageous in certain situations. The disadvantage however is that the maximum attenuation that these coils can provide is fairly modest and they provide no protection against low frequency signals.

The passive shielding model starts with a lumped parameter model of the coils. It is assumed that the coils can be described by an impedance in series with a voltage source, with the induced voltage in the Laplace domain, with frequency variable $s$, given by,

$$V = -2NAB_o s, \tag{8.20}$$

where $N$ is the number of turns, $A$ is the coil area and $B_o$ is the external magnetic field. Note that the factor of two is due to the two coils in the Helmholtz pair, each with N turns. From (8.20) we can determine the current, $I$, that will be induced is given by the ratio between the voltage, $V$, and the complex impedance,$Z$, as,

$$I = \frac{V}{Z} = \frac{-2NAB_o s}{Z}. \tag{8.21}$$

In general, the relationship between the magnetic field generated at the centre of the Helmholtz coils and the current flowing in through them is given by,

$$B_c = k_g N I, \tag{8.22}$$

where $k_g$ is a constant determined by the geometry of the coils, see (8.16) and (8.17). From these equations we can deduce the magnetic field generated by the Helmholtz coils due to an external magnetic field as,

$$B_c = k_g N \frac{V}{Z} = -2k_g N^2 A \frac{B_o s}{Z}. \tag{8.23}$$

Thus the total magnetic field at the centre of the coils will be,

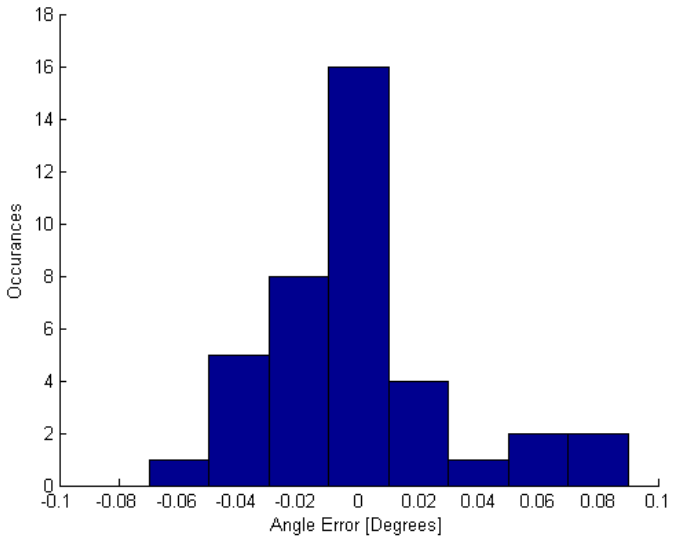


Figure 65: The laser and mirror system was used to place a fluxgate magnetometer in the same orientation repeatedly. The figure shows the estimated error distribution for this technique.

$$B_{tot} = B_o + B_c = B_o - 2k_g N^2 A \frac{B_o s}{Z}, \tag{8.24}$$

and hence the transfer function from the external magnetic field to the total internal magnetic field becomes

$$H(s) = \frac{B_{tot}}{B_o} = \frac{Z - 2k_g N^2 A s}{Z}. \tag{8.25}$$

Thus for a short circuited coil $Z = sL + R$ and (8.25) becomes,

$$H(s) = \frac{B_{tot}}{B_o} = \left(\frac{L - 2k_g N^2 A}{L}\right) \frac{s + \frac{R}{L - 2k_g N^2 A}}{s + \frac{R}{L}}, \tag{8.26}$$

which is the form for a low pass filter with a limited attenuation capability. By terminating the coil with a different load, the frequency response of the coil can be adjusted. For a capacitive load the impedance becomes $Z = sL + (R + R_c) + \frac{1}{sC}$, while for an inductive load the impedance becomes $Z = s(L + L_L) + (R + R_L)$. Note that it is important to take the equivalent series resistance (ESR) of the capacitor into account, as well as resistance of the load inductor.

### 8.4.2 Experimental Verification

To verify this model an experiment was performed that would measure the frequency response of the coil and compare it to theory. A 1 meter square Helmholtz coil was used to generate a uniform test field. This coil was driven by a voltage controlled current source and used to generate sinusoidal fields at a variety of frequencies. The shield coil under test was placed at the center of the large external coil. The shield coils for this experiment were all circular with a diameter of 15 cm. All coil frames were made from non-conducting materials. A Bartington Mag-03 fluxgate was placed at the centre of the shield coil. A diagram of the experimental setup is shown in Figure 66.

To perform the experiment, a baseline response for the large excitation coil had to be established first, to account for its low-pass nature. The shield coil under test was left open-circuited, and a sinusoidal current was passed through the excitation coil at a variety of frequencies from 10 Hz to 4 kHz. An earlier experiment confirmed that if the shield coil is terminated by an open-circuit, then it has no effect on the magnetic field at the test frequencies. The open-circuit data was used as the baseline for comparison when the shield coil would be terminated by an appropriate load. Thus, at each test frequency the shield coil response was determined by,

$$H(f) = 20\log_{10}\left(\frac{B(f)}{B_{oc}(f)}\right), \tag{8.27}$$

where $H(f)$ is the response at the test frequency, $B(f)$ is the test coil response in nT, and $B_{oc}(f)$ is the open-circuit baseline response in nT at the same frequency.

The data was captured by the fluxgate and a Fourier transform was used to extract the amplitude of the signal at the test frequency. Once the baseline was established, the coil was terminated by the test load and the measurements performed again. Figure 67 shows the results of these experiments for a variety of coils and loads and confirms the validity of the model.

Using this model it is possible to design a shield coil to have a specific cut-off frequency. Unfortunately, larger coils result in a smaller maximum attenuation. By using thicker wire, with a lower linear resistivity,

the maximum attenuation can be improved slightly, as shown in Figure 68. However, the attenuation is not significant enough to justify using these coils as part of the SQUID system. This does however indicate that the frame of the Helmholtz coils should be built from non-conductive materials and the coils should be left disconnected when not in use. If this is not done, the higher frequency components may be unintentionally attenuated.

It is possible to increase the maximum attenuation by placing several coils inside one another. However, it was found through experimentation that each coil needs to be significantly larger than the previous one to limit the mutual inductance between the coils. If the coils are strongly coupled they tend to work against each other and any benefit is lost. This limitation makes it impractical to use more than two or three coils to increase the attenuation and was not pursued further for this project.

## 8.5 Designing Helmholz Coils

When designing a Helmholtz coil there are many variables that need to be taken into account and they are often interrelated. This can make designing a Helmholtz coil system a challenging task. It is hoped that this example will help future designers build their own coils as well as show the author's methodology. In this example a square coil system will be designed. Large square coils are often simpler and cheaper to construct due to not requiring specialised equipment to make the circular frame that houses coils. The first choice that needs to be made is the size of the coil system. The larger the coils, the larger the uniform field area, but the more wire and power will be required to produce the same magnetic fields as smaller coils as shown in equations 8.16 and 8.17.

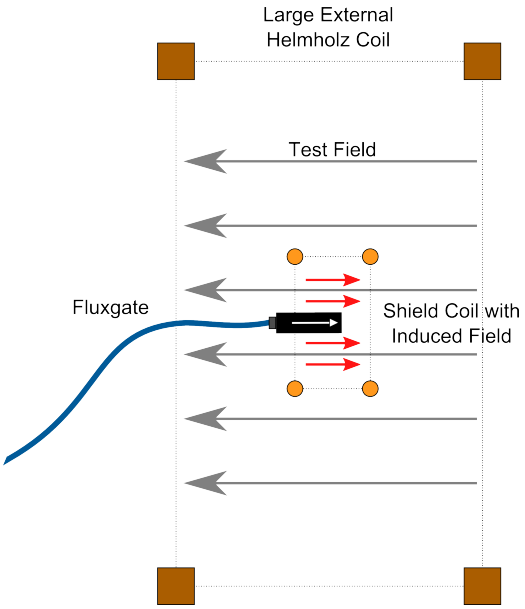


Figure 66: To test the effects of the passive Helmholtz shield, a fluxgate magnetometer was placed inside the test coil. This in turn was placed inside a much larger Helmholtz coil which was used to generate the test signals.

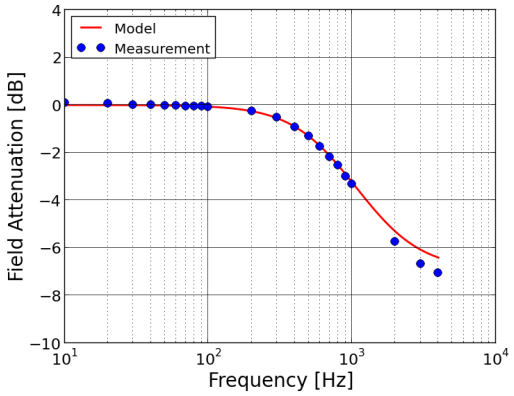


a) 15cm diameter circular coil with 30 windings

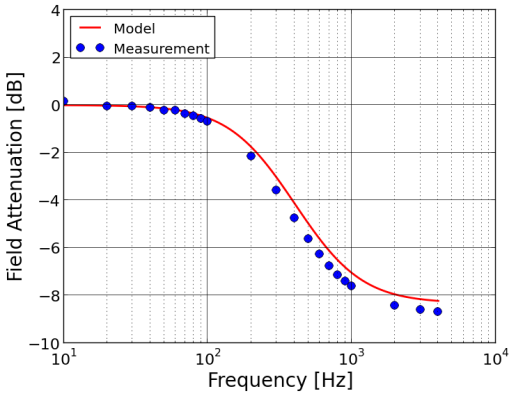


b) 15cm diameter circular coil with 110 windings

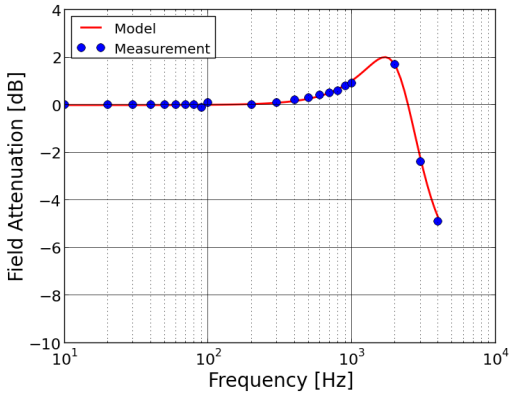


c) 15cm diameter circular coil with 30 windings and 10uF load

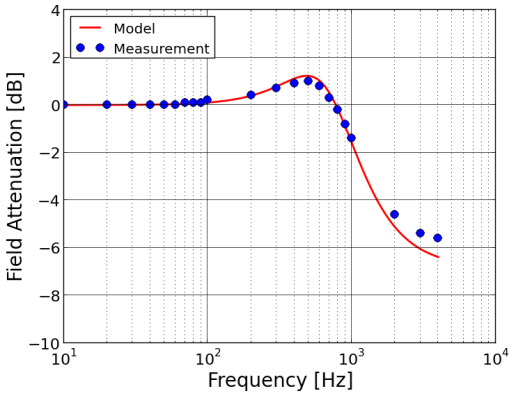


d) 15cm diameter circular coil with 30 windings and 100uF load

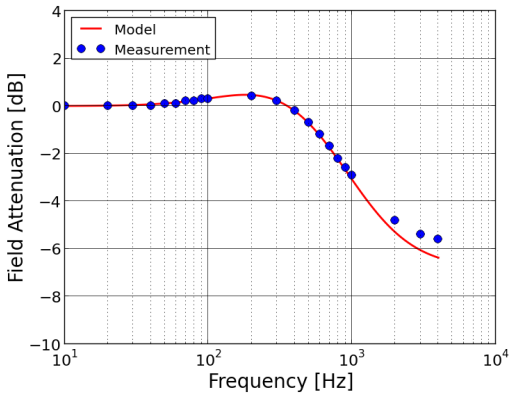


e) 15cm diameter circular coil with 30 windings and 470uF load

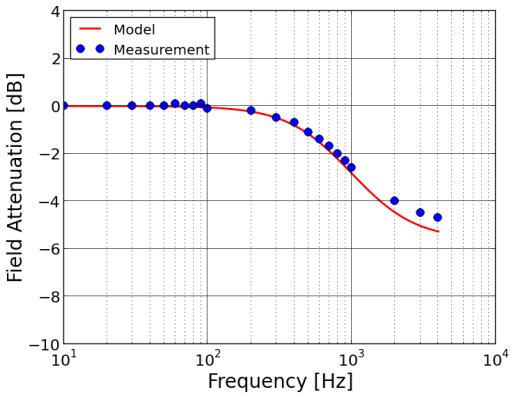


f) 15cm diameter circular coil with 30 windings and 100uH load

Figure 67: Verification of coil model from measurements

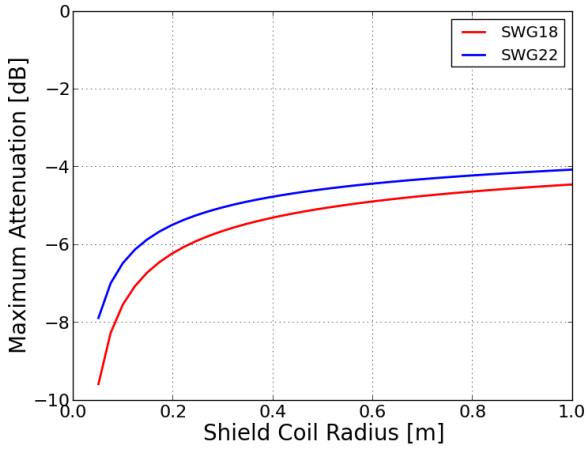


Figure 68: Maximum attenuation achieved for different coil and wire sizes based on the Helmholtz passive shielding models derived in Section 8.4.1. The thicker wire (SWG18) results in lower coil resistance and hence higher current.

### 8.5.1 Coil Size Selection

The coils used for cancelling the Earth's magnetic fields around the SQUIDs need to be able to fit around the dewar. Furthermore, the SQUID's final position, which is at the bottom of the dewar, needs to be at the centre of the coils. The dewar used at SANSA has a diameter of 48 cm and a height of 71 cm. The SQUIDs are be placed inside the dewar at a depth of 50 cm. Since the separation of the square coils is given by $s = 0.5445l$, the side length can be calculated if it is required that the dewar must fit between the two coils. Thus the separation must at least be 48 cm, however allowance should be made for the frame itself. Wooden beams commonly come in widths of 4.2 cm and is a suitable material for constructing the frame for the coils. Thus the separation needs to be increased to 53 cm to allow room for the frame and a small margin for error. The side length then becomes 97.3 cm. With this coil separation the dewar will comfortably fit inside the coils and can be positioned such that the SQUID is in the centre of the coil pair. The coil geometry term given by (8.17) can now be calculated. Substituting 0.973 for the length term and calculating gives the value

$$k_g = 1.674 \times 10^{-6}. \tag{8.28}$$

The next step is to choose the maximum field that needs to be generated. It is recommended to add a safety factor of around 25 %, especially for larger coils, to ensure that the coils perform as required. A maximum field value of 60 $\mu$T should be sufficient to cancel the Earth's magnetic field at almost any site in the world, and this value will be used for the remainder of this example. Thus, the coils will be designed to produce a field strength of 75 $\mu$T. Substituting this value into (8.15), which relates the coil geometry to the magnetic field, and solving we obtain,

$$NI = 44.8. \tag{8.29}$$

Thus, the product of the maximum coil current and the number of windings needs to be equal to 44.8 or

greater.

### 8.5.2 Power Amplifier

At this point the current source to power the coils should be chosen. After considering several amplifier and voltage-controlled-current-source designs, it was decided to use a bipolar push-pull amplifier with a current feedback resistor (see Figure 69), as this design produced no cross-over distortion and could operate at frequencies exceeding the cut-off frequency of the coils, and hence would not negatively affect the control system's response time. The current value will be fed back to an analogue control system to regulate the current and reject any disturbances.

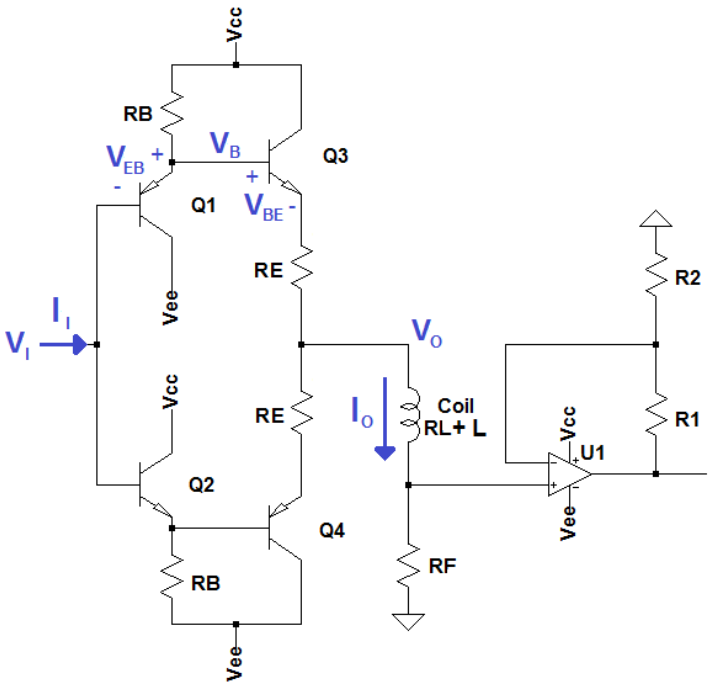


Figure 69: Push-Pull Amplifier With Current Feedback

Before this circuit can be optimised for this project, the design equations must first be derived. The important factors are the voltage gain, the current gain and the power dissipated in each of the components.

**Voltage Gain:**

By definition the relationship between the output voltage, $V_O$, and the input voltage, $V_I$, is the voltage gain. This can be found by using Kirchoff's voltage law as follows:

$$V_O + I_O R_E + V_{BE} - V_I - V_{EB} = 0 \tag{8.30}$$

$$\text{with } I_O = \frac{V_O}{R_L + R_F} \tag{8.31}$$

$$\therefore V_O \left(1 + \frac{R_E}{R_L + R_F}\right) + V_{BE} = V_I + V_{EB} \tag{8.32}$$

$$\text{since } V_{BE} \approx V_{EB} \tag{8.33}$$

$$\therefore A_v \approx \frac{V_O}{V_I} = \frac{1}{\left(1 + \frac{R_E}{R_L + R_F}\right)} \tag{8.34}$$

$$A_V \approx \frac{R_L + R_F}{R_L + R_F + R_E} \tag{8.35}$$

This parameter is normally close to 1, but it does affect several other parameters and hence it is useful to calculate it explicitly to improve the model's accuracy and hence the circuit optimisation.

**Current Gain:**

By definition the current gain is the ratio between the output current $I_O$ and the input current $I_I$. The total input current is the sum of the two base currents:

$$I_I = I_{B2} - I_{B1}. \tag{8.36}$$

If we ignore the voltage drops across the emitter resistors, $R_E$, and the base currents in $Q_3$ and $Q_4$, we have:

$$I_{B2} = \frac{(V_I - V_{BE}) - V_{EE}}{(1 + \beta_1) R_B} \tag{8.37}$$

and

$$I_{B1} = \frac{V_{CC} - (V_I + V_{EB})}{(1 + \beta_1) R_B}, \tag{8.38}$$

where $\beta_1$ is the current gain of the transistors $Q_1$ and $Q_2$. Thus combining these equation we can solve for the input current:

$$I_I = \frac{(V_I - V_{BE}) - V_{EE}}{(1 + \beta_1) R_B} - \frac{V_C C - (V_I - V_{EB})}{(1 + \beta_1) R_B} = \frac{2 V_I}{(1 + \beta_1) R_B}. \tag{8.39}$$

Since

$$I_O = \frac{V_O}{R_L + R_F} = \frac{A_v V_I}{R_L + R_F}, \tag{8.40}$$

we can estimate the current gain as,

$$A_I = \frac{I_O}{I_I} = \frac{(1 + \beta_1) A_v R_B}{2(R_L + R_F)}. \tag{8.41}$$

It should be noted that several assumptions were made during this derivation (such as assuming the transistors are identical and that their parameters do not change) and that $\beta$ can be difficult to estimate. Hence, this should only be considered an estimate and simulation should be used to verify circuit performance. This is an important parameter to determine the type of op-amps that need to be used for the control system. If the

current gain is fairly low, then the op-amps will need to supply large amounts of current to the amplifier which they may not be capable of providing.

**Power Dissipated By $Q_1$ And $Q_2$:**

The maximum power through the biasing transistors is important to know for heatsink design and can be calculated as follows. The current through the transistor, assuming that no current flows into the base of the power transistors, is given by,

$$I_E = \frac{V_{CC} - V_I - V_{EB}}{R_B}, \tag{8.42}$$

and the voltage across the transistor is given by,

$$V_{EC} = V_I + V_{EB} - V_{EE} = V_I + V_{EB} + V_{CC}, \tag{8.43}$$

with $V_{EE} = -V_{CC}$.

Thus the power through the transistor can be calculated by multiplying the voltage by the current,

$$\begin{aligned} P &= V_{EC} I_E & (8.44)\\ P &= \frac{V_{CC} - V_I - V_{EB}}{R_B}(V_I + V_{EB} + V_{CC}) & (8.45)\\ \text{Substitute } \alpha_1 &= V_{CC} + V_{EB} \text{ and } \alpha_2 = V_{CC} - V_{EB} & (8.46)\\ P &= \frac{\alpha_2 V_I - V_I^2 + \alpha_1\alpha_2 - \alpha_1 V_I}{R_B}. & (8.47) \end{aligned}$$

The maximum power can be found by calculating the first derivative with respect to the input voltage, $V_I$, and setting it equal to zero:

$$\begin{aligned} \frac{dP}{dV_I} &= \frac{\alpha_2 - \alpha_1 - 2V_I}{R_B} = 0 & (8.48)\\ 2V_I &= V_{CC} - V_{EB} - V_{CC} - V_{EB} & (8.49)\\ 2V_I &= -2V_{EB} & (8.50)\\ V_{Imax} &= -V_{EB}. & (8.51) \end{aligned}$$

Substituting this into (8.47) and simplifying we find the maximum power in the biasing transistors as,

$$P_{Q1/2} = \frac{V_{CC}^2}{R_B}. \tag{8.52}$$

**Power Disipated By $Q_3$ And $Q_4$:**

A large portion of the power will be lost over the transistors $Q_3$ and $Q_4$. The analysis for the circuit needs to be considered under two conditions. First when only one of the transistors is conducting, and second when both are conducting. This is because there is a quiescent current that flows even when there is no output signal and this current is shared by both the power transistors. In the first scenario consider only the top transistor (Q3) to be conducting. Then

$$V_{CE} = V_{CC} - (V_O + I_O R_E) \tag{8.53}$$
$$V_{CE} = V_{CC} - (A_v V_I + I_O R_E) \tag{8.54}$$
$$V_{CE} = V_{CC} - A_v V_I - \frac{A_v V_I}{R_L + R_F} R_E \tag{8.55}$$
$$V_{CE} = V_{CC} - V_I A_v \left( \frac{R_L + R_F + R_E}{R_L + R_F} \right), \tag{8.56}$$

and the transistor current is

$$I_E \approx I_O = \frac{A_v V_I}{R_L + R_F}. \tag{8.57}$$

Hence, the power can be calculated by multiplying the voltage with the current as follows:

$$P = V_{CE} I_E = (V_{CC} - V_I) \left( \frac{A_v V_I}{R_L + R_E} \right) \tag{8.58}$$
$$P = V_I V_{CC} \left( \frac{A_v}{R_L + R_F} \right) - V_I^2 \frac{A_v^2 (R_L + R_F + R_E)}{(R_L + R_F)^2}. \tag{8.59}$$

As before, the maximum power can be found by taking the derivative w.r.t. the input voltage and setting it equal to zero:

$$\frac{dP}{dV_I} = \frac{A_v V_{CC}}{(R_L + R_F)} - 2V_I \frac{A_v^2 (R_L + R_F + R_E)}{(R_L + R_F)^2} \tag{8.60}$$
$$0 = \frac{A_v V_{CC}}{(R_L + R_F)} - 2V_I \frac{A_v^2 (R_L + R_F + R_E)}{(R_L + R_F)^2} \tag{8.61}$$
$$0 = A_v V_{CC} - 2V_I \frac{A_v^2 (R_L + R_F + R_E)}{R_L + R_F} \tag{8.62}$$
$$V_{Imax} = \frac{V_{CC}(R_L + R_F)}{2A_v(R_L + R_F + R_E)}. \tag{8.63}$$

Substituting this back and simplifying we can find the maximum power dissipated in the power transistors to be,

$$P_{Q3/4} = \frac{V_{CC}^2}{4(R_L + R_F + R_E)}. \tag{8.64}$$

The resistance of the Helmholtz coil strongly influences the maximum power that will be dissipated in the transistors. It is thus highly recommended to ensure that the load is always close to the design load. If this is not done, the transistors may dissipate more power than they were designed to handle and could be damaged through overheating.

Secondly we consider the case when both transistors are conducting. Through circuit analysis, the collector current through $Q_3$ was found to be,

$$I_C' = \frac{V_I(1 - A_V) + 2(V_{EB} - V_{BE})}{2R_E}. \tag{8.65}$$

It should be noted that the fact that the NPN and PNP transistors are not perfectly matched causes the a current to flow even when there is no input signal, leading to static power dissipation. Thus the power can

be found in much the same way as before and this leads to the maximum power being achieved in this region when the input voltage is,

$$V'_{Imax} = \frac{R_E}{1 - A_V}\left(\frac{V_{CC}(1 - A_V)}{2R_E} - \frac{V_{EB} - V_{BE}}{R_E}\right). \tag{8.66}$$

This can be substituted into the power equation,

$$P'_{Q3/4} = (V_{CC} - V_I)\left(\frac{\frac{V_I(1-A_V)}{2} + V_{EB} - V_{BE}}{R_E}\right), \tag{8.67}$$

to find the maximum power dissipated when both transistors are conducting. Both transistors will be conducting when the input voltage is below a certain threshold:

$$V'_{Imax} < \frac{2(V_{EB} - V_{BE})}{1 - A_V} = V_T. \tag{8.68}$$

If $V'_{Imax} < V_T$, then both transistors will conduct when the maximum power is being dissipated and the maximum power is given by (8.67). If $V'_{Imax} > V_T$, then only one of the power transistors will be conducting when the maximum power is being dissipated and the maximum power is given by (8.64). These calculations show that the smaller the differences in $V_{EB}$ and $V_{BE}$ the less power will be dissipated in the power transistors. It is thus recommended to use matched resistors, such as the TIP41 and TIP42 for all the transistors in the amplifier.

**Power Disipated By $R_E$, $R_B$ and $R_F$:**

The maximum power dissipated through the emitter resistors and the feedback resistor occurs when the maximum load current flows through the resistors:

$$P_{RE} = I^2_{O_{max}} R_E, \tag{8.69}$$

$$P_{RF} = I^2_{O_{max}} R_F. \tag{8.70}$$

The maximum power dissipated through the base resistors occurs when transistors $Q_1$ and $Q_2$ are completely switched on. Then the power can be calculated by considering the voltage drop across the resistors:

$$P_{RB} = \frac{(V_{CC} - V_{EE})^2}{R_B} \tag{8.71}$$

$$\text{with } V_{CC} = -V_{EE} \tag{8.72}$$

$$P_{RB} = \frac{4V^2_{CC}}{R_B} \tag{8.73}$$

**Maximum Load Current:**

The maximum current flows through the output when one of the transistor branches becomes completely switched on. Assume that the top branch switches on completely. We then find that

$$V_B = I_O(R_E + R_L + R_F) + V_{BE}, \tag{8.74}$$

and also

$$V_B = V_{CC} - \frac{I_O R_B}{(\beta_2 + 1)}. \tag{8.75}$$

Where $\beta_2$ is the current gain of transistors $Q_3$ and $Q_4$. Combining these two equations, we find the maximum output current to be,

$$I_O(R_E + R_L + R_F) + V_{BE} = V_{CC} - \frac{I_O R_B}{(\beta_2 + 1)} \tag{8.76}$$

$$I_O\left(R_E + R_L + R_F + \frac{R_B}{(\beta_2 + 1)}\right) = V_{CC} - V_{BE} \tag{8.77}$$

$$I_{O_{max}} = \frac{V_{CC} - V_{BE}}{R_E + R_L + R_F + \frac{R_B}{(\beta_2+1)}}. \tag{8.78}$$

### 8.5.3 Optimal Component Selection

What is considered optimum greatly depends on what constraints the project is facing. In order to choose the best combination of values the circuit must first be fully understood. In Section 8.5.2, all the design equations have been derived for the power amplifier that will be used in this project. A second factor which plays an important role is the cost of constructing the coils themselves. The size and material of the frames have been fixed by other constraints and hence there are no parameters to optimise for the frames. However, the wire used for the coils still needs to be chosen. To this end, local suppliers of wire were sourced and their prices collected as shown in table 9.

Using this table and the design equations derived previously, it is possible to write a computer program to calculate the optimal component values for our amplifier (see Appendix A). Figure 70 shows the cost and power dissipation in each component for different maximum currents and wire choices. The power graph also shows the effects on power wasted based on the choice of the feedback resistor. In general the higher the feedback resistor, the more power is dissipated by other components, specifically the base resistors.

Only three wire sizes produced valid results, and hence the choice is made much simpler. The primary trade-off when selecting maximum operating current appears to be between power dissipation to coil construction cost. The higher the current, the fewer windings are needed and hence the lower the cost for wire, but the greater the amount of power that needs to be dissipated through the amplifier's components. It was decided to use a maximum output current of 2.0 Ampere using SWG19 wire. This choice offered a low cost and fairly low power dissipation by transistors. To minimise the noise fed back to the control system, the feedback resistor should be made as large as possible. Thus, with the aid of a SPICE simulation, it was found that a 1.0 Ω resistor was the maximum value that still allowed the amplifier to deliver 2.0 A of current. This resulted in a coil with

$$N = \frac{44.8}{I_{max}} = \frac{44.8}{2.0} \approx 23 \text{ windings}. \tag{8.79}$$

| **Standard Wire Gauge** | **Diameter** | **Area** | **Linear Resistivity** | **Linear Density** | **Cost Density** |
|---|---|---|---|---|---|
| SWG | mm | $mm^2$ | ohm/km | g/m | ZAR/g |
| 18 | 1.220 | 1.170 | 14.8 | 10.40 | 0.2628 |
| 19 | 1.020 | 0.811 | 21.3 | 7.23 | 0.3255 |
| 20 | 0.914 | 0.657 | 26.3 | 5.86 | 0.2336 |
| 21 | 0.813 | 0.519 | 33.2 | 4.63 | 0.3565 |
| 22 | 0.711 | 0.397 | 43.4 | 3.54 | 0.3633 |
| 23 | 0.610 | 0.292 | 59.1 | 2.60 | 0.3743 |
| 25 | 0.508 | 0.203 | 85.1 | 1.81 | 0.3743 |
| 27 | 0.417 | 0.136 | 127.0 | 1.22 | 0.4548 |
| 30 | 0.315 | 0.078 | 221.0 | 0.70 | 0.3400 |
| 33 | 0.254 | 0.051 | 340.0 | 0.45 | 0.3743 |
| 36 | 0.193 | 0.029 | 589.0 | 0.26 | 0.3400 |

Table 9: Standard Wire Gauge properties and local costs.

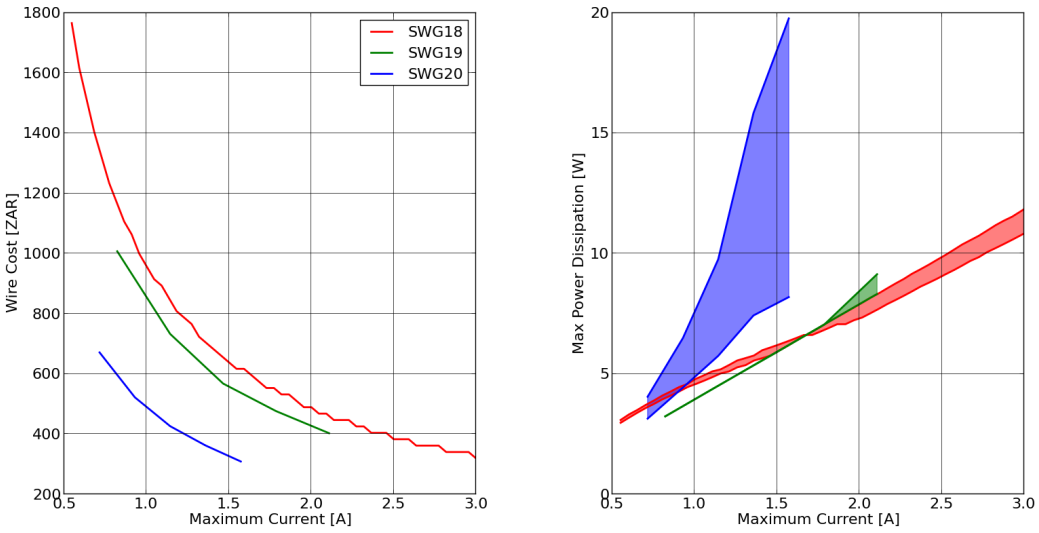


Figure 70: *Left panel:* Cost as a function of maximum current for different wire gauges. *Right panel:* Maximum power dissipated by any component in the circuit as a function of maximum current, for different wire gauges and over a wide range of resistor values.

Thus each coil requires approximately 180 meters of wire. Since SWG19 wire has a linear resistivity of 21.3 $\Omega/km$, this results in a coil resistance of approximately 3.8 Ω. The inductance of the coil can be estimated using [60] as,

$$L_{square} \approx N^2 \frac{4l\,\mu_0}{\pi}\left(\ln\left(\frac{l}{r_w}\right) - 0.774\right) = (23)^2\,\frac{4(0.973)\,\mu_0}{\pi}\left(\ln\left(\frac{0.973}{0.00051}\right) - 0.774\right) = 5.6 \text{ mH}. \quad (8.80)$$

The inductance value will be useful later when designing the control system. Only the base and emitter resistor values still need to be chosen. A computer program was written to do this. The design equations derived earlier were used to calculate the maximum power dissipated in each component. Then a large variety of base and emitter values were chosen and the combination that yielded the lowest power loss in the amplifier components was selected. The procedure outlined above yielded the component values listed in table 10.

| Component | Design Value |
|---|---|
| Transistors | TIP41/42 |
| $R_B$ | 47 Ω |
| $R_E$ | 0.1 Ω |
| $R_F$ | 1.0 Ω |
| Coil Geometry | Square |
| Side Length | 97.3 cm |
| Coil Separation | 53 cm |
| Coil Windings | 23 |
| Coil Resistance | 3.8 Ω |
| Coil Inductance | 5.6 mH |
| Wire Length | 180 m |
| Wire Gauge | SWG19 |
| Max Current | 2.0 A |
| Max Field | 60 uT |
| Power $R_B$ | 11.8 W |
| Power $R_E$ | 0.4 W |
| Power $R_F$ | 2.0 W |
| Power $Q_{1/2}$ | 3.0 W |
| Power $Q_{3/4}$ | 7.3 W |

Table 10: Component values resulting from Helmholtz coil design, utilising the program in appendix A.

**Heating Considerations:**

Providing adequate cooling for the amplifier components is critical to the operation of the circuit. As the temperature of the transistors increases, their ability to safely dissipate power decreases. The maximum anticipated power loss across the transistors is 7.3 W. If we include a safety margin, then the maximum power we will allow the transistors to dissipate is 15 W. Thus according to the power derating curve of the TIP41/42, found in their datasheets, the maximum junction temperature is 120°C. Given a maximum ambient temperature of 40°C, this implies a maximum temperature rise of 80°C for each transistor. Thus, the heatsinks must be chosen to give the transistors a thermal resistivity of at most 10 $K/W$. A SPICE simulation of the circuit shows no significant

change in the power dissipation of the amplifier components over between 40°C and 120°C.

The feedback resistor supplies the signal to the control system that regulates the current. As this resistor heats up, its resistance will change and hence the signal that is fed back will change as well even though the current may remain the same. Assuming that the control system will ensure that the voltage that is fed back remains constant, then,

$$V = (R + \Delta R)(I - \Delta I) \tag{8.81}$$

$$V = RI + I\Delta R - R\Delta I - \Delta I\Delta R. \tag{8.82}$$

Since the change in voltage is zero, then the change in current and resistance must cancel each other out. Hence,

$$\Delta V = 0 = I\Delta R - R\Delta I - \Delta I\Delta R \tag{8.83}$$

$$\Delta I = \frac{I\Delta R}{R + \Delta R}. \tag{8.84}$$

The sensitivity, S, of the coils we have designed is 30 $\frac{\mu T}{A}$ and the temperature coefficient of the feedback resistor, $k_T$, is typically in the region of 100 ppm. Thus the change in magnetic field due to change in resistor temperature can be expressed as:

$$\Delta B = \frac{SI\Delta R}{R + \Delta R} \tag{8.85}$$

$$\text{with } \Delta R = k_T R \Delta T \tag{8.86}$$

$$\therefore \Delta B = \frac{SIk_T R\Delta T}{R + k_T R\Delta T}. \tag{8.87}$$

Thus allowing a temperature variation of 20°C, due to ambient temperature and self heating, the magnetic field in our system is expected to vary by approximately 120 nT, which is unacceptable. Assuming that adequate cooling can be provided, it is possible to decrease this variation by increasing the resistor value, as seen in Figure 71. However, our resistor value is already as large as we can reasonably make it. Thus, the only option that remains is to install a temperature sensor to monitor the temperature of the resistor. Through careful calibration, it should be possible to compensate for the temperature variations using the control system.

### 8.5.4 Control System

The control system is responsible for regulating the current through the coil system and rejecting any disturbances. After an initial investigation it was decided to implement an analogue control system as opposed to a digital control system. Both systems would cost approximately the same, but it was determined that the analogue control system performed better at rejecting disturbances. Figure 72 shows the control loop for one of the Helmholtz coil pairs.

The reference voltage, $R$, is generated by the computer through a Digital to Analogue Converter (DAC) and controls the current that will flow through the coils. The control system, $D(s)$, is responsible for ensuring that

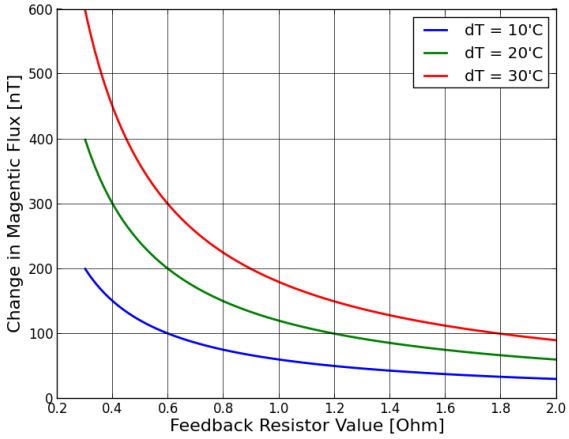


Figure 71: Relationship between field variation and feedback resistor value due to temperature changes

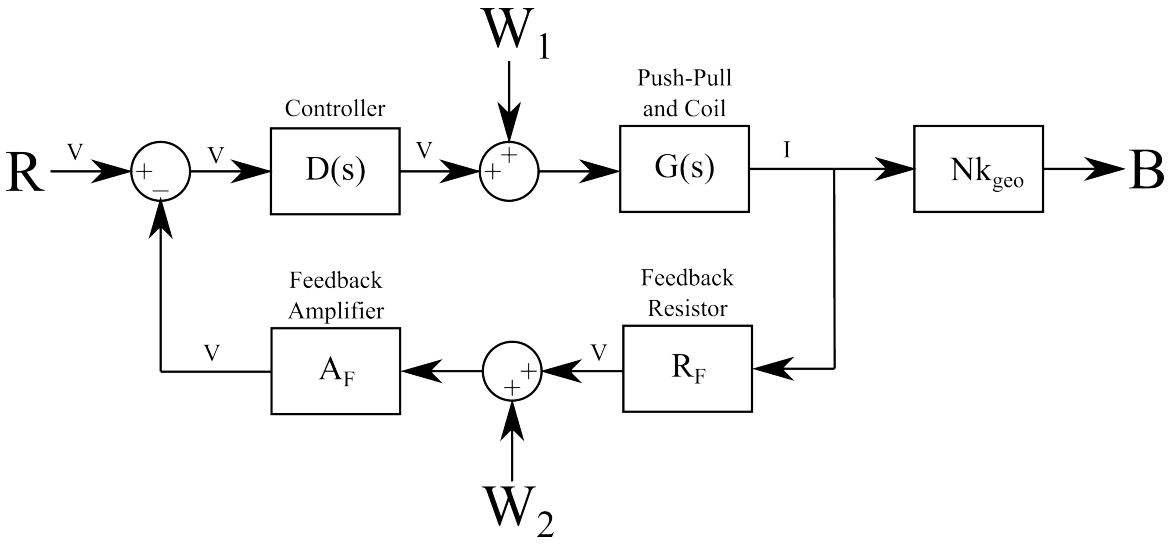


Figure 72: Analogue control loop, showing how the reference voltage $R$ and the noise $W_1$ and $W_2$ affect the output magnetic field $B$.

the current through the coils, $G(s)$, is equal to the desired current dictated by R. The magnetic field generated by the coils, $B$, is proportional to the current passing through them, $I$, according to the relation,

$$B = Nk_g I, \tag{8.88}$$

where $N$ is the number of windings on the coil, $k_g$, is a constant determined by the geometry of the coil. For the control system to function, a feedback loop has to be provided. This is done by placing a resistor, $R_F$, in the current path and feeding the voltage back to the control system through an amplifier, $A_F$. Noise signals, $W_1$ and $W_2$, were modelled as voltage sources that could enter the system as indicated in Figure 72.

The Helmholtz coil can be represented by an inductor and resistor in series with each other. Since the resistance of the coil is typically comparable to the push-pull amplifier's emitter resistor, and the feedback resistor, these should be taken into account when modelling the coil, as shown in Figure 73.

By analysing the circuit in the Laplace domain, the current through the coil can be determined as,

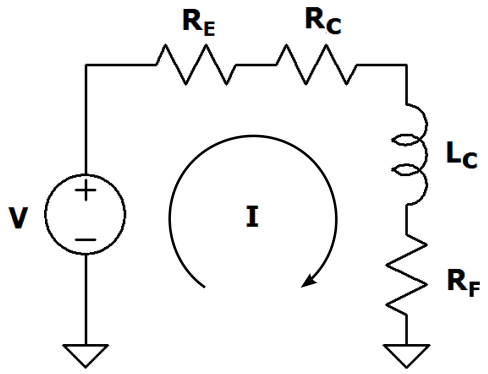


Figure 73: Lumped parameter Helmholtz coil with feedback resistor, $R_F$, and push-pull amplifier emitter resistor, $R_E$.

$$I(s) = \frac{V(s)}{R_E + R_F + R_C + sL_C} = \frac{V(s)}{R' + sL_C}, \tag{8.89}$$

where $R'$ is all the resistors added together to simplify the analysis. Thus, the voltage to current transfer function of the push-pull amplifier, with a voltage gain of $A_V$, and the Helmholtz coil is given by,

$$\begin{aligned} G(s) &= A_V \frac{I(s)}{V(s)} && (8.90)\\ &= A_V \frac{1}{R' + sL_C} && (8.91)\\ &= \frac{A_v}{L_C}\left(\frac{1}{s + \frac{R'}{L_C}}\right) && (8.92)\\ &= k_1 \frac{1}{s+p}, && (8.93) \end{aligned}$$

where $k_1 = \frac{A_v}{L_C}$ and $p = \frac{R'}{L_C}$. The system uses a Proportional-Integral control system that is described by a transfer function in the Laplace domain as,

$$\begin{aligned} D(s) &= k_p + \frac{k_i}{s} && (8.94)\\ &= \frac{sk_p + k_i}{s} && (8.95)\\ &= k_p\left(\frac{s + \frac{k_i}{k_p}}{s}\right) && (8.96)\\ &= k_p \frac{s+z}{s}, && (8.97) \end{aligned}$$

where $z = \frac{k_i}{k_p}$. Using the transfer functions described by equations 8.93 and 8.97, and the block diagram algebra on Figure 72, the closed loop system response can be derived. From the closed loop response, the component values for the control system can be calculated for optimal performance of the system. The most important closed loop response is the effect that the reference signal has on the magnetic field generated by the Helmholtz coils described by,

$$H_1(s) = \frac{B}{R} = Nk_g \frac{D(s)G(s)}{1 + D(s)G(s)R_F A_F} = Nk_g k_1 k_p \left( \frac{s+z}{s^2 + (p+\alpha)s + \alpha z} \right), \tag{8.98}$$

with $\alpha = k_1 k_p R_F A_F$. The other two transfer function of interest are the contributions of the modelled noise sources to the produced magnetic field. Their contributions are described by the following transfer function,

$$H_2(s) = \frac{B}{W_1} = \frac{G(s)}{1 + D(s)G(s)R_F A_F} = Nk_g k_p \left( \frac{s}{s^2 + (p+\alpha)s + \alpha z} \right), \tag{8.99}$$

and

$$H_3(s) = \frac{B}{W_2} = \frac{-A_F D(s)G(s)}{1 + D(s)G(s)R_F A_F} = Nk_g A_F k_1 k_p \left( \frac{-(s+z)}{s^2 + (p+\alpha)s + \alpha z} \right). \tag{8.100}$$

It should be noted that all three of these transfer functions have the same poles, and hence the same bandwidth. The bandwidth of $H_1(s)$ determines how quickly the system can respond to disturbances. The larger the bandwidth, the faster the response will be. However, as shown by $H_2(s)$ and $H_3(s)$, the larger bandwidth will also allow more noise to enter the system. Furthermore, the greater the feedback gain, $A_F$, the larger the noise contribution will be from the $W_2$ noise source. Thus the feedback gain should be kept as small as possible to limit the noise contribution.

By considering the steady state step response of the transfer function:

$$\lim_{s \to 0} s \frac{H_1(s)}{s} = \frac{Nk_g}{R_F A_F}, \tag{8.101}$$

a further effect of reducing the feedback gain can be seen. Equation 8.101 shows that the magnetic field produced for a given reference signal is heavily dependant on the combination of the feedback gain and resistor choice. A smaller feedback gain, $A_F$, would increase the field generated for a particular reference signal. For this project it was decided to limit the number of op-amps in the system as each one contributes a small error signal, additional noise, and greater circuit complexity. If the feedback amplifier is removed and the voltage signal is fed back directly to the control system, then the voltage gain $A_F = 1$.

With the feedback resistor also chosen to be 1 Ω, the output current is equal to the reference voltage. For this thesis, it was decided to use a 16-bit Digital-to-Analogue Converter (DAC) from Texas Instruments, DAC8581, to produce the reference signal. This chip is capable of producing an output between ±5 V, while the maximum current is only 2 A. Thus, a voltage divider should be used at the output of the DAC to ensure that the reference signal never exceeds ±2 V, while still ensuring that the full 16-bit resolution is being used.

To implement the controller, the circuit shown in Figure 74 was used. This circuit has proven to be simple to implement as well as reliable, and hence it was chosen as the controller for this circuit.

To obtain the transfer function D(s), assume no feedback and hence $V_f = 0$V. Under these conditions:

$$V_n = V_{out} \left( \frac{R}{R + \frac{1}{sC}} \right) \tag{8.102}$$

$$\therefore V_n = V_{out} \left( \frac{RCs}{RCs + 1} \right) \tag{8.103}$$

$$\therefore \frac{V_{out}}{V_n} = \left( \frac{RCs + 1}{RCs} \right), \tag{8.104}$$

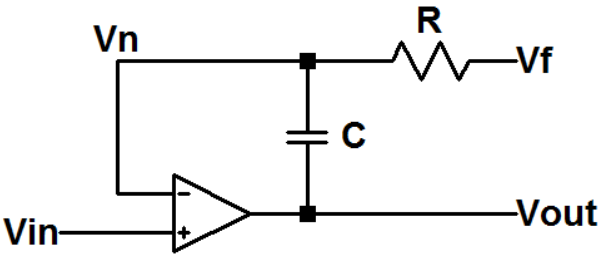


Figure 74: Implemented Proportional-Control system using a single operational amplifier, resistor and capacitor.

However, due to the action of the operational amplifier $V_n = V_{in}$, thus,

$$\frac{V_{out}}{V_{in}} = D(s) = \left(\frac{s + \frac{1}{RC}}{s}\right), \tag{8.105}$$

which has the same form as our desired controller, but with a proportional gain of 1 and $z = \frac{1}{RC}$. By selecting the values for the resistor and capacitor, the poles of the closed loop response can be chosen, and hence the bandwidth of the system. As mentioned earlier, it is desirable to make the bandwidth of the system as large as possible, however the system does have a limit as the Helmholtz coils act as a low pass filter. If the bandwidth is made much greater than the natural cut-off frequency of the coils, it will result in oscillating transients in the current and hence in the magnetic field.

From (8.98), the poles of the closed loop system are given by,

$$s^2 + (p + \alpha)s + \alpha z = 0, \tag{8.106}$$

known as the characteristic equation of the system. By choosing different values for the controller zero $z$, the transient response of the system can be changed. Figure 75 shows the root locus as well as the transient response for different controller zero values.

If the zero value is chosen too low, then the system response is slow, while if it is chosen too high, it introduces transients into the response curve. The SQUID is incredibly sensitive to magnetic fields, thus to ensure that the signal is as smooth as possible while still being fast, it was decided to place the poles at position 2 shown in Figure 75. At this position, the two poles are in the same location and hence the roots of the characteristic equation are equal. The roots for (8.106) are found using the quadratic formula,

$$s_{1,2} = \frac{-(p + \alpha) \pm \sqrt{\Delta}}{2}, \text{ with } \Delta = (p + \alpha)^2 - 4\alpha z. \tag{8.107}$$

When the two roots are equal, $\Delta = 0$. Thus the value for the controller zero can be found as,

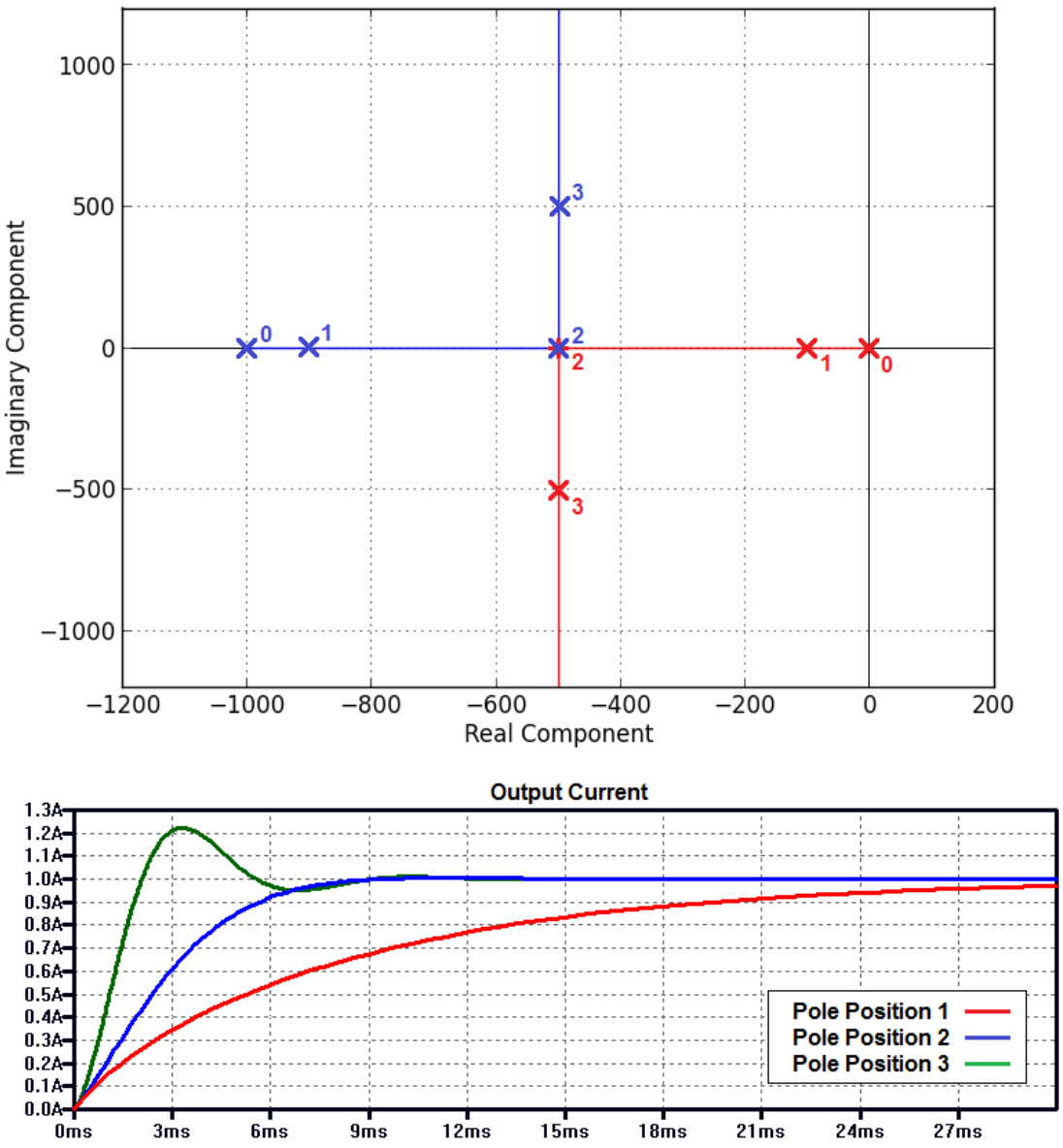


Figure 75: The top graph shows root locus for the closed loop response between the reference signal and the output current for different values for the controller zero. Position 0 is the starting location for the two closed loop poles, while positions 1,2, and 3 are for z values of 500, 1470, and 5800 respectively. The bottom graph shows the transient step response for the different pole locations.

$$(p+\alpha)^2 - 4\alpha z = 0 \tag{8.108}$$

$$z = \frac{(p+\alpha)^2}{4\alpha} \tag{8.109}$$

$$z = \frac{(p+k_1k_pR_FA_F)^2}{4k_1k_pR_FA_F} \tag{8.110}$$

$$z = \frac{(\frac{R'+1}{L_C})^2}{\frac{4}{L_C}} \tag{8.111}$$

$$z = \frac{(R'+1)^2}{4L_C}. \tag{8.112}$$

Using (8.112), it was found that the optimal zero value is 1500, for the current implementation. Finally, the resistor and capacitor values for the controller can be calculated, since $z = \frac{1}{RC}$, by fixing the capacitor value and calculating the resistor value. If the capacitor value is chosen as 100 nF then the resistor value is found to be 6.7 kΩ. A complete circuit diagram can be found in Appendix C.

## 8.6 Correcting Coil Misalignment

When constructing a multi-axis Helmholtz coil, it is very likely that small misalignment errors between the coils will occur. These misalignments will result in the coils producing fields not along their axes and make it difficult to produce precision fields. Fortunately, it is possible to correct for these misalignments using software. Using a matrix it is possible to describe the correlation between the various axes as,

$$B' = AB, \tag{8.113}$$

$$\begin{bmatrix} B'_x \\ B'_y \\ B'_z \end{bmatrix} = \begin{bmatrix} \alpha_{x'x} & \alpha_{x'y} & \alpha_{x'z} \\ \alpha_{y'x} & \alpha_{y'y} & \alpha_{y'z} \\ \alpha_{z'x} & \alpha_{z'y} & \alpha_{z'z} \end{bmatrix} \begin{bmatrix} B_x \\ B_y \\ B_z \end{bmatrix}$$

where A is the correlation matrix with $\alpha_{x'y}$ describing the effect on the generated x-field by the y-field command, $B$ is the desired field, and $B'$ is the actual generated field. It is possible to estimate the correlation matrix by placing a 3-axis reference magnetometer at the centre of the coil system and energising one coil at a time. The reference magnetometer defines the X, Y, and Z axes of the coils and hence care should be taken to ensure that it is aligned as best as possible to the coil axes. By only energising the X-coil, recording the change in the magnetic field and dividing the change in the field by the requested field the first column can be determined. Similarly, the second and third column can be determined. Typically the correlation matrix has the following values:

$$A = \begin{bmatrix} 0.998 & 0.030 & 0.009 \\ -0.018 & 0.996 & -0.072 \\ 0.036 & 0.059 & 0.995 \end{bmatrix}$$

Thus by finding the inverse of the correlation matrix, A, and multiplying it by the requested field, a modified requested field can be found. If this modified field request is sent to the coil control system instead, then the system is able to compensate for the misalignments as described by:

$$B' = AB_{mod} = A(A^{-1}B) = B. \tag{8.114}$$

The effectiveness of this technique was verified experimentally as shown in Figure 76 and table 11.

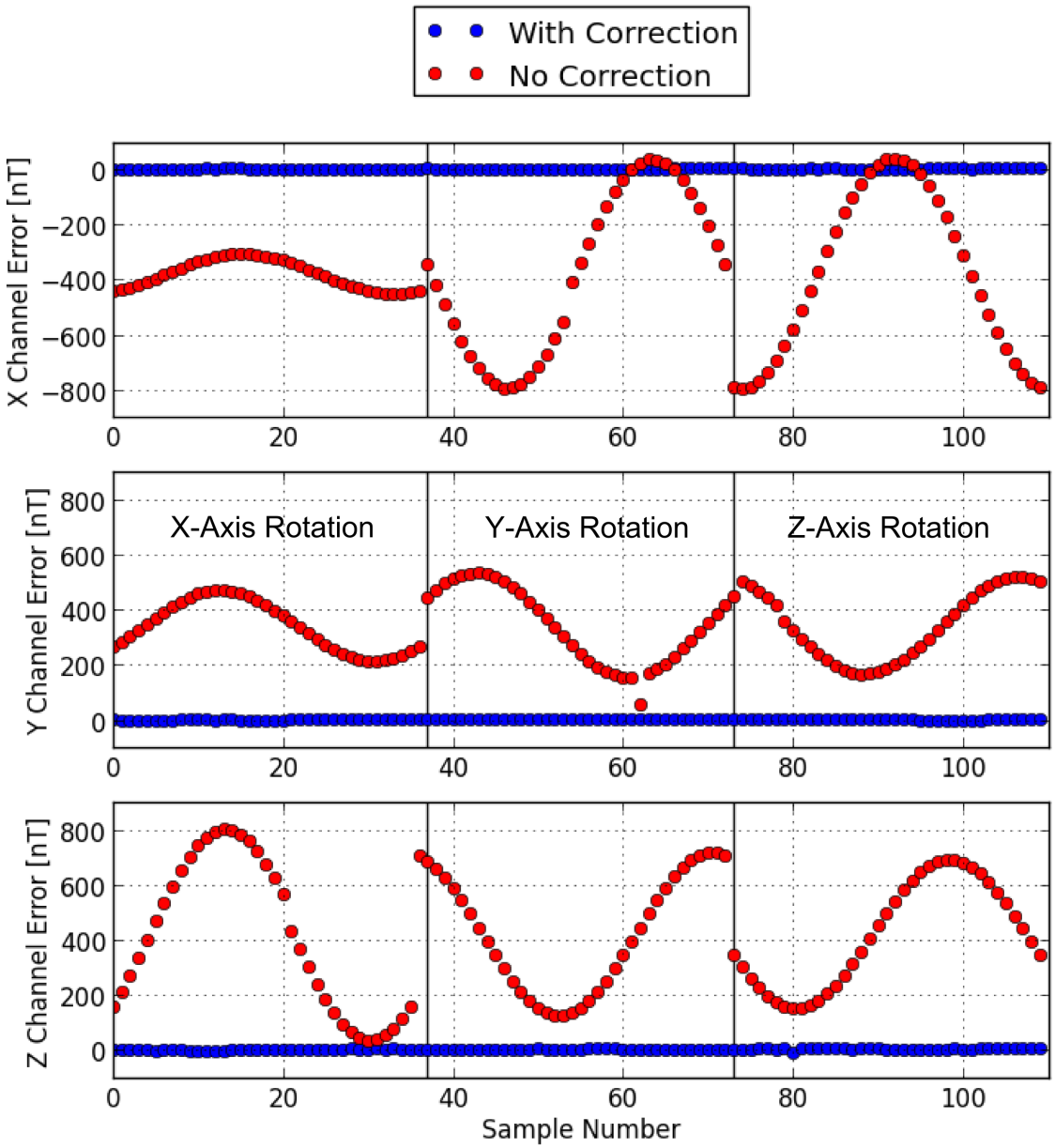


Figure 76: Dramatic reduction of the coil misalignment errors achieved by applying the correction matrix to the field values before they are transmitted to the control system. A fluxgate magnetometer was placed at the centre of the three-axis Helmholtz coil and a 10 $\mu T$ test field was applied at 10 degree steps around each axis. The graph shows the difference between the requested and generated fields, with and without correction, for each 10 degree step. The regions bound by vertical lines indicate where the field is rotated around the X, Y and Z axes respectively.

| **Axis** | **No Correction [nT RMS]** | **With Correction [nT RMS]** |
|---|---|---|
| X | 382.4 | 3.0 |
| Y | 340.6 | 2.0 |
| Z | 416.3 | 3.8 |
| Average | 379.8 | 2.9 |

Table 11: The average error magnitude along each axis with and without the correction matrix for the experimental setup of Figure 76.

# 9 Conclusion

In this thesis the outline for a remote SQUID station for geomagnetic measurements is provided. The SQUID magnetometer is orders of magnitude more sensitive than other magnetometers and hence has the potential to be the next generation instrument for ground based observatories. The maximum potential of this instrument can only be obtained by moving it far from man-made magnetic signals. Moving the instrument to a remote site, does however introduce several infrastructure problems which were discussed in the text.

Some of these problems involved selecting a site based on geographic data. The site needs to be easily accessible for construction and maintenance purposes, but also needs to be clear of local magnetic anomalies. This thesis did not include a detailed study on potential sites, but this would be an essential step before a remote SQUID station can become a reality. Thus, it is recommended that a future project be based on finding these potential sites for the SQUID observatory.

Once a potential site is found it needs to be checked for magnetic anomalies. This is done by surveying the area with magnetometers. The survey instruments are typically PPM that are used to measure the absolute magnetic field as well as the vertical gradient. Any static anomalies, such as buried magnetic material or rock formations, should be detectable with this method, and we have given detailed instructions on how such a survey should be performed. Once an area with a uniform magnetic field is found, the magnetic spectrum of the site must be checked. This is done by placing a fluxgate magnetometer at the proposed site and recording data for as long as possible. The data can then be used to plot a spectrogram of the site to check for periodic signals undetectable by the PPM. Thus, the fluxgate should at least have the same bandwidth as the SQUID. In the case of SANSA and LSBB, this would be 125 Hz. This sampling frequency was chosen since it is fast enough to capute the highest frequency Schumann resonance, while still keeping the number of samples that need to be stored to a manageable size. This would form part of any future survey to find a suitable site for the remote SQUID station.

Once the site has been checked, construction can begin. The station would consist of three buildings placed approximately 40 m apart. These include: the control room, which houses all computers and supporting electronics, the power hut, which contains a regulated battery bank charged from a solar array that delivers DC power to the rest of the system, and the SQUID hut itself, which is thermally insulated by cavity walls. The SQUID is placed on an isolation pillar that decouples it from structural vibrations due to wind and outside temperature fluctuations. The temperature inside the SQUID hut is also monitored, as changes in temperature can result in small deformations of the SQUID mounting system which lead to changes in the SQUID's orientation. The changes in the orientation will appear as slow varying magnetic signals on the SQUID output. In principle, it is possible to compensate for these variations through post-processing. Many construction materials are magnetic in nature, such as steel and certain types of bricks, and hence any material should be checked with a magnetometer before being included in the construction of the station. Also of interest is the effect of a standby diesel generator on site, should the photovoltaic power system fail. However, there was not enough time to include such a study in this work.

The benefits of the SQUID do come with a few drawbacks, however, the greatest of these being the need for cryogenic cooling. The HTS SQUID was the focus of this study and hence immersion cooling using liquid

nitrogen was found to be the optimal cooling method. This method is simple and does not introduce additional mechanical or electrical noise to the system like cryocoolers would. Immersion cooling does however require periodic refilling of the dewar as the liquid nitrogen slowly evaporates. Typically, this needs to be done every few weeks depending on the capacity of the dewar. The refilling procedure needs to be performed in a simple and safe manner without significantly disrupting the functionality of the SQUID. To achieve this, a pumping scheme was developed that used very simple and inexpensive components. Once end of a Teflon or copper tube would be placed at the bottom of the refill dewar, while the other was placed at the top of the SQUID dewar. A small heater was also placed inside the refill dewar and the container sealed. As the heater was switched on, a small quantity of the liquid nitrogen would boil off and pressurise the refill dewar. This would force liquid nitrogen through the tube and into the SQUID dewar. Using this technique a pumping rate of 1.8 litres per minute with a 60 W heater was achievable. To ensure that the pressure remained at safe levels inside the dewar, a burst disk pressure relief system was installed on all dewars. If the pressure inside the dewar exceeded a predetermined value, the disk would rupture and the pressurising gas would vent safely.

An important requirement is the monitoring of the liquid nitrogen level inside the SQUID dewar. If the level dropped too low, the SQUID would stop functioning. However, unnecessary trips to the remote station also needs to be avoided given the potential difficulty and expense of accessing these stations. Thus, knowing the liquid nitrogen level and when exactly to dispatch a refill team is required optimal management of the station. The monitoring is performed by placing the SQUID dewar on a specially designed non-magnetic loadcell scale. The scale was designed to minimise tilting as the weight of the dewar changed. If the orientation of the scale changed, it would appear as a slowly varying voltage signal on the output of the SQUID. Future projects could involve integrating this data into the SQUID data, or setting up an automated warning system should the liquid nitrogen levels become low. If the site is extremely remote, the potential of introducing a small scale liquid nitrogen generator also exists. However, these systems would need to run for a few days per month and the compressor that is used in these systems could produce unwanted magnetic signals at the site. Due to cost constraints, the impact of these systems on the SQUID station could not be investigated.

When a HTS SQUID is cooled in a large magnetic field, such as the Earth's field, Abrikosov vortices are likely to form in the superconducting material. As these vortices jump between pinning sites in the material, they increase the 1/f noise of the device and have been found to reduce the stability of the SQUID. In this thesis, a shielding method using a 3-axis Helmholtz coil system was investigated. These coils are relatively simple and inexpensive to construct and do not attenuate the signals of interest, unlike metal shielding. It was found that by cooling the SQUID in the reduced magnetic field, generated by the Helmholtz coils, the stability of the SQUID can be improved significantly. When the SANSA SQUID was cooled in the ambient field, some of the channels drifted to -10 V within a few seconds. Using a 3-axis Helmholtz coil, the ambient field was reduced from 25000 nT to 800 nT and the SQUID was cooled in this reduced field. All channels were stable over the observed period of approximately 10 minutes. The coils were then shut down smoothly over a period of 20 minutes. The channels were still stable but tended drift by a small amount over the 10 minute observation period. This is not likely to be due to natural variation since no drifting was observed minutes before when the coils were left on. Metal shields can be used to reduce the magnetic field, but are awkward to use and also reduce the magnitude of the signals of interest. This thesis provided details on how the Helmholtz coils can be

constructed as well as their effectiveness at stabilising the the SQUID. Future studies can include what effect these coils have on the noise profile of the SQUID and to find the optimal shut down procedure for the coils.

By and large this thesis provided the groundwork for several potential projects to come. It is my belief that a remote SQUID station for geomagnetic research is achievable, and while many obstacles do still remain, none of them are insurmountable. It is hoped that this document, as well as those to follow will pave the way for future SQUID observatories that would be used to study the Earth magnetic signals in greater detail than ever before.

# References


[1] S. Gaffet, et al. Simultaneous seismic and magnetic measurements in the low-noise underground laboratory (lsbb) of rustrel, france, during the 2001 january 26 indian earthquake. *Geophysics Journal International*, 155:981–990, 2003.

[2] J. Kawai. Realizin a squid magnetometer for practical geomagnetic field measurements. *International Superconductivity Technology Center*, 2013.

[3] NC State University. `http://www.nc-climate.ncsu.edu/edu/k12/.AtmStructure`. accessed: 26 October 2014.

[4] M. G. Kivelson and C. T. Russell. *Introduction to space physics*. Cambridge university press, 1995.

[5] Intermagnet data. `http://www.intermagnet.org/`. accessed: 24 November 2014.

[6] G. S. Lakhina, et al. On magnetic storms and substorms. In *Proceedings of the ILWS Workshop*, volume 1, page 320, 2006.

[7] Wikipedia: Geomagnetic storms. `http://en.wikipedia.org/wiki/Geomagnetic_storm`. accessed: 11 November 2014.

[8] Atmospheric and environmental research: Space weather. `http://www.aer.com/science-research/space/space-weather/space-weather-index`. accessed: 25 November 2014.

[9] R. L. McPherron. Magnetic pulsations: their sources and relation to solar wind and geomagnetic activity. *Surveys in Geophysics*, 26(5):545–592, 2005.

[10] P. Kotze. personal communication.

[11] C. Price, et al. Schumann resonances in lightning research. *J. of Lightning Res*, 1:1–15, 2007.

[12] S. K. Park, et al. Electromagnetic precursors to earthquakes in the ULF band: A review of observations and mechanisms. *Reviews of Geophysics*, 31(2):117–132, 1993.

[13] G. Waysand, et al. Earth-ionosphere couplings, magnetic storms, seismic precursors and TLEs: Results and prospects of the [SQUID]2 system in the low-noise underground laboratory of Rustrel-Pays d'Apt, journal=Comptes Rendus Physique. 12:192–202, 2011.

[14] T.P. Orlando and K.A. Delin. *Foundations of Applied Superconductivity*. Addison-Wesley Publishing Company, 1991.

[15] S. A. Kane and J. Gollub. *Superconductivity and SQUID Laboratory Manual*, 2005.

[16] D. Halliday, et al. *Fundamentals of physics extended*. John Wiley & Sons, 2010.

[17] A. M. Kadin. *Introduction to superconducting circuits*. Wiley New York, 1999.

[18] W. G. Jenks, et al. Squids for nondestructive evaluation. *Journal of Physics D: Applied Physics*, 30(3):293, 1997.

[19] Closely-spaced search-coil magnetometer array on svalbard. http://mirl.sr.unh.edu/ULF/ULF_svalbard.html. accessed: 29 October 2014.

[20] C. M. Schlinger. Mangetometer and gradiometer surveys for detection of underground storage tanks. *Bulletin of the Association of Engineering Geologists*, XXVII:37–50, 1990.

[21] Gem systems advanced magnetometers. http://www.gemsys.ca/. accessed: 25 November 2014.

[22] I. Hrvoic, et al. Brief review of quantum magnetometers. *GEM Systems Technical Papers*, 2005.

[23] V. Tiporlini and K. Alameh. High sensitivity optically pumped quantum magnetometer. *The Scientific World Journal*, 2013, 2013.

[24] K. Evans. Fluxgate magnetometer explained, 2006.

[25] M. Butta, et al. Reduction of noise in fundamental mode orthogonal fluxgates by optimization of excitation current. *Magnetics, IEEE Transactions on*, 47(10):3748–3751, 2011.

[26] Bartington. http://www.bartington.com. accessed: 30 October 2014.

[27] J. Jankowski and C. Sucksdorff. Guide for magnetic measurements and observaiory practice. 1996.

[28] B. J. St-Louis. Intermagnet technical reference manual, version 4.6, intermagnet, 2012.

[29] A. Trnkoczy, et al. Site selection, preparation and installation of seismic stations. *Bormann, P.(ur.)*, 2002.

[30] Federal Communications Commission. Understanding the fcc regulations for low-power, non-licensed transmitters. *Office of Engineering and Technology*, 34, 1993.

[31] Which is the best satellite internet service provider for rural areas? http://www.globalcomsatphone.com/hughesnet/internet.html. accessed: 19 November 2014.

[32] Mweb satellite internet. http://www.mweb.co.za/business-internet/connectivity/vsat-satellite-internet-access.aspx. accessed: 19 November 2014.

[33] Vsat uncapped. https://www.iburst.co.za/?option=com_content&view=article&id=16&Itemid=490. accessed: 19 November 2014.

[34] Hermanus seekers. http://www.hermanus-seekers.com/hermanus/weather-for-hermanus. accessed: 9 November 2014.

[35] Elan2. www.elan2.com. accessed: 29 November 2014.

[36] Cryomech. http://www.cryomech.com/. accessed: 29 November 2014.

[37] Remote power inc. http://www.remotepowerinc.com/resources.php. accessed: 15 November 2014.

[38] Solon black 280/11, blue 270/11. http://www.solon.com/global/products/power-plants_old/modules/index.html. accessed: 16 November 2014.

[39] Sharp nd-rxxxa5 solar panel. www.sharp.eu/solar. accessed: 16 November 2014.

[40] D. Medveď, et al. Importance of batteries for photovoltaic systems. *Inteligentné riadenie vỳroby a spotreby elektriny z obnovitel'nỳch energetickỳch zdrojov 2011*, page 40, 2011.

[41] Z. M. Omer, et al. Comparison of discharge performance of 12v/150ah gel and agm sealed lead-acid batteries in stand-alone pv-based systems in uae.

[42] J. W. Stevens and G. P. Corey. A study of lead-acid battery efficiency near top-of-charge and the impact on pv system design. In *Photovoltaic Specialists Conference, 1996., Conference Record of the Twenty Fifth IEEE*, pages 1485–1488. IEEE, 1996.

[43] R. Ramabadran and B. Mathur. Effect of shading on series and parallel connected solar pv modules. *Modern Applied Science*, 3(10):P32, 2009.

[44] C. Christensen and G. Barker. Effects of tilt and azimuth on annual incident solar radiation for united states locations. *Solar Engineering*, pages 225–232, 2001.

[45] Solar GIS. `http://solargis.info/`. accessed: 16 November 2014.

[46] Meteonorm. `http://meteonorm.com/`. accessed: 29 November 2014.

[47] H. Worters. The SAAO 1m Telescope: A User's Guide. `http://www.saao.ac.za/wp-content/uploads/sites/5/40v1.4.pdf`. accessed: 17 November 2014.

[48] F. Coleman. Cryogenic safety. *NASA - 2013 WFF Safety Awareness Campaign*, 2013.

[49] R. Teodorescu. *General Safety Considerations for the Installation and Operation of Superconducting Magnet Systems*. Bruker Biospin, 2002.

[50] *Safety Bulletin: Oxygen-Deficient Atmospheres*, 3rd edition, 1992.

[51] *Material Safety Data Sheet: Liquid Nitrogen*, version 2 edition, 2009.

[52] A. L. Woodcraft. *An introduction to cryogenics*, 2007.

[53] A.E. Shapiro. Brazing: Q&A. *Welding Journal*, pages 20–21, 2013.

[54] B. S. Guru and H. R. Hiziroglu. *Electromagnetic field theory fundamentals*. Cambridge University Press, 2004.

[55] T. T. Li. Tri-axial square helmholtz coil for neutron edm experiment. *University of Hong Kong*, 2004.

[56] Finite element method magnetics. www.femm.info.

[57] J. Clarke and A.I. Braginski. *The SQUID Handbook: Vol.1 Fundamentals and Technology of SQUIDs and SQUID Systems*. Whiley-VCH, 2004.

[58] H. Dantsker, et al. Reduction of 1/f noise in high-tc dc superconducting quantum interference devices cooled in an ambient magnetic field. *Applied Physics Letters, Vol. 69, No. 26*, pages 4099–4101, 1996.

[59] E. Saunderson. personal communication.

[60] F. W. Grover. *Inductance calculations: working formulas and tables*. Courier Dover Publications, 2004.

# Appendix A: Python code for amplifier design

```
from __future__ import division
import matplotlib.pyplot as plt
import numpy as np

# This script attempts to choose the the optimal components based on wire cost considerations
    and maximum power consideration.
# It is assumed that the coil is square and being driven by a push-pull amplifier with a
    feedback resistor for current control.

run_cost_power = 0
run_other = 1

C_WG = 0
C_DIA = 1
C_AREA = 2
C_OPKM = 3
C_MPL = 4
C_CPM = 5
WG_table = np.loadtxt("SWG_table.csv", skiprows=2)

C_I = 0
C_RL = 1
C_RE = 2
C_RB = 3
C_POW = 4
C_COST = 5
C_NUM = 6
C_POWTOT = 7
C_P_RB = 8
C_P_RE = 9
C_P_Q12= 10
C_P_Q34 = 11

# Amplifier characterisitcs
Vcc = 12
Rb = 0
Re = 0
Rl = 0
Rf = 1
Beta = 70
Vbe = 0.8
Imax = 0
dVbe = 0.0165

# Coil Characterisitics
B_max = 60e-6*1.25
l = 1
```

```
NI = B_max/(1628.8e-9/l)

N = 1
u0 = 4*np.pi*10**(-7)
r = 0.0005

print N**2 * (2*l*u0)/np.pi * (np.log(l/r) - 0.77401)*1000*2


label_size = 16

N = 100
my_legend = []

r_range = [0.1, 0.11, 0.12, 0.13, 0.15, 0.16, 0.18, 0.2, 0.22, 0.24, 0.27, 0.30, 0.33, 0.36,
    0.39, 0.43, 0.47, 0.51, 0.56, 0.62, 0.68, 0.75, 0.82, 0.91, 1]

power_upper = {}
power_lower = {}
current_graph = {}

if run_cost_power:
    for Rf in [0.1,0.68]:
        fig = plt.figure(0)
        cost_ax = fig.add_subplot(121)
        pow_ax = fig.add_subplot(122)
        for wire in WG_table:
            graphs = np.zeros((1,12))

            for Imax in np.linspace(0.5, 5, N, True):
                if Imax <= wire[C_AREA]*2.6:
                    # Calculate the number of windings required for given current
                    N = np.ceil(NI/Imax)
                    #N = NI/Imax
                    cost = (8*l)*N*(wire[C_MPL]*1000)*wire[C_CPM]

                    # For the chosen wire, calculate the resistance
                    Rl = wire[C_OPKM]*(8*l)*N/1000

                    P_best = 1e6
                    Re_best= 0
                    Rb_best = 0

                    P_RB_best = 0
                    P_RE_best = 0
                    P_Q34_best = 0
                    P_Q12_best = 0
                    best_found = False
                    for Re in np.linspace(0.1,2,100,True):
```

```
                Av = (Rl+Rf)/(Rl+Rf+Re)
                Vit = 2*dVbe/(1-Av)

                a = (1-Av)/2
                V1max = Re/(2*a)*(Vcc*a/Re - dVbe/Re)

                Rb = (Beta+1)*((Vcc-Vbe)/Imax - Re - Rl - Rf)
                P_RB = 4*Vcc**2/Rb
                P_RE = Imax**2*Re

                if V1max < Vit:
                    Ic = (V1max*a + dVbe)/Re
                    Vce = Vcc - V1max
                    P_Q34 = Ic*Vce
                else:
                    P_Q34 = Vcc**2/(4*(Rl+Rf+Re))

                P_Q12 = Vcc**2/Rb

                P = np.max([P_RB, P_RE, P_Q12, P_Q34])

                if Rb > 0 and P < P_best:
                    Re_best = Re
                    Rb_best = Rb
                    P_RB_best = P_RB
                    P_RE_best = P_RE
                    P_Q34_best = P_Q34
                    P_Q12_best = P_Q12
                    P_best = P
                    P_max = np.sum([P_RB, P_RE, P_Q12, P_Q34])
                    best_found = True

            if best_found:
                graphs = np.vstack((graphs,[Imax, Rl, Re_best, Rb_best, P_best, cost,
                    N, P_max,P_RB_best,P_RE_best,P_Q12_best,P_Q34_best]))

                if my_legend.count('SWG' + str(int(wire[C_WG]))) == 0:
                    my_legend.append('SWG' + str(int(wire[C_WG])))

    c = 'k'

    if wire[C_WG] == 18:
        c = 'r'
    elif wire[C_WG] == 19:
        c = 'g'
    elif wire[C_WG] == 20:
        c = 'b'
```

```
            if current_graph.has_key('SWG' + str(int(wire[C_WG]))) == False:
                cost_ax.plot(graphs[2:,C_I],graphs[2:,C_COST],linewidth=2,color=c)
                cost_ax.grid(b=True, which='major', color='k', linestyle='-')
                cost_ax.grid(b=True, which='minor', color='0.4', linestyle='--')
                cost_ax.set_ylabel('Wire Cost [ZAR]',size=label_size)
                cost_ax.set_xlabel('Maximum Current [A]',size=label_size)
                cost_ax.legend(my_legend,loc=0,fontsize=label_size)
                cost_ax.set_xlim([0.5,3])

            current_graph['SWG' + str(int(wire[C_WG]))] = graphs[2:,C_I]

            if Rf < 0.3:
                power_lower['SWG' + str(int(wire[C_WG]))] = graphs[2:,C_POW]
            else:
                power_upper['SWG' + str(int(wire[C_WG]))] = graphs[2:,C_POW]

    for w in my_legend:
        x = current_graph[w]
        y1 = power_lower[w]
        y2 = power_upper[w]

        c = 'k'

        if w == 'SWG18':
            c = 'r'
        elif w == 'SWG19':
            c = 'g'
        elif w == 'SWG20':
            c = 'b'

        y1 = y1[0:len(y2)]

        pow_ax.fill_between(x,y1,y2,color=c,alpha=0.5)
        pow_ax.plot(x,y1,color=c,linewidth=2)
        pow_ax.plot(x,y2,color=c,linewidth=2)
        pow_ax.grid(b=True, which='major', color='k', linestyle='-')
        pow_ax.grid(b=True, which='minor', color='0.4', linestyle='--')
        pow_ax.set_ylabel('Max Power Dissipation [W]',size=label_size)
        pow_ax.set_xlabel('Maximum Current [A]',size=label_size)
        pow_ax.set_ylim([0,20])
        pow_ax.set_xlim([0.5,3])

    '''
    pow_ax.semilogy(graphs[2:,C_I],graphs[2:,C_POW],linewidth=2,color=c)

    '''
```

```
    for tick in pow_ax.xaxis.get_major_ticks():
        tick.label.set_fontsize(label_size)
    for tick in pow_ax.yaxis.get_major_ticks():
        tick.label.set_fontsize(label_size)

    for tick in cost_ax.xaxis.get_major_ticks():
        tick.label.set_fontsize(label_size)
    for tick in cost_ax.yaxis.get_major_ticks():
        tick.label.set_fontsize(label_size)

    fig.tight_layout()

    fig.set_figheight(13)
    fig.set_figwidth(11)

    plt.show()
        #plt.savefig('component_graphs.png',dpi=600)


# Enter design values here
#-------------------------
Imax = 2.5
SWG = 18
Rf = 0.47
#-------------------------

cost = 0
Rl = 0

if run_other:
    N = np.ceil(NI/Imax)
    for w in WG_table:
        if w[C_WG] == SWG:
            Rl = w[C_OPKM]*(8*l)*N/1000

            cost = (8*l)*N*(w[C_MPL]*1000)*w[C_CPM]
            r = w[C_DIA]/2/1000
            wire = w
            break

    u0 = 4*np.pi*10**(-7)

    L = N**2 * (2*l*u0)/np.pi * (np.log(l/r) - 0.77401)*1000*2


    if Imax <= wire[C_AREA]*2.6:
        P_best = 1e6
        Re_best= 0
        Rb_best = 0
```

```
    P_RB_best = 0
    P_RE_best = 0
    P_Q34_best = 0
    P_Q12_best = 0
    Av_best = 0
    Ai_best = 0
    for Re in r_range:
        Av = (Rl+Rf)/(Rl+Rf+Re)
        Vit = 2*dVbe/(1-Av)

        a = (1-Av)/2
        V1max = Re/(2*a)*(Vcc*a/Re - dVbe/Re)

        Rb = (Beta+1)*((Vcc-Vbe)/Imax - Re - Rl - Rf)

        P_RB = 4*Vcc**2/Rb
        P_RE = Imax**2*Re

        if V1max < Vit:
            Ic = (V1max*a + dVbe)/Re
            Vce = Vcc - V1max
            P_Q34 = Ic*Vce
        else:
            P_Q34 = Vcc**2/(4*(Rl+Rf+Re))

        P_Q12 = Vcc**2/Rb

        P = np.max([P_RB, P_RE, P_Q12, P_Q34])
        Io_max = (Vcc-Vbe)/(Re+Rl+Rf+Rb_best/(Beta+1))

        if Rb > 0 and P < P_best:
            wL = (8*l)*N
            Re_best = Re
            Rb_best = Rb
            P_RB_best = P_RB
            P_RE_best = P_RE
            P_Q34_best = P_Q34
            P_Q12_best = P_Q12
            P_best = P
            P_max = np.sum([P_RB, P_RE, P_Q12, P_Q34])
            Av_best = Av
            Ai_best = (1+Beta)*Av*Rb/(2*(Rl+Rf))
else:
    print "Maximum current to high for chosen wire gauge"

Io_max = (Vcc-Vbe)/(Re_best+Rl+Rf+Rb_best/(Beta+1))

print "Av = {0:.2f}".format(Av_best)
```

```
print "Ai = {0:.2f}".format(Ai_best)
print "Imax = {0:.2f} A".format(Io_max)
print "Rb = {0:.1f} Ohm".format(Rb_best)
print "Re = {0:.2f} Ohm".format(Re_best)
print "Rf = {0:.2f} Ohm".format(Rf)
print "N = {0:.0f} Turns".format(N)
print "Rcoil = {0:.2f} Ohm".format(Rl)
print "Lcoil = {0:.1f} mH".format(L)
print "Cost = R{0:.2f}".format(cost)
print "Wire Length = {0:.1f} m".format(wL)
print "Power RB = {0:.1f} Watt".format(P_RB_best)
print "Power RE = {0:.1f} Watt".format(P_RE_best)
print "Power RF = {0:.1f} Watt".format(Rf*Io_max)
print "Power Q3/4 = {0:.1f} Watt".format(P_Q34_best)
print "Power Q1/2 = {0:.1f} Watt".format(P_Q12_best)

# Show the relationship between Rf and maximum power
Rf_graph = []
Re_graph = []
Pow_graph = []

for Rf in r_range:
    P_best = 1e6
    Re_best= 0
    Rb_best = 0

    P_RB_best = 0
    P_RE_best = 0
    P_Q34_best = 0
    P_Q12_best = 0
    for Re in r_range:
        Av = (Rl+Rf)/(Rl+Rf+Re)
        Vit = 2*dVbe/(1-Av)

        a = (1-Av)/2
        V1max = Re/(2*a)*(Vcc*a/Re - dVbe/Re)

        Rb = (Beta+1)*((Vcc-Vbe)/Imax - Re - Rl - Rf)

        P_RB = 4*Vcc**2/Rb
        P_RE = Imax**2*Re

        if V1max < Vit:
            Ic = (V1max*a + dVbe)/Re
            Vce = Vcc - V1max
            P_Q34 = Ic*Vce
        else:
            P_Q34 = Vcc**2/(4*(Rl+Rf+Re))
```

```
            P_Q12 = Vcc**2/Rb

            P = np.max([P_RB, P_RE, P_Q12, P_Q34])
            Io_max = (Vcc-Vbe)/(Re+Rl+Rf+Rb_best/(Beta+1))

            if Rb > 0 and P < P_best:
                Re_best = Re
                Rb_best = Rb
                P_RB_best = P_RB
                P_RE_best = P_RE
                P_Q34_best = P_Q34
                P_Q12_best = P_Q12
                P_best = P
                P_max = np.sum([P_RB, P_RE, P_Q12, P_Q34])

        Rf_graph.append(Rf)
        Pow_graph.append(P_max)
        Re_graph.append(Re_best)

plt.figure()
plt.plot(Rf_graph,Pow_graph,linewidth=2)
plt.xlabel('Feedback Resistor [Ohm]',fontsize=20)
plt.ylabel('Sum Of Max Power [W]',fontsize=20)
plt.xticks(size=16)
plt.yticks(size=16)
plt.grid(which='minor')
plt.grid(which='major',ls='-')

plt.figure()
plt.plot(Rf_graph,Re_graph,linewidth=2)
plt.xlabel('Feedback Resistor [Ohm]',fontsize=20)
plt.ylabel('Emitter Resistor [Ohm]',fontsize=20)
plt.xticks(size=16)
plt.yticks(size=16)
plt.grid(which='minor')
plt.grid(which='major',ls='-')


# RF and RB selection
Re = 0.16
Vcc = 12
Vbe = 0.8
Io_max = 1.4
Rl = 6.6
Beta = 70

pow_graph = []
Rf_graph = []
Rb_graph = []
```

```
for Rf in np.linspace(0.1, 2, 100, True):
    Rb = (Beta + 1)*((Vcc - Vbe)/Io_max - Re - Rl - Rf)

    if Rb > 0:
        pow_graph.append(Vcc**2/Rb)
        Rf_graph.append(Rf)
        Rb_graph.append(Rb)

plt.figure()
plt.plot(Rb_graph,Rf_graph)
plt.show()
```

# Appendix B: SWG Wire Table

The information in this table was gathered from local suppliers and is used with the Python script shown in Appendix A.

| Wire Gauge | Diameter | Area | Ohm per km | Mass per length | Cost per gram |
|---|---|---|---|---|---|
| SWG | mm | $mm^2$ | Ohm/km | kg/m | R/g |
| 18 | 1.220 | 1.1700 | 14.8 | 0.010400 | 0.2628 |
| 19 | 1.020 | 0.8110 | 21.3 | 0.007230 | 0.3255 |
| 20 | 0.914 | 0.6570 | 26.3 | 0.005860 | 0.2336 |
| 21 | 0.813 | 0.5190 | 33.2 | 0.004630 | 0.3565 |
| 22 | 0.711 | 0.3970 | 43.4 | 0.003540 | 0.3633 |
| 23 | 0.610 | 0.2920 | 59.1 | 0.002600 | 0.3743 |
| 25 | 0.508 | 0.2030 | 85.1 | 0.001810 | 0.3743 |
| 27 | 0.417 | 0.1360 | 127.0 | 0.001220 | 0.4548 |
| 30 | 0.315 | 0.0779 | 221.0 | 0.000695 | 0.3400 |
| 33 | 0.254 | 0.0507 | 340.0 | 0.000452 | 0.3743 |
| 36 | 0.193 | 0.0293 | 589.0 | 0.000261 | 0.3400 |

Table 12: SWG table used in program of appendix A.

# Appendix C: Coil control circuit

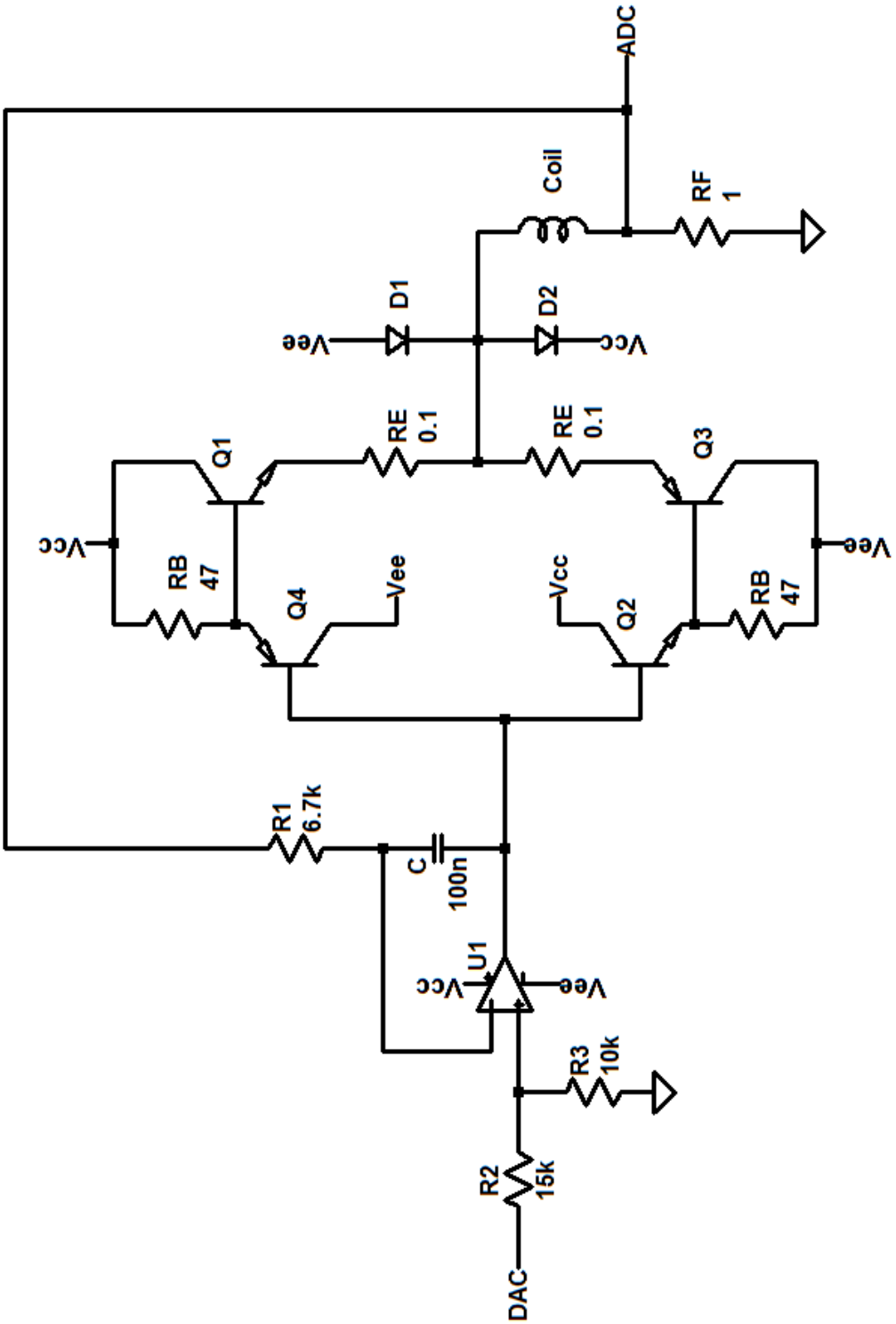


Figure 77: Final amplifier and control circuit for the Helmholtz coils (computer interface not shown).

# Appendix D: Final coil geometries

| | Cancellation Coil | Calibration Coil |
|---|---|---|
| Geometry | Square | Square |
| Side Length [m] | 0.97 | 0.97 |
| Separation [m] | 0.53 | 0.53 |
| Max Field [nT] | 60,000 | 200 |
| Max Current [A] | 2 | 0.15 |
| Number of Windings | 23 | 1 |
| Wire Type | SWG19 | SWG19 |
| Wire Length [m] | 180 | 8 |
| Coil Resistance [Ω] | 3.8 | 0.17 |
| Coil Inductance [mH] | 5.6 | 0.01 |
| Estimate Cost [ZAR] | 420 | 19 |

Table 13: Final coil geometries.